University of Technology Ilmenau

Fully Integrated Transducer Platform with Cavity Optomechanical Readout

Author:

M.Sc. Thomas Michels

Reviewer:

Prof. Dr. rer. nat. habil. Ivo W. Rangelow

Prof. Dr. Sc. Teodor Pawel Gotszalk

Prof. Dr. Reza Moheimani

Date of public defense:

16.06.2019

urn:nbn:de:gbv:ilm1-2019000590

Abstract

Research and development of transducers based on cavity optomechanics is a topic of high interest particularly because these transducers enable measurement of mechanical motion down to the fundamental limit of precision imposed by quantum mechanics. The development of an on-chip cavity optomechanical transducer platform that combines high bandwidth and sensitivity near the standard quantum limit with compactness, robustness, small size, and potential for low cost batch fabrication inherent in MEMS is demonstrated as a proof of concept study.

Design, fabrication and characterization of fully integrated and fiber pigtailed transducers is presented. The devices combine high sensitivity (0.14 – 40 fm·Hz$^{-1/2}$), high bandwidth optomechanical readout and built-in thermal and electrostatic actuation. It is implemented by a double-side wafer-scale microfabrication process combining one e-beam, six stepper, and three contact mask aligner lithography steps.

The SiN probes can be actuated using an electrical signal supplied to an integrated thermal or electrostatic actuator. The probe is evanescently coupled to a high-Q (10^5 – 2 x 10^6) optical whispering gallery mode of the optical microdisk cavity and the motion is detected by measuring the resonance frequency shift of the optical cavity mode. The actuator can be used to dynamically move the probe as well as to tune the distance between the cantilever and the optical cavity, to change the sensitivity and range of measurement of the cantilever. One side of the probe overhangs the edge of the chip, where it can be easily coupled to a variety of off-chip samples and physical systems of interest.

The modular design of the transducer allows for parallelization, which enables the possibility of sensor arrays for simultaneous detection of multiple forces or other physical properties. Parallelization is shown on a 2x1 array, which can be easily extended to larger array architectures. The application of the probe arrays and single probes in a commercial scanning probe microscope is shown.

In addition the flexibility of this transducer approach is demonstrated with membrane transducers and acceleration sensors. The performance of all presented transducers is studied, focusing on displacement sensitivity,

frequency stability and readout gain tuning.

Zusammenfassung

Forschung und Entwicklung von Wandlern basierend auf kavität- optomechanischen Elementen ist ein Forschungsgebiet von hohem Intresse. Sie kombiniert hohe Bandbreiten und Empfindlichkeit nahe dem Standardquantumlimit mit Kompaktheit, Robustheit, kleinen Abmessungen und dem Potential für eine wirtschaftliche Massenproduktion systemimmanent bei mikroelektromechanischen Systemen. Vollintegrierte Wandler erlauben demnach Bewegungsmessungen bis hin zum fundamentalen Quantenlimit.

In dieser Arbeit werden Design, Herstellung und Charakterisierung eines vollintegrierten und glasfasergekoppelten Wandlers in einer Machbarkeitsstudie dargestellt. Das System kombiniert hohe Verschiebungsauflösungen 0.14 – 40 fm·Hz$^{-1/2}$), optomechanische Detektion mit hoher Bandbreite und eine eingebaute thermische und elektrostatische Anregung. Die Herstellung erfolgt in einem doppelseitigen mikro- und nanotechnischen Fertigungsverfahren auf Waferbasis, in einer Kombination aus einem Elektronenstrahllithographieschritt, sechs Projektionslithographieschritten und drei Kontaktlithographie Schritten.

Die Siliziumnitridsonden können mittels eines elektrischen Signals, angelegt an den integrierten thermischen oder elektrostatischen Aktuator, angeregt werden. Sie sind optisch über das evanecente Feld mit einer optischen Kavität hoher Güte (10^5 – 2 x 10^6) gekoppelt. Die Bewegung der Sonde wird detektiert über eine Veränderung der Resonanzfrequenz der Kavität. Die eingebauten Aktuatoren ermöglichen die Einstellung des Abstandes zwischen Sonde und optischer Kavität, welche die Einstellung der Sensitivität ermöglicht. Eine Seite der Sonde steht über die Kante des Siliziumchips, um die Kopplung mit einer Vielzahl von Proben und physikalischen Systemem zu erlauben.

Die modulare Bauweise des Wandlers schafft die Grundlage zur Parallelisierung der Sonden für die gleichzeitige Messung mehrer Kräfte oder pysikalischer Eingenschaften. Die Parallelisierung wird in dieser Arbeit am Beispiel eines 2x1 Array gezeigt, welche mit geringem Aufwand auf größere Arrayarchitekturen angepasst werden kann. Zur Demonstration der Funktion von Einzelsonden und Sondenarrays, wird die Sondenanwendung in der Rasterkraftmikroskopie präsentiert.

Desweiteren wird die Flexibilität der Wandlerbauweise an der Herstel-

lung von Membrane- und Beschleunigungswandlern belegt. Das das Verhalten aller hergestellten Wandler wird hinsichtlich der Bewegungsempfindlichkeit, Frequenzstabilität, und Einstellbarkeit der Auslesung analysiert.

List Publications

Listed below are publications that took place during my time in graduate school.

- Thomas Michels, Ivo W. Rangelow: **Review of scanning probe micromachining and its applications within nanoscience**. – *Microelectronic Engineering (Review article)*, Volume 126, 25 August 2014, Pages 191-203
- Thomas Michels, Vladimir Aksyuk: **Cavity optical transducer platform with integrated actuation for multiple sensing applications.** – *Proceedings, Solid State Sensor, Actuator and Microsystems Workshop*, June 5-9, 2016
- Thomas Michels, Ivo W. Rangelow, Vladimir Aksyuk: **Fabrication Process for an Optomechanical Transducer Platform with Integrated Actuation**. – *J. Res. Natl. Inst. Stand.*, Volume 121 (2016)
- Thomas Michels, Vladimir Aksyuk: **Optical Probe for Nondestructive Wafer-Scale Characterization of Photonic Elements**. – *Photonics Technology Letters*, Jan 2017
- Thomas Michels, William R. McGehee, Vladimir Aksyuk, and Jabez.J. McClelland: **Two-dimensional imaging and modification of nanophotonic resonator modes using a focused ion beam**. – *Optica*, Nov 2017
- Jie Zou, Houxun Miao, Thomas Michels, Vladimir Aksyuk: **Integrated optomechanical transducers as probes for atomic force microscope**. – *Proceedings, Solid State Sensor, Actuator and Microsystems Workshop*, June 5-9, 2016
- Jie Zou, Houxun Miao, Thomas Michels, Vladimir Aksyuk: **A Novel Integrated Optomechanical Transducer and Its Application in Atomic Force Microscopy**. – *Nanotechnology 2013, Chapter: MEMS & NEMS Devices & Applications*, pp. 173- 176, 2013
- Jie Zou, Houxun Miao, Thomas Michels, Vladimir Aksyuk: **Integrated silicon optomechanical transducers and their application in atomic**

force microscopy. – *Lasers and Electro-Optics (CLEO)*, 18 December 2014

- Kartik C. Balram, Thomas Michels, Bojan R. Ilic et al: **The Nanolithography Toolbox**. – *J. Res. Natl. Inst. Stand.*, 121, pp. 464-475 (2016)
- Krishna C. Balram, Thomas Michels, Bojan R. Ilic et al: **The Nanolithography Toolbox**. – *U. S. Department of Commerce, NIST Handbook*, October 2016
- Jie Zou, Marcelo Davanco, Thomas Michels, Kartik Srinivasan, and Vladimir Aksyuk: **Book chapter 11: Integrated Silicon Optomechanical Transducers and Their Application in Atomic Force Microscopy**. – *Nanocantilever Beams - Modeling, Fabrication and Applications*, Pan Stanford, ISBN-13: 978-9814613231 (January 2016)
- Jabez.J. McClelland, William R. McGehee, Thomas Michels et al: **Cold-Atom Ion Sources for Focused Ion Beam Applications**. – *Microscopy and Microanalysis*, Volume 23 (2017)

List of Patents

Listed below are patents that have been filled during my time in graduate school.

- V. Aksyuk, K. Srinivasan, H. Miao, T. Michels, and I.W. Rangelow, Microscope probe and method for use of same, US Patent No. US20140338074 A1
- V. Aksyuk, K. Srinivasan, and T. Michels, Microfabricated optical probe for integrated photonic devices, US Patent No.pending

List of Figures

Acknowledgement

First and foremost I would like to thank my academic advisors, Vladimir Aksyuk and Professor Rangelow. Vladimir for the support and guidance he has provided me throughout my dissertation, but also for the freedom he has given me to make my own mistakes. He created a space in which ideas could be explored without financial constraints. Despite his at times busy schedule, he has always made time for discussion. I have always appreciated his calm, precise and carefully evaluating manner. I have truly learned a lot during my thesis, which go beyond science itself, and thank professor Vladimir for this. Prof Rangelow for his guidance throughout my time at the university, fruitful discussion, his patience and pressure at the right time and his confidence in my to manage an international project. He found always time for the project and financial support, to allow me concentrate on my thesis. His scientific intuition and insights have always been very helpful.

CNST is truly a special place, and I have deeply enjoyed haveing the provilege to do my graduate work at such a unique institution. I have enjoyed having all these bright people around me to learn from and work with. In particular, I would like to thank Alex Liddle to create this cooperation. Robert Ilic for his support on the scientific and workaday life, for always having an open door for discussion.

Last but not least, I wish to thank a special group of people. I am fortunate to have met Anne who has enriched my life in every aspect in the last one and a half years. I thank her for all the love and support. In addition, I wish to thank my parents, my mother Renate and my father Peter and my brother Felix, for their support, love and patience during my entire time in the USA. Their support and help. In particular my father Peter, who I deeply admire, has provided me with invaluable advice and help to maneuver many challenging situations in my live. He was a constant source of inspiration and motivation for me. It is to them, I wish to dedicate this thesis.

Contents

1.0 Introduction

The measurement of physical quantities by transducing them to mechanical motion has a long history. From the usual large scale household utensils to a nanoresonator for the detection of electron spin flips [1] or single atoms [2] in science laboratories, we can find many transducer application based on the detection of mechanical motion.

In the last decades, the application area of silicon based mechanical transducer grew rapidly. This is partially driven by the extraordinary physical properties of silicon and by the major improvements in batch processing technology, driven by the integrated circuit industry.

The advancements in fabrication technology of micro- and nanomechanical resonators continued this trend [3]. Ongoing miniaturization and better process control have enabled high quality factors for both optical and mechanical resonators and therefore more sensitive measurement of microscopic physical phenomena. This progress allowed for the extension of detection limits and thereby enabling measurements with an unprecedented degree of precision [4].

One major obstacle in the ongoing process of further miniaturization is the reliable motion readout of small resonator structures with high sensitivity, high bandwidth and without excess power dissipation.

In the past decades, numerous methods for the readout of resonator motion have been developed. Electrical readout schemes, such as capacitive [5–8], magnetomotive [9–11], piezoresistive [12–15] and piezoelectric [16, 17], are convenient but suffer from various combinations of poor scal-

ing with reduced size, power dissipation limitations, magnetic field, material requirements, and thermal Johnson noise in the readout signal, as summarized in [18].

On the other hand, optical readout schemes, such as beam deflection [19, 20] and interferometry [21–24], substitute optical shot noise for thermal noise, in principle don't dissipate any power at the transducer, and have a high measurement bandwidth. However, to effectively couple motion to light, most of the off-chip optical methods need a certain minimum moving structure size and reflectivity, which often involves bulky structures or mechanically dissipative reflective coatings.

Integrated cavity optomechanical systems can overcome this obstacle with the direct integration of the transducer readout and optomechanical coupling to the resonator motion.

1.1 Cavity Optomechanics

Optomechcanics displays in general parametric coupling between the mechanical displacement x of a mechanical motion and the energy stored inside a localized optical-frequency electromagnetic mode of an optical micro- or nano-cavity. That is, the frequency of the localized optical-frequency electromagnetic mode depends on the x and can be written as $\omega_{opt}(x)$.

A central part of cavity optomechanical systems are optical microresonators [25]. Optical microresonators have a long and successful history as ultra-sensitive detectors, mainly thanks to enhanced light-matter interactions resulting from their appreciable photon lifetime and optical field confinement. These properties generated a tremendous research progress in disparate fields of optical science, such as all-optical nonlinear switching [26–28], modulators [29–31], all-optical signal processing [32–34], biochemical sensing [35–37], slow-light structures or optical buffers [38–44], wavelength division-multiplexed (WDM) optical filters for optical networks and on-chip optical interconnects [45–52] and in fundamental experiments in quantum physics, e.g. cavity quantum electrodynamics (QED) [53]. All of the above applications are made possible by the strong light confinement in a small modal volume. By adjusting the shape, size, and material composition, the microresonator can be designed to support a wide spectrum of optical modes with required polarization, frequency, and field patterns.

There are two well-established mechanisms of light confinement and guidance inside the volume of an optical microresonator. The first is the conventional mechanism of total internal reflection (TIR) and the existence of evanescent waves, where the guiding medium must be optically denser, i.e. have a higher refractive index, than the surrounding one in order to achieve light confinement. The second is the photonic bandgap (PBG) found in artificial optical media having a spatial periodicity in one, two or three dimensions, termed photonic crystal (PC) [54–57]. The light can be confined in a size comparable to its wavelength (λ/n), where λ is the vacuum wavelength and n is the medium refractive index.

One resonator type based on the phenomena of continuous light TIR along the boundary of a rotationally symmetric optical medium, e.g. microdisk [58–60], microsphere [61–63], and microtorus [64–66], is the whispering gallery (WG) microresonator.

1.1.1 Resonator Material

Fabrication of WG resonators has been carried out for a variety of material systems such as silica (SiO2), silica-on-silicon, silicon (Si), silicon-on insulator (SOI), silicon nitride (SiN) and oxynitride (SiON), polymers [67, 68], semiconductors such as GaAs [69, 70], ZnO [71], InP [72], GaInAsP [73], GaN [74, 75], and crystalline materials such as lithium niobate (LiNbO3) [76] and calcium fluoride (CaF2) [77]. All these key materials have their own advantages and disadvantages in terms of their linear and nonlinear functionalities, their ease of fabrication processing, and the range of refractive index contrasts that determine the allowable sizes of the resonator features.

Silica glass has a wide transparency window (from visible to infrared), low intrinsic loss and is also compatible with fiber-optic technology. The fabrication of silica microspheres (or microtoruses) is generally based on the surface tension mechanism, which forms atomically smooth surfaces leading to ultrahigh-Q-factors. The index contrast between silica and air is small in comparison to silica and semiconductor materials (InP, GaAs, Silicon, etc), thus the cavity size scales inversely. Due to the exceptionally high-Q-factor generated by this material, several parametric processes have been demonstrated at ultralow power, such as Raman lasing [78, 79],

erbium-doped lasing around 1.5 µm [80] and green up-conversion lasing [81]. Microspheres fabricated by melting the tip of an optical fiber are generally difficult to integrate on planar chips. A better integrability is offered by silica-on-silicon fabrication technology where microtoroid and microdisk resonators are formed by heating the top silica part of short silicon posts acting as supports.

In SOI technology one can have a much larger index contrast (Si/-SiO2 3.45/1.45) compared to that in silica technology, which enables the fabrication of resonators with reduced dimensions [82, 83]. In terms of fabrication the SOI material system is perfectly compatible with CMOS-based processing, which has been well established for deep-submicron electronic chips [84, 85]. The fact that silicon is transparent for $\lambda > 1.1$ µm makes SOI-based resonators suitable for telecommunication wavelengths and propagation losses of 0.8–3 dB/cm [86] have been demonstrated using CMOS-compatible processes. The higher field confinement, in a silicon resonator, does also minimize optical losses to the mechanical counterpart in the optomechanical transducer.

1.2 Dissertation Organization

Chapter 2 describes the major parts of the transducer platform. Chip integration and an overview of the fabrication process are discussed.

In Chapter 3, transducer design, optical setup and the characterization results for the different probe designs are presented. The discussion is focused on displacement sensitivity, frequency stability and readout tuning.

Chapter 4, shows the performance of the developed probe in a commercial scanning probe microscope. In single probe and probe array configuration.

Chapter 5, introduces an optical probe for nondestructive wafer-scale optical characterization of photonic structures. Design and setup are presented and the measurement results are discussed.

In Chapter 6, frequency stability of membrane transducers is studied to show an alternative platform for the investigation of the origin of frequency fluctuations.

Chapter 7, presents an acceleration sensor based on optomechanical readout. Design and fabrication of the transducer is discussed first experimental results are presented.

In Chapter 8, a study of the influence of Li^+ ions implanted in the silicon microdisk resonator is presented. The optical and thermal response of a microdisk resonator to pulses of low energy ions from a focused beam was imaged. This enabled direct imaging of the device's optical mode intensity in the linear response regime with both higher sensitivity and speed. With higher cumulative dose, persistent editing of mode spectra and spatial patterns is demonstrated.

2.0 Device Fabrication

In this chapter the general transducer structure is introduced. The critical aspect of low loss optical coupling to the micro chip is discussed in detail. For the fabrication process only an overview is provided, while further details can be found in appendix B and [87].

2.1 Transducer Structure

The presented transducer platform is based on a silicon microdisk cavity, evanescently coupled to an on-chip waveguide. The light trapped in the microdisk volume is made to interact for a longer time, in close proximity with the mechanical resonator. Typical photonic cavity optical quality factors on the order of 10^5 to 10^6 increase the readout signal-to-noise by the same factor. The readout bandwidth is reduced from $\approx$ 100 THz optical frequency to about $\approx$ 100 MHz, which is still fast enough for most mechanical sensors.

Maintaining stable coupling of a microscopic mechanical resonator with an off-chip optical cavity is challenging due to alignment and drift of components with respect to each other. Here, this challenge is overcome by integrating the high quality factor optical cavity directly underneath the moving device. This allows strong interaction with the optical near-field of the cavity, while avoiding mechanical contact (Figure 2.1). This interaction is described by the optomechanical coupling coefficient (g_{OM} typically $\frac{GHz}{nm}$) relating the change in optical frequency of the microdisk cavity to the displacement of the mechanical device. This fully integrated stable and

practical optomechanical transducer is fiber coupled and implements the readout of mechanical motion with gigahertz bandwidth. Low-loss, stable and robust fiber coupling of the transducer is essential to allow sensitive and reliable operation. (This will be discussed in the next section)

This readout approach allows independent tailoring of the various optical and mechanical parts of the transducer. The photonics can be separately optimized for low losses, high quality factor and desired cavity size. This scenario allows for tuning the waveguide-cavity coupling depth and the optomechanical coupling to achieve the optimal readout sensitivity and dynamic range. The mechanical components' size, shape, stiffness, and resonance frequency can be tailored to best address the specific sensing applications.

The actuation can be tailored for the needed displacement and force ranges, ideally without introducing mechanical losses, avoiding increased mechanical noise and decreased mechanical quality factor (Q_m) in resonators.

Two different transducer actuations schemes, bimorph and electrostatic actuation, have been characterized.

Bimorph actuators deliver fast responses and large forces. However, the introduction of metal on the mechanical structure creates significant internal losses and therefore reduces the mechanical quality factor drastically.

In contrast, electrostatic fringe field actuation doesn't need any metal in contact with the mechanical member, which lets the mechanical member freely oscillate and doesn't affect the mechanical quality factor. However, the maximum forces, as indicated by simulation, are rather small, but still suitable on-resonance excitation for frequency sensing [88, 89].

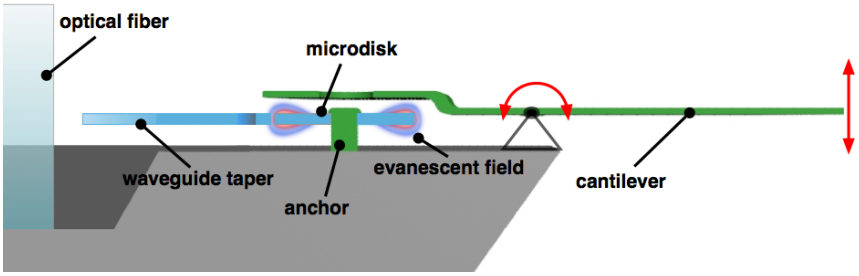

Figure 2.1: *Schematic illustration of the transducer (not to scale) showing overhung cantilever on a torsional pivot as the mechanical device. SiN is shown in green, Si is shown in blue and grey. The red arrow indicates the direction of motion.*

2.2 Chip Integration

The transducers utilizing the optomechanical readout in this work take the form of a microchip device. Through this architecture offers a number of significant benefits, such as sophisticated fabrication processes, large scale integrateability and a high degree of tailorability, a fundamental challenge lies in the efficient coupling of light from conventional optical setup (e.g laser, polarizer, optical fibers) to the chip-based device. The losses result from mode-size and effective-index mismatch between the optical fiber and the Si waveguide structure, which induce optical scattering and back-reflection.

The premise of the V-groove coupler is to provide an on-chip optical fiber alignment feature [85, 86], which allows a fiber to couple to a device with high efficiency before being permanently fixed in place. This pre-alignment removes the need for in-situ fiber positioning.

Minimizing optical loss is important for many applications of the probe. Alternative approaches for fiber connectorizing these devices have to be weighed carefully. In this case robustness and small size were major considerations, dictating end-fire coupling with fibers parallel to the chip surface, as opposed to the grating coupler geometries with fibers near-normal to the chip surface. The coupling loss achieved between the on chip waveguide and the optical fiber is ≈ 5.5 dB per facet, and also agrees well with the numerical predictions. The limited thickness of bottom oxide cladding (≈ 2 µm) further dictated the need to suspend the inverse taper to avoid losses into

the substrate. Simulations for the coupling efficiency with fiber end-fire coupling in the presence of the SiO_2 cladding and Si substrate showed much lower coupling efficiency, because of high optical losses into the Si handle wafer. One interesting direction for further reduction of optical losses is the approach described by Tiecke et.al, showing that the coupling between a fiber, which is tapered down to a narrow tip, laying on top of the waveguide can reach a high efficiency [90]. However, this approach shows some challenges in the device fabrication and packaging, which limits the potential for robust waveguide / fiber coupling. Another promising approach for the coupling could be the use of lensed fiber array to couple to the chip [91].

2.2.1 Coupler Design

The V-groove design takes advantage of the anisotropic etch properties of silicon, which allows V-shaped features to be defined by preferred crystal planes of the Si handle wafer. The depth and wall-angle of the V-groove alignment feature determine the height at which an optical fiber (cladding diameter of ≈ 125 µm) will sit when placed in the groove. Appropriate choice of the groove dimensions places the center of the ≈ 9 µm diameter fiber core at the same height as the center of the ≈ 260 nm Si film of the Silicon-on-insulator (SOI) wafer. The fiber is cleaved to produce a flat-facetted tip from which the optical mode is launched towards the device. A mode-converter consisting of an adiabatically-tapered Si waveguide [92–97] is used to mode-match the fiber-launched optical beam to the waveguide mode. The individual parts of the optical coupler are described in detail in the following sub-sections, in order corresponding to the propagation of light from the input optical fiber to the on chip waveguide.

2.2.1.1 Waveguide Tip

The Si waveguide is fiber-end coupled to a cleaved optical fiber (Corning SMF-28e) tip. The positioning of the fiber in the alignment groove feature aligns the glass fiber to the y and z position of the index waveguide tip, while the separation in x is kept below 10 µm. Mode-matching between the Corning SMF-28e optical fiber and the Si waveguide tip is accomplished by determining the waveguide cross-section, which supports an evanescent field matching the 10.4 µm fiber mode-field diameter [93, 96–98]. The

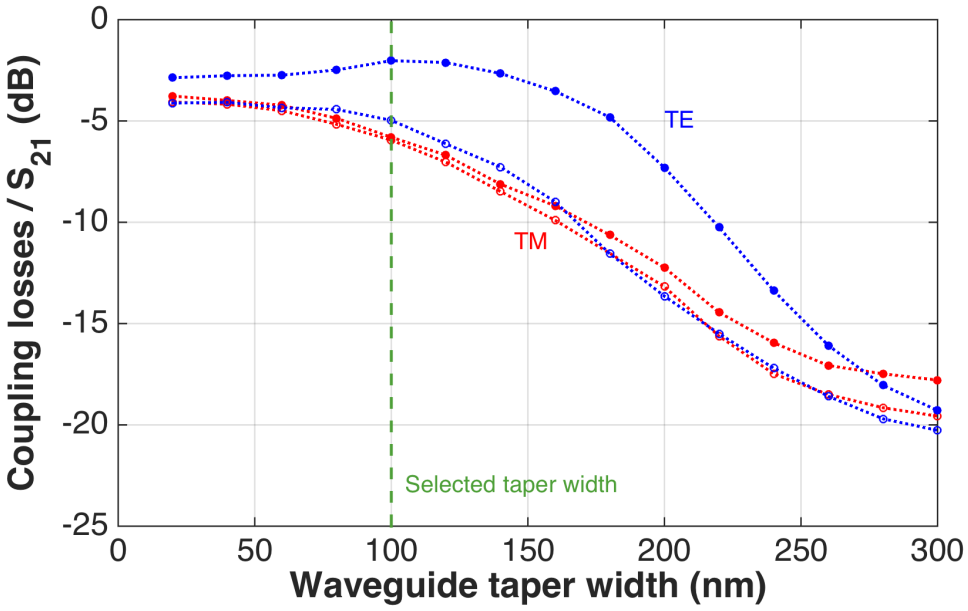

Figure 2.2: *Simulation result of the transmission (S21) as a function of taper tip width. The inverse taper length is 65 μm. The results for the TM polarization are red and the results for the TE polarization are blue. The filled marker represent the results without silicon support tethers and the circle represent the results for the simulation model with silicon support tethers.*

transmission efficiency through this junction is given by the mode overlap integral

$$\eta_{overlap} = Re\left(\frac{\int E_1 \times H_2^* \cdot dS \int E_2 \times H_1^* \cdot dS}{\int E_1 \times H_1^* \cdot dS \int E_2 \times H_2^* \cdot dS}\right) \tag{2.1}$$

where E and H are respectively the electric and magnetic fields of the optical modes supported by the fiber (subscript 1) and Si index waveguide (subscript 2). While the waveguide thickness is fixed at 260 nm, tuning of the waveguide width w_{tip} can be used to optimize Equation 2.1 via Finite Element Method (FEM) simulation. Figure 2.2 shows the simulation result for the transmission (S21) as a function of taper width. A width of ≈ 100 nm is found to produce the optimal transmission at the target wavelength of 1550 nm. This is also a reasonable size for the electron beam lithography used to define the waveguide taper. The taper nominal length is 65 μm.

2.2.1.2 Waveguide Taper

As the optical mode propagates along the silicon waveguide (in x- direction), the waveguide gradually widens from a tip width of ≈ 100 nm to a final width of $w \approx 500$ nm. This has the effect of confining the optical mode in the dielectric to a mode profile similar to the fundamental optical mode of the waveguide. To accomplish this mode conversion efficiently, an adiabaticity condition

$$\frac{dw}{dx} \ll |n_{eff,i} - n_{eff,j}| \qquad \forall i \neq j \tag{2.2}$$

is enforced, where $n_{eff,i}$ is the effective refractive index for an arbitrary waveguide mode. This condition ensures that light in the preferred optical mode does not couple to other modes of the structure, which could cause loss in propagation. Finite- difference time-domain (FDTD) simulations of the waveguide show that the adiabatic condition for this device is reasonably met when w as a function of x expands linear. Figure 2.3 show the dependence of the mode shape for the two main polarizations (TE and TM) in respect to the waveguide width for a silicon waveguide in air, with a waveguide height of 260 nm.

Since the mode size and effective index of the taper strongly depend on the surroundings of the nanotaper, an overhanging nanotaper in air has been chosen, avoiding the possibility of increased losses into the nearby substrate. Figure 2.4 shows a comparison of the coupling losses of a waveguide taper in air to one with a substrate below. By making the total length of this waveguide taper greater than 60 µm, the optical loss in the mode conversion plus coupling can be kept below 60 % .

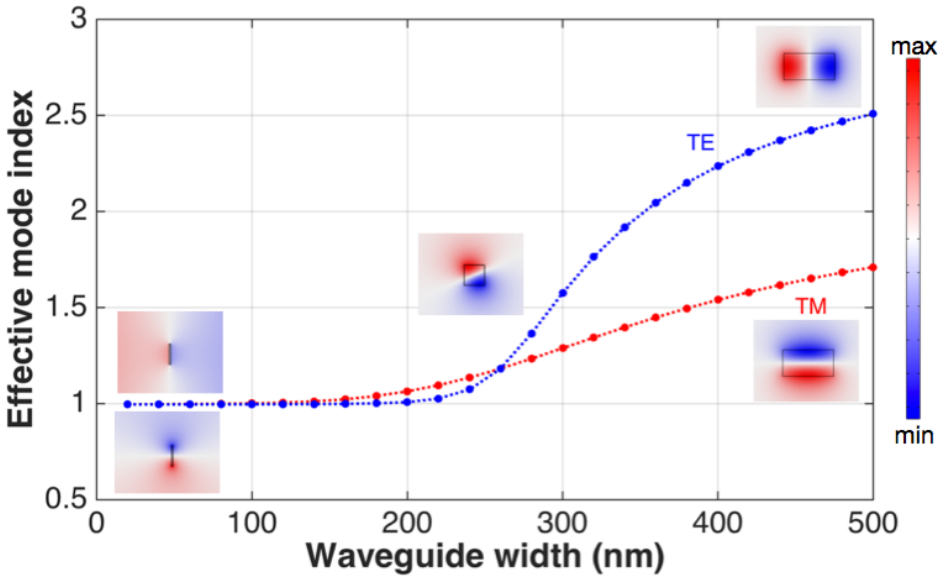

Figure 2.3: *Simulation result for the effective mode index for the two main polarisations (TE and TM) of a silicon waveguide in air as a function waveguide width between 20 nm and 500 nm and a waveguide height of 250 nm. The insets show $|E^2|$ for the TE and TM mode at 20nm, 250nm, and 500nm.*

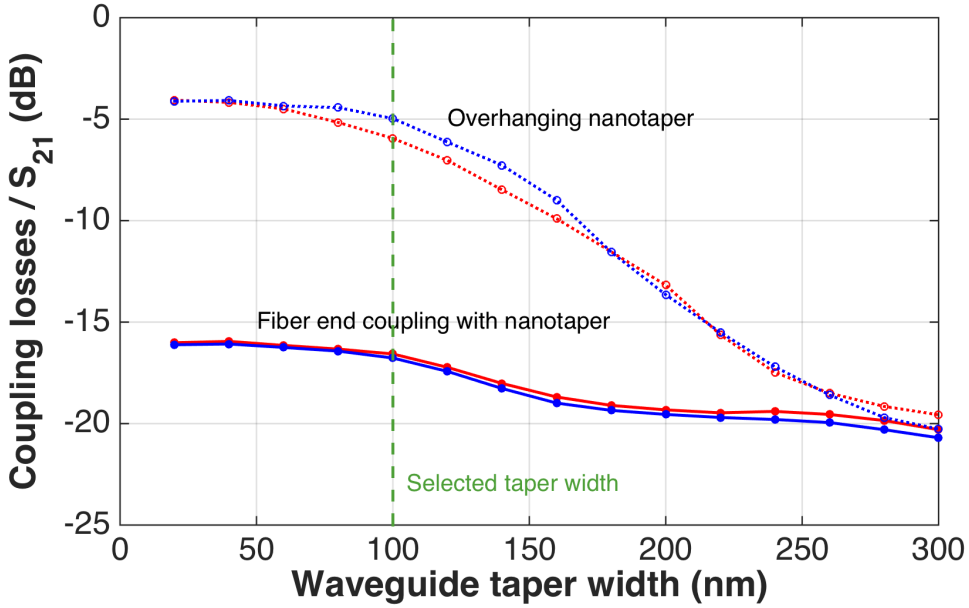

Figure 2.4: *Simulation result of the transmission (S21) as a function of taper tip width (w_{tip}). The inverse taper length is ≈ 65 µm. The results for the TM polarization are red and the results for the TE polarization are blue. The circle represent the results for the overhanging nanotaper with support structure and the filled marker represent the results for the simulation model with fiber-end coupling into the nanotaper with substrate below.*

2.2.1.3 Support Tether

In order to prevent mechanical bending modes of the waveguide taper from coupling optically and adding spurious signals to the probe bending modes of the microdisk resonator, two tethers are used to secure the waveguide along the 65 µm taper section (Figure 2.5). The tethers are supported by large sections (≈ 20 µm x 65 µm) of silicon to add stiffness and mechanical damping to this junction.

The first support tether spans ≈ 9 µm distance between the plates and fixes the waveguide taper at a distance of ≈ 6 µm from the tip. Since the mode is significantly extended at this point, scattering at the tether junction causes optical loss. The amount of scattering depends strongly on the width of the tether feature. Tethers can be reproducibly fabricated at a width of ≈ 80 nm to avoid excessive scattering losses. The second tether is used to damp the mechanical oscillations of the waveguide taper. This tether spans ≈ 2.5 µm distance between the support structures, in an area where the waveguide taper already reached the final width of ≈ 500 nm. As the mode is already concentrated in the beam waveguide the optical losses caused by the tether are minimized (Figure 2.3).

The results of the mechanical eigenfrequency simulations compared to measurement results on the final devices are summarized in Table 2.1. Figure 2.5 (left) shows simulation results for the mode shapes of the first four mechanical eigenfrequencies for the silicon nanotaper. The colored scanning electron micrograph in Figure 2.5 (right) shows the final geometry of the released nanotaper.

Furthermore, the gap between waveguide taper and support structure was widened toward the coupling point to minimize coupling of the evanescent fields of the mode to the Si support structure.

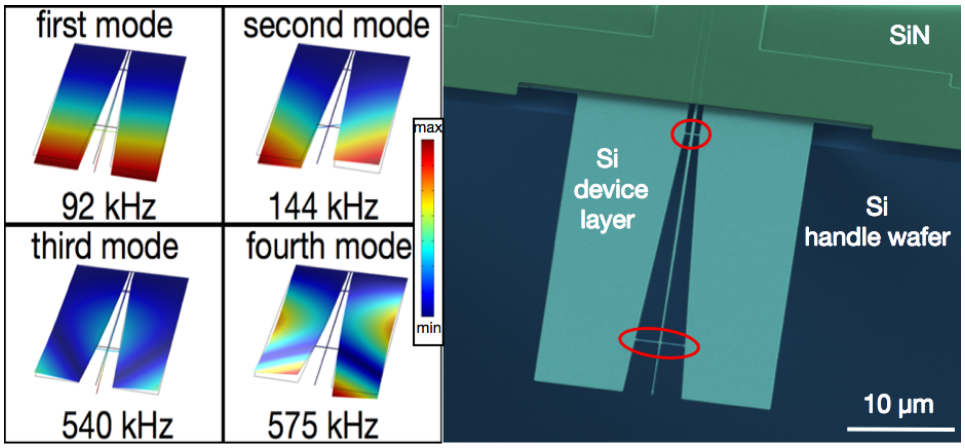

Figure 2.5: *(left) Simulation result for the first four mechanical eigenfrequencies of the silicon nanotaper.(right) Colored scanning electron micrograph image of the released nanotaper. The red circles highlight the silicon support structure to hold the nanotaper in place.*

Mode	f_{res} (Simulation)	f_{res} (Measurement)
1st	92 kHz	92 kHz
2nd	144 kHz	138 kHz
3rd	540 kHz	548 kHz
4th	575 kHz	572 kHz

Table 2.1: *Simulation results for the first six mechanical eigenfrequencies of the nanotaper with the corresponding measured resonance frequencies of a released device. The values have been measured with a laser doppler vibrometer at a pressure of ≈ 5 mPa.*

2.3 Overview of the Fabrication process

The main challenge is to fabricate these diverse optical, mechanical and electrical structures in a unified batch fabrication process and a single platform, which can be tailored for specific applications. In the following, the process will be presented using the overhanging cantilever probe as an example [99].

The fabrication of the cavity optical transducer is based on double-side polished SOI. The process flow is summarized in Figure 2.6. In the first step, the waveguide taper, waveguide and micro disk are defined via electron beam lithography and inductively-coupled reactive ion etching (RIE) of the SOI device layer down to the buried oxide layer (BOX). The nominal width of the waveguide is ≈ 500 nm and the gap between the waveguide and the disc is defined to be ≈ 340 nm.

Both waveguide ends are linearly tapered down to a width of ≈ 100 nm over the distance of ≈ 65 µm for low loss coupling to/from optical fibers (≈ 5.5 dB per facet) (Figure 2.6 (b)) [99]. The remaining structures are defined by i-line stepper optical lithography unless otherwise noted (ASML PAS 5500/275D). A sacrificial silicon dioxide layer (≈ 1 µm) is deposited in a low-pressure chemical-vapor deposition furnace (LPCVD) and defined to create a window to the Si substrate for the later KOH etching as well as a hole in the center of the microdisk, which is used to anchor the microdisk to the bulk silicon with the following SiN layer.

The silicon dioxide is thinned down by a CF_4 plasma etch through a lithographically-defined window in photoresist in the region above the micro disk to ensure good optomechanical coupling (Figure 2.6 (c,d)).

A low-stress silicon nitride layer (≈ 400 nm) deposited with LPCVD acts as a passivation layer in the waveguide region and as a structural material for the mechanical structure. Following nitride deposition, a gold layer is deposited and defined in a liftoff process to create a micro heater, electrical connection and wire bond pads. (For the electrostatically actuated transducer, the micro heater is replaced by electrodes for fringe field actuation). The SiN layer is lithographically patterned (Figure 2.6 (e)), and dry etched to form the SiN cantilever, SiN ring above the micro disk, and SiN anchor to mechanically attach the micro disk to the bulk silicon.

The previously defined metal layer is used as a hard mask for SiN,

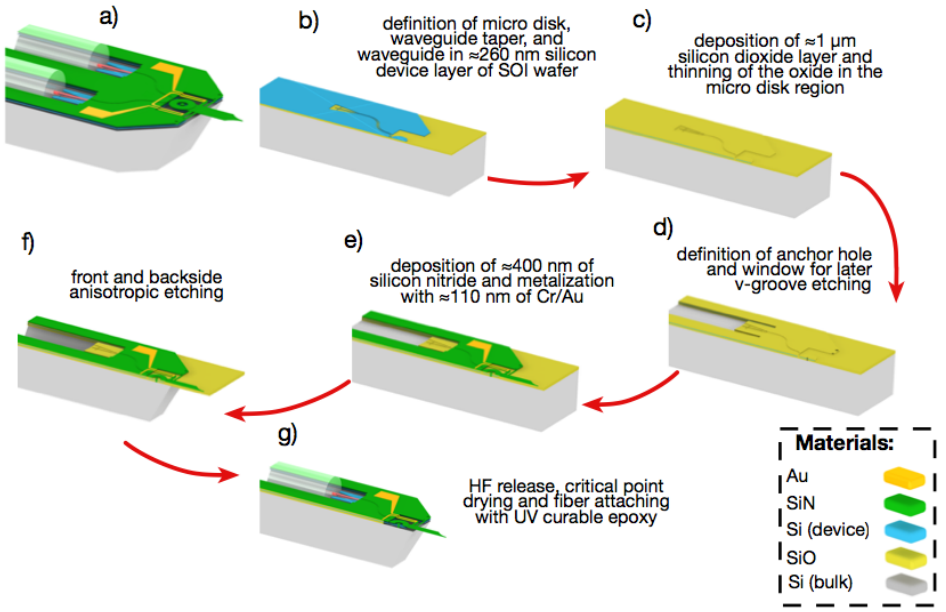

Figure 2.6: *Representation of the process flow for the transducer with integrated thermal actuation and overhanging tip. The image in the top left shows the finished device (a). (b) Definition of micro disk, waveguide taper, and waveguide in ≈ 260 nm silicon device layer of SOI wafer. (c) Deposition of ≈ 1 µm silicon dioxide layer in micro disk region. (d) Definition of anchor hole and window for later V-groove etching. (e) Deposition of ≈ 400 nm of silicon nitride and metallization with ≈ 110 nm of Cr / Au. (f) Front and backside anisotropic etching. (g) HF release, critical point drying and fiber attaching with UV curable epoxy.*

to self-align the SiN structure in critical areas (Figure 2.6 (e)). For front side protection during the later KOH etch, a hafnium oxide (HfO) layer is deposited with atomic layer deposition. In the following, a RIE is used to open up a window in the HfO and SiN for anisotropic etching of the silicon, and to form v-grooves for optical fibers. A back to front aligned backside lithography followed by RIE etching is used to form an anisotropic etch window on the backside as well.

Both lithographies for the definition of the front and backside etch window for anisotropic etching are defined with contact aligner lithography. During the anisotropic silicon etch, V-grooves are formed on the front side of the chip and the shape of the cantilever chip is defined by etching through the handle wafer from the backside (Figure 2.6 (f)). (Another approach is the replacement of the backside KOH etch with an ICP etch to create a backside trench with vertical sidewalls. This approach is currently being used to develop acceleration sensors with large seismic masses made from the handle wafer.)

Silicon dioxide layers and HfO are removed by 49 % HF wet etching to undercut and release the movable structures as well as the microdisk, which is anchored to the bulk silicon with a SiN anchor. A critical point drying process is used to avoid stiction between the parts due to capillary forces (Figure 2.6 (g)). At the end of each V-groove the overhanging waveguide inverse tapers are suspended between silicon support structures and coupled to optical fibers. Which are placed in the V-groove, actively aligned and glued into place with ultraviolet (UV) light curable epoxy.

2.3.1 Contrast Cold-Warm-Development

The electron beam lithography process is based on a cold development process. Cold development has the advantage of higher resist contrast during the development process, which results in higher geometric fidelity as shown in Figure 2.7. Figure 2.7 (a) shows the nanotape after the transfer into the silicon device layer and after the removal of the resist, developed at room temperature. The nanotaper shows round edges, which is caused by the lower contrast in the development process. These rounded corners have a significant influence on the optical coupling performance of the fiber/waveguide taper. Figure 2.7 (b) shows the same structure developed

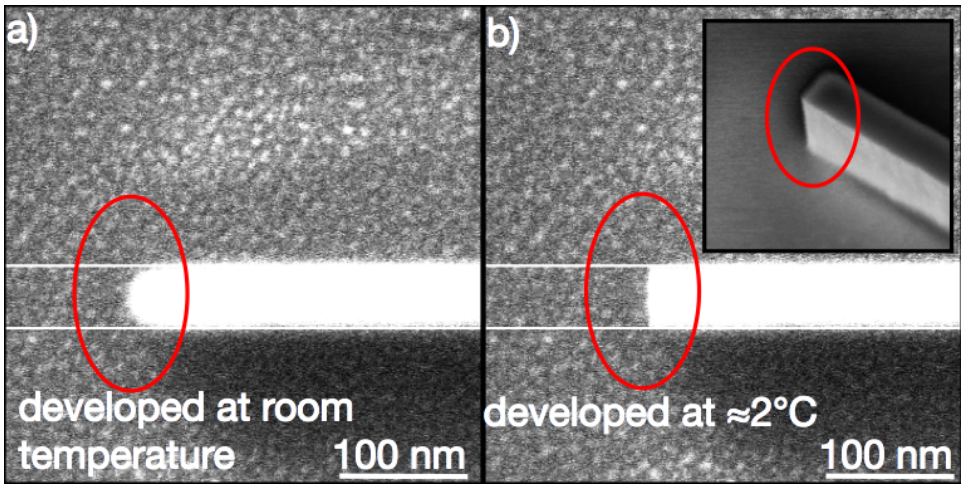

Figure 2.7: *(a) Shows the nanotaper after the transfer into the silicon device layer and the removal of the electron beam resist. The electron beam resist for this chip has been developed at room temperature. (b) Shows the same structure written with a higher dose and developed at ≈ 2 °C. The red circles highlight the coupler edges which have a significant influence on the coupling performance of the nanotaper. The inset shows the nanotaper in an angle to inspect the sidewall roughness of the etched structure.*

at ≈ 2 °C and again transferred into the silicon device layer and after the resist strip. The geometric fidelity of the nanotaper is much higher, which results in sharp corners and vertical sidewall (inset).

2.4 Conclusion

The chip integration for the optical parts has been discussed. FEM simulations were performed to verify the design of critical transducer parts and to optimize the geometries. The approach of full silicon integration of all nanophotonic components with mechanically separated high quality factor movable components creates the opportunity to independently tailor optical, mechanical, and the actuation parts for a variety of MEMS and NEMS sensing applications that require high precision, high bandwidth, and small footprint. Additional benefits of the photonic readout approach are low power dissipation at the sensor, insensitivity to electromagnetic interference, and robustness of fiber-connectorized devices.

The provided overview of the fabrication process focuses on critical points, e.g. electron beam lithography, waveguide cladding etc., that maximized device yield.

3.0 Transducer Designs

This chapter will provide an overview of the transducer designs as well as the general optical setup used to characterize the transducers. Important characteristics of the optomechanical transducers are explained and discussed.

The results presented are a summary of all characterization experiments, more extensive collection of transfer functions and measured mechanical frequency noise spectra, in air and vacuum, can be found in the appendix C.

3.1 Optomechanical Coupling (g_{OM})

The integrated optomechanical readout (Figure 3.1) utilizes near-field interaction as a probe of transducer motion. The silicon microdisk used in this transducer platform is a device that supports whispering gallery optical modes. These modes circulate around the microdisk edge and have evanescent tail that extends out into the surrounding air cladding. Introducing a probe into this evanescent region induces a shift in the optical mode frequencies ω_{opt}, with the amount of shift depending on the specific location of the probe with respect to the disk. Thus, as the probe vibrates, the resonant frequency of a given optical mode varies and this in turn can be mapped to a varying optical intensity in a number of ways. One straightforward approach is to use a laser that is tuned to the shoulder of the cavity mode optical resonance. Alternately, measurements of phase on resonance with

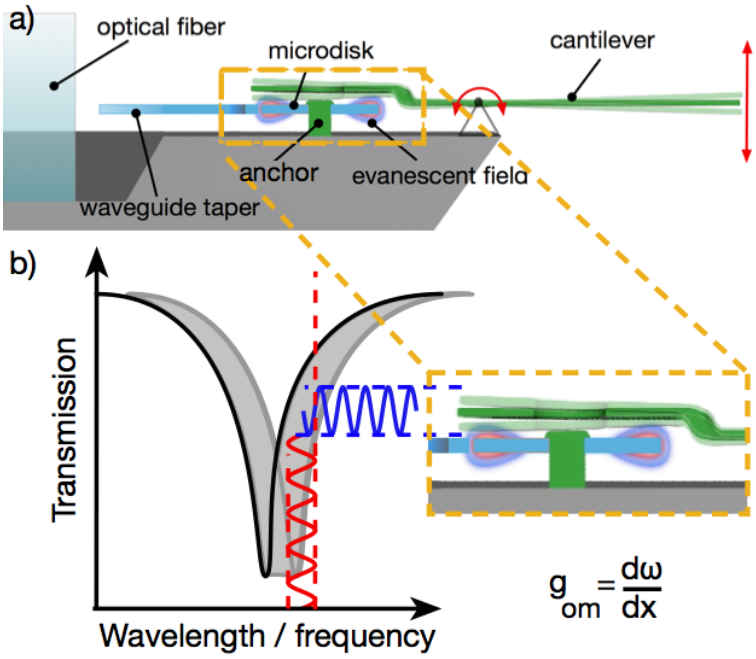

Figure 3.1: *(a) Schematic illustration of the transducer (not to scale) showing overhung mechanical probe on a torsional pivot as the mechanical device. The device illustration shows the arrangement of the different components in our transducer, such as the optical fiber, inverse-taper coupler, waveguides, microdisk cavity, and the mechanical (torsional probe) structure. (b) Using a tunable laser whose wavelength is aligned to the shoulder of an optical mode enables fluctuations in the cavity mode optical frequency due to probe motion to be mapped to an intensity-modulated optical signal.*

the cavity mode can be used.

This approach is characterized by serval parameters which determine the readout sensitivity. The optomechanical coupling (g_{OM}) is defined by the change of the optical microdisk resonance frequency in respect to the movement of the mechanical structure in the optical near-field. This parameter is co-determined by the optical quality factor of the microdisk, which defines the slope of the optical resonance dip.

For $ResBW \ll \frac{f_{res}}{Q_m}$ [100]

$$|g_{OM}| = |\frac{\partial \omega_{opt}}{\partial x}| = |\frac{\partial \frac{2\pi c}{\lambda}}{x}| = |\frac{2\pi c}{\lambda^2}\frac{\partial \lambda}{\partial x}| = \frac{2\pi c}{\lambda^2}\,|\frac{dT_{opt}}{d\lambda}|^{-1}_{\lambda_{probe}}\,\frac{\sqrt{\frac{S_V}{S_Z}}}{V_0} \quad [\frac{GHz}{nm}] \quad (3.1)$$

$$S_Z = \frac{4k_B T Q_m}{k 2\pi f_{res}} \quad [\frac{m^2}{Hz}] \quad (3.2)$$

with $ResBW$, λ, x, c, T_{opt}, T, V_0, S_v, k_B, f_{res} and k being the resolution bandwidth, optical wavelength, displacement, speed of light, transmission, temperature, photodiode voltage, Boltzmann constant, mechanical resonance frequency and spring constant of the desired mechanical mode respectively. The transmission T_{opt} is measured as the detector voltage (V). V_0 corresponds to the voltage at maximum transmission.

For $ResBW \gg \frac{f_{res}}{Q_m}$ [101]

$$V_{rms} = \sqrt{P * Impedance} \quad [V] \quad (3.3)$$

$$|g_{OM}| = \frac{2\pi c}{\lambda^2}\,|\frac{dT_{opt}}{d\lambda}|^{-1}_{\lambda_{probe}}\,\frac{(\frac{V_{rms}}{x_{rms\ disk}})}{V_0} \quad [\frac{GHz}{nm}] \quad (3.4)$$

The result of a 2D numerical simulation of the optomechanical interaction focusing on the TM polarization, as these modes should be especially sensitive to changes in the ring-disk gap, is shown in Figure 3.2 with g_{OM} as a function of probe-disk gap.

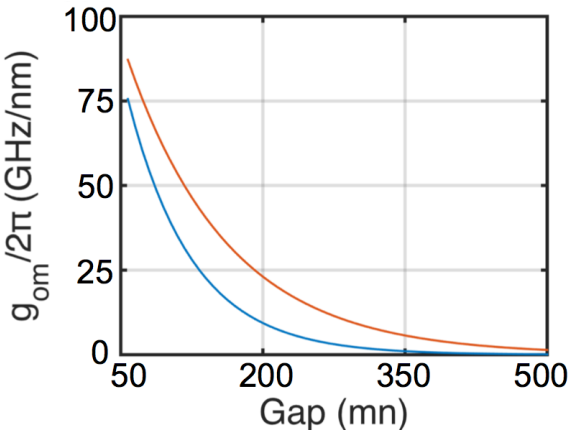

Figure 3.2: *Optomechanical coupling as a function of gap distance for $TM_{1,35}$ (blue) and $TM_{2,30}$ (red).*

3.1.1 Signal calibration

In order to determine the mechanical behavior of the transducer, we combined finite element simulation with mechanical frequency measurements of the mechanical eigenmodes to determine the effective mass (m_{eff}) and the spring constant (k) of each mode. This gives us:

$$x_{rms\ disk} = \sqrt{\frac{k_B T}{k_{disk}}} \tag{3.5}$$

with k_{disk} being the spring constant of the probe in the disk region and $x_{rms\ disk}$ being the root mean square of the thermal motion.

Figure 3.3 shows the measured mechanical frequency noise spectrum of a probe with Lorentzian fit (red). The dotted green line indicates the background noise level. Signal power is reported relative to 1 mW.

With the raw voltage signals of the photo detector (V), proportional to the vertical displacement of the probe (x), the measured voltage power spectral density was calibrated by fitting to a Lorentzian $S_{vv}(\omega)$ with an area given by the equipartition theorem.

With:

$$\alpha_{disk} = \frac{2\, x_{rms\ disk}\sqrt{\frac{Q_m}{\omega_m}}}{\sqrt{S_{vv\ peak} - S_{vv\ noise}}}\sqrt{S_{vv\ noise}} \tag{3.6}$$

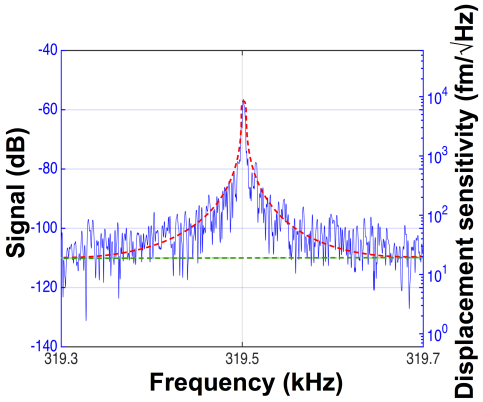

Figure 3.3: *Measured mechanical frequency noise spectrum of a probe with Lorentzian fit (red). The dotted green line indicates the background noise level. Signal power is reported relative to 1 mW.*

The transducer displacement sensitivity can be determined.

3.1.2 Calculation of g_{OM} via Boltzmann Distribution

Another approach to determine g_{OM} experimentally is the analysis of the probability distribution of the mechanical energy stored in the resonator oscillation. For this, the energy stored in the mechanical resonator was measured with a network analyzer and a sufficiently large resolution bandwidth (Figure 3.4 (a)). From the logarithmic histogram of the resonator energy the parameter α_B can be extracted as the slope of a linear fit (Figure 3.4 (b)).

The power in the resonator measred by a spectrum analyzer with input impedance 50 Ω can be described by:

$$P = \frac{(\frac{dT_{opt}}{dx})^2 x^2}{Z} = \frac{2}{Z\,k}(\frac{dT_{opt}}{dx})^2 \frac{kx^2}{2} \tag{3.7}$$

with k and Z, the spring constant and impedance respectively.

$$Ae^{-\frac{1}{k_B T}E} = Ae^{(-\alpha_B \frac{2}{Z\,k}(\frac{dT_{opt}}{dx})^2 \frac{kx^2}{2})} \tag{3.8}$$

$$\frac{1}{k_B T} = \alpha_B \frac{2}{Z\,k}(\frac{dT_{opt}}{dx})^2 \frac{kx^2}{2} \tag{3.9}$$

$$\frac{dT_{opt}}{dx} = \sqrt{\frac{Z\,k\,x^2}{k_B T\;\alpha_B\;2}} \tag{3.10}$$

With the Equation for g_{OM} (Equation 3.2)

$$|g_{om}| = |\frac{\partial \omega_d}{\partial x}| = |\frac{\partial \frac{2\pi c}{\lambda}}{x}| = |\frac{2\pi c}{\lambda^2}\frac{\partial \lambda}{\partial x}| = |\frac{2\pi c}{\lambda^2}\frac{d\lambda}{dT_{opt}}\frac{dT_{opt}}{dx}| \tag{3.11}$$

and Equation 3.10 in Equation 3.2 gives:

$$|g_{om}| = |\frac{2\pi c}{\lambda^2}\frac{d\lambda}{dT_{opt}}\sqrt{\frac{Z\,k\,x^2}{k_B T\;\alpha_B\;2}}| \qquad [\frac{GHz}{nm}] \tag{3.12}$$

The approach creates very similar results compared to the general approach described in section 3.1.

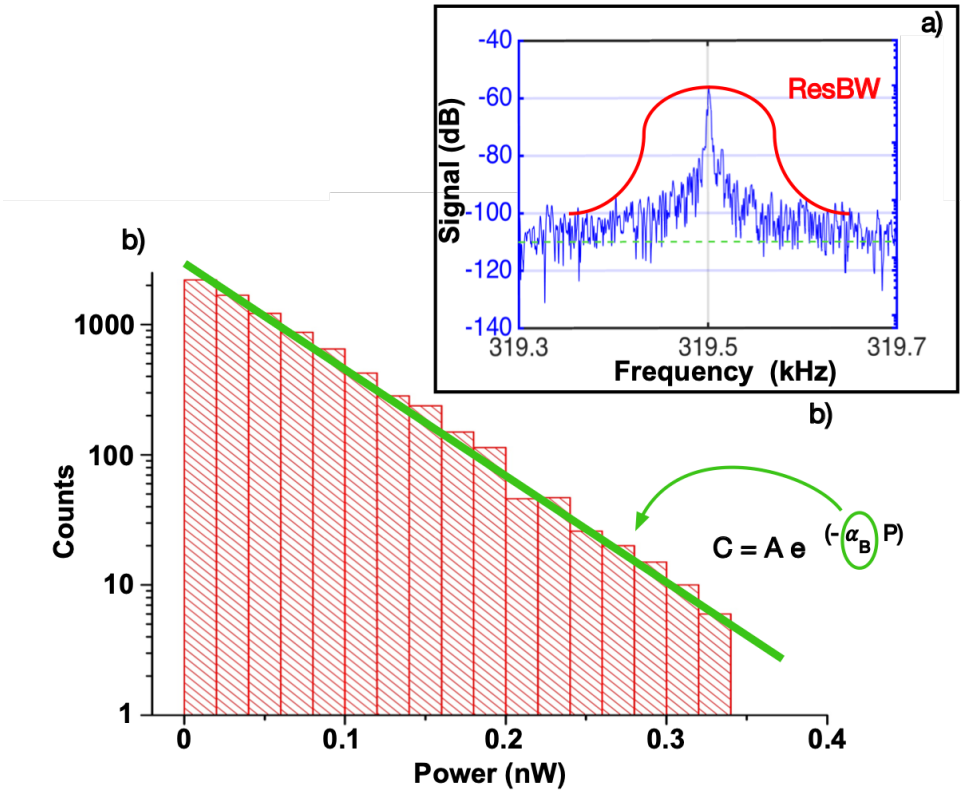

Figure 3.4: *(a) Measured mechanical frequency noise spectrum (blue) of a probe with an illustration of the resolution bandwidth (RedBW) used for the measurement (red). Signal power is reported relative to 1 mW. (b) Histogram of the measured oscillator energies with linear trend line to extract α_B (green).*

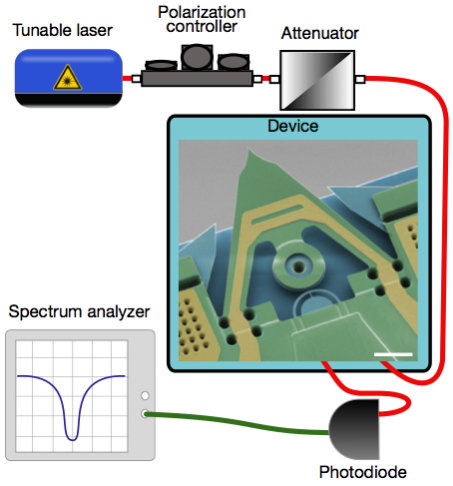

Figure 3.5: *Schematic of the detection setup with an embedded scanning probe micrograph of a probe transducer. Scale bar correspond to 10 µm.*

3.2 General Measurement Setup

The general setup used for optical characterization of the individual transducer designs is illustrated in Figure 3.5.

It starts with a tunable laser (≈ 1520 nm to ≈ 1630 nm). The light is sent through a polarization controller and coupled into the fiber pigtailed device, allowing for polarization adjustment to maximize the coupling depth of the desired optical mode before recording data. The injected light circulates hundreds or thousands of times (depending on the cavity's finesse) before exiting through the outgoing optical fiber. The output of the fiber is analyzed with a photodetector and either the transmission spectrum of the device is recorded in situation in which the laser wavelength is swept (Figure 3.6), revealing the spectral location and spectral width of the cavity's optical modes, or the transmission modulation is analyzed in situation in which the laser wavelength is fixed on the shoulder of an optical cavity mode, to detect a mechanical motion of the cantilever.

As described above, motion of the cantilever results in a frequency modulation of the optical cavity modes, which can be translated into an intensity modulation by probing these modes on the side of their resonance minima. The information obtained from the transmission spectra is thus used to determine the laser wavelength for optimal transduction sensitivity. The output signal exiting the device, which now carries the imprint of the

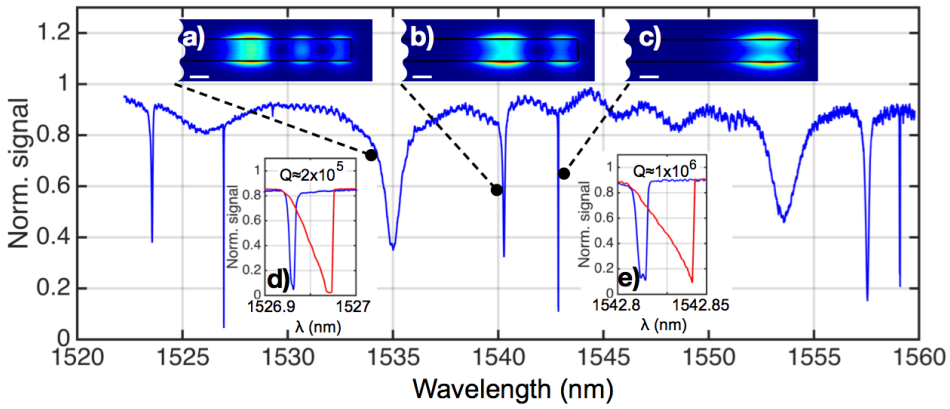

Figure 3.6: *(a), (b), and (c) finite element simulation result showing the square of transverse electrical field component and its profile of the 0^{th} order, 1^{st} order, and 2^{nd} order mode. The scales bars correspond to 200 nm. Inset (d) and (e) show travelling wave and the doublet of a standing wave. The red color shows the response at high input power and the blue at low input power.*

mechanical motion as an intensity fluctuation, is detected on a photodetector before being sent to an electronic spectrum analyzer to reveal the spectrum of mechanical modes.

The measured transmission spectrum for the transverse magnetic (TM - electric field in the radiation direction is small, because azimuthal E filed is appreciable away from the midsection of the disk) polarization of a microdisk resonator is shown in Figure 3.6. Transverse magnetic (TM) resonance modes with radial mode number from one to three can be observed in the spectra. The inset (a), (b), and (c) show the square of the transverse electrical field component and its profile of the 0^{th} order, 1^{st} order, and 2^{nd} order mode. Inset (d) shows the transmission spectrum of a travelling wave resonance mode and (e) shows the spectrum for a standing wave, at high (red) and low (blue) optical power. These doublets correspond to pairs of standing wave modes with slightly different energies, arising from mixing between clock-wise (CW) and counter-clock-wise(CCW) propagating waves. The nodal position of the lower- and higher-energy standing waves is dictated by the details of the spatial symmetry breaking disorder.

3.3 Designs

Separating photonic and mechanical layers affords flexibility in the design of the mechanical parts to suit specific sensing applications. Cantilever structures, torsional structures, and membranes, on chip structures, and overhanging structures, as well as various types of actuation mechanisms have been designed. The membrane structures are designed to have a resonance frequency ranging from ≈ 70 kHz up to ≈ 1 MHz (Figure 3.7). The cantilevers are designed to combine small size with high resonance frequencies with a range between ≈ 100 kHz and ≈1 MHz for the first harmonic. The integration of an actuator increases the range of possible applications. The built-in static actuation gives the possibility of tuning the transducer gain and measurement range. This is accomplished by changing the static gap size between the mechanical structure and the optical cavity.

Two different transducer actuations schemes, bimorph and electrostatic actuation, have been characterized. Bimorph actuators deliver fast responses and large forces. But the introduction of metal on the mechanical structure creates significant internal losses and therefore reduces the mechanical quality factor drastically. In contrast, electrostatic fringe field actuation doesn't need any metal in contact with the mechanical member which lets the mechanical member freely oscillate and doesn't affect the mechanical quality factor. However, the maximum forces, as indicated by simulation, are rather small, but still suitable for on-resonance excitation for frequency sensing.

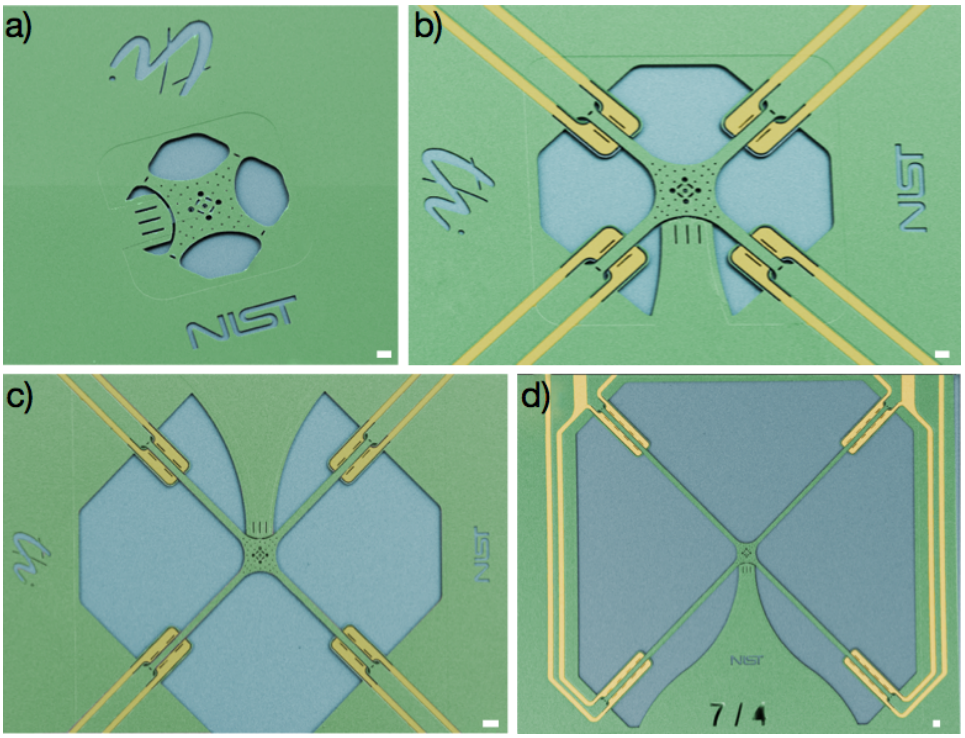

Figure 3.7: *False-color scanning electron micrographs of the membranes, showing the silicon nitride structural layer (green), metal layer (yellow), silicon device layer (light blue), and silicon handle wafer (dark blue). Four different membrane sizes were built. (a) shows a the smallest membrane without integrated actuation, the "bridges" are ≈ 60 µm long. (b), (c), and (d) show membranes with a "bridge" length of ≈ 130 µm, ≈ 300 µm, and ≈ 650 µm respectively. The membranes shown in (b), (c), and (d) have integrated electrostatic actuator, which are placed on both sides of the "bridge". Scale bars correspond to 20 µm.*

Nine different probe designs have been fabricated to study the probe performance depending on the probe shape and actuator configuration, the designs are summarized in in Figure 3.8. The structures can be grouped in electrostatically and electrothermally actuated probes, stiff and soft probes, or cantilever and torsional probes. The layout of the probes defines the probe behavior in therms of frequency stability, displacement sensitivity, and displacement amplitude. Some designs show the ability of active read-out tuning and therefore control of the dynamic measurement range and displacement sensitivity, others show a mechanical excitation connected to the supplied optical input power.

The capability for probe parallelization is demonstrated for the design # 1 and # 3. The labels used in Figure 3.8 are the design names that are used for this thesis to refer to specific probe designs.

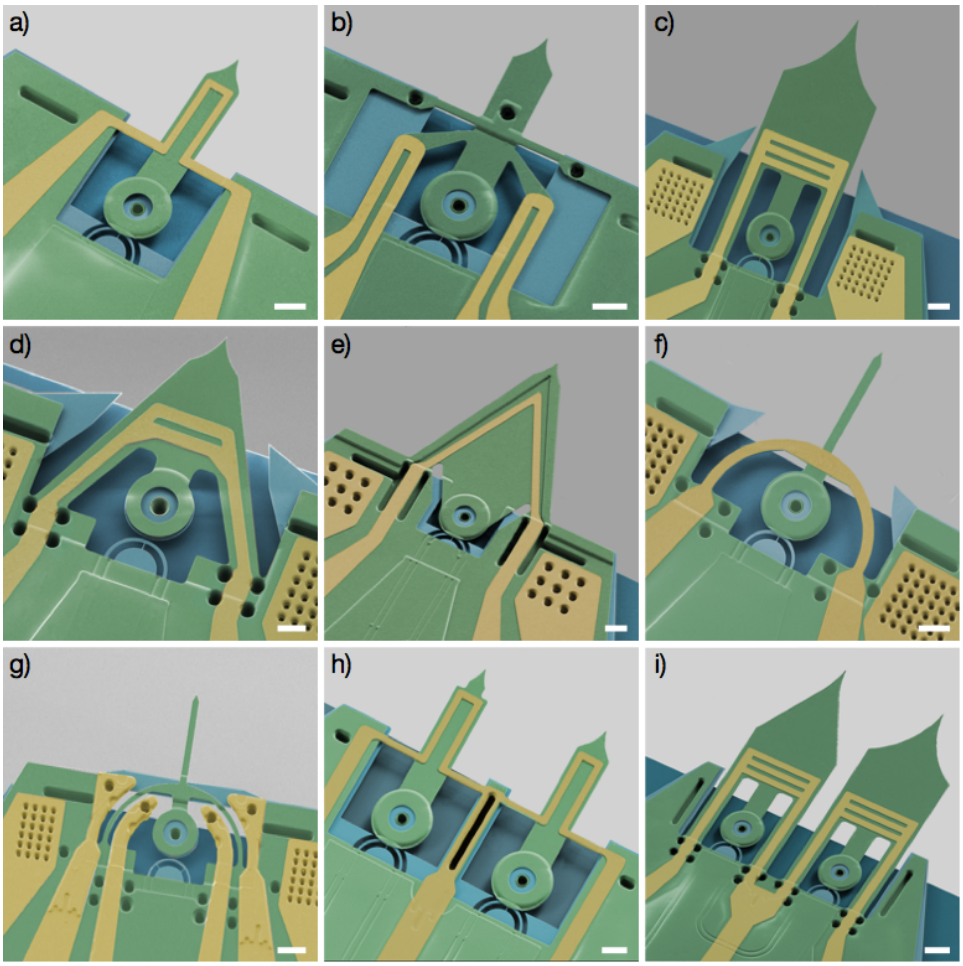

Figure 3.8: *False-color scanning electron micrographs of the release probes, to illustrate the different designs discussed in this article, showing the structural layer (green), metal layer (yellow), silicon device layer (light blue), and silicon handle wafer (dark blue). (a) Probe with torsional support and thermal bimorph actuation on the probe (Design # 1). (b) Probe with torsional support and two thermal bimorph actuators, one on each side of the probe, to allow the excitation of the probe (Design # 2). (c) Cantilever probe with rectangular shape and integrated bimorph actuator (Design # 3). (d) Cantilever probe with triangular shape and integrated bimorph actuator (Design # 4). (e) Cantilever probe with triangular shape and integrated bimorph actuator. A step in probe topography increases the stiffness of the probe (Design # 5). (f) Cantilever probe with semi-circular shape and integrated bimorph actuator. The probe is designed to reduce the effective mass without size reduction (Design # 6).(g) Semi-circular shaped probe with integrated electrostatic actuation.*

Figure 3.8 ***(previous page)*:** *(h) 2x1 array of torsional supported probes with individually addressable bimorph actuation (Design # 7). (i) 2x1 probe array with individually addressable bimorph actuation (Design # 8). Scale bars correspond to 5 µm.*

Design	Mode	$f_{res}\,[MHz]$	$\alpha_{disk}\left[\frac{fm}{\sqrt{Hz}}\right]$	$\alpha_{tip}\left[\frac{fm}{\sqrt{Hz}}\right]$	$\sqrt{S_{FF\ tip}^{thermal}}\left[\frac{fN}{\sqrt{Hz}}\right]$
# 1	**1st**	**0.537**	**8.6**	**11**	**0.25**
# 1	2nd	1.16	8.6	10	4
# 1	4th	2.66	8.6	10	1.6
# 2	**1st**	**0.825**	**3.2**	**6.4**	**2.6**
# 2	2nd	1.3	3.2	5.4	0.72
# 2	3rd	1.86	3.2	0.14	0.58
# 3	**1st**	**0.119**	**3.8**	**8.7**	**5**
# 3	2nd	0.68	3.8	3.5	3.3
# 3	3rd	1.97	3.8	4.8	1
# 4	**1st**	**0.407**	**2.5**	**36**	**0.66**
# 4	2nd	1.3	2.5	2	2.6
# 4	4th	3	2.5	21	0.65
# 5	**1st**	**0.58**	**3.3**	**11.3**	**3.8**
# 5	2nd	2.27	3.3	2.6	5
# 5	4th	3.77	3.3	4.7	5
# 6	**1st**	**0.506**	**1.5**	**42**	**0.32**
# 6	2nd	0.969	1.5	2	1.9
# 6	3rd	2.166	1.5	13	0.17
# 7	**1st**	**1.013**	**0.67**	**0.8**	**2**
# 7	2nd	2.69	0.67	4	0.2

Figure 3.9: *Summary of important parameters to describe transducers displacement and force sensitivity. The displacement sensitivity has been calibrated using the equipartition theorem.*

3.3.1 Displacement Sensitivity α

A key parameter for mechanical probe's integrated readout, is the displacement sensitivity (α) [102]. Which is related to the force sensitivity by:

$$\sqrt{S_{FFtip}^{peak}} = \alpha k_{tip} \tag{3.13}$$

with k_{tip} the spring constant of the desired mode at the cantilever tip.

The displacement and force sensitivity, summarized for each probe in Table 3.9, was estimated via the equipartition theorem. The raw voltage signals, proportional to the vertical displacement of the probes, were calibrated by fitting the measured voltage power spectral density with a Lorentzian $S_{ZZ}(\omega)$ with an area given by the equipartition theorem [100, 103] (Figure 3.3).

Form this procedure, we obtained the transduction gain β in $V \cdot m^{-1}$ and the displacement sensitivities (α) reported in Table 3.9. The statistical uncertainty derived from the measurement is small. The main uncertainty is propagated from the Young's modulus used to calculate the spring constant for the displacement sensitivity calculation with the equipartition theorem. The estimated variation of the Young's modulus originating from deposition conditions is about 10 %.

The displacement sensitivity at the disk and the cantilever tip is reported individually, the difference originates form the different spring constants. Therefore, the displacement sensitivity at the probe tip can easily be tailored for specific application, e.g. high sensitivity or wide dynamic measurement range.

3.3.1.1 Standard Quantum Limit

Due to the quantum nature of light, measurements of the motion of a mechanical oscillator as described in this thesis are fundamentally limited in sensitivity. In general, the uncertainty principle poses a limit on how well one can continuously measure a certain quantity. This limit defined by the standard quantum limit (SQL) [104–106]:

$$\sqrt{S_{xx}^{SQL}} = \sqrt{\frac{\hbar Q_m}{k}} \qquad [\frac{m}{\sqrt{Hz}}] \tag{3.14}$$

with $\hbar$ the Planck constant. Following:

$$\sqrt{S_{FF}^{SQL}} = \sqrt{S_{xx}^{SQL} * (\frac{k}{Q_m})^2} = \sqrt{\frac{\hbar Q_m}{k} * \frac{k}{Q_m}} \qquad [\frac{N}{\sqrt{Hz}}] \qquad (3.15)$$

for the force sensitivity.

The semi-classical definition of the SQL is the condition where the optical shot noise measurement uncertainty is equal to the uncertainty due to random backaction force of the photons on the device, such that the combined uncertainty is minimized. It should be noted that at room temperature the force measurement is limited by the thermal, Langevin force noise, which is $\frac{kT}{\hbar\Omega} >> 1$ larger than the force measurement SQL.

The reported devices are too big to reach the SQL limit. In these devices the thermal nois is by far dominat for the reported mechanical resonance frequences. However, we showed in [107] and [108] that displacement sensitivities close to the SQL can be reached with relatively small modifications on the design.

3.3.2 Readout Tuning

For some designs, the integrated actuator allows the active tuning of the readout gain, by applying a static bias voltage to the actuator [109]. To show the ability of readout tuning, the dynamic response of the structure with different bias voltages was measured, normalized in generated force. A small fixed modulation (AC) voltage, with a frequency sweep of $\approx$ 200 kHz around the resonators resonance frequency, was added to the actuator static bias (DC) voltage, resulting in a small, known mechanical modulation of the gap. The laser wavelength has been fixed at the steepest point of the slope in transmission on the side of the optical resonance line at each applied DC voltage. After every DC voltage change, the position on the slope was adjusted since the resonance frequency changes due to a change of the mechanical member position. A network analyzer was used to provide the AC voltage and detect the resulting optical power modulation which is proportional to the motion amplitude and optomechanical coupling. A typical optomechanically measured normalized device transfer function is illustarted in Figure 3.10 (inset).

The AC bimorph output is proportional to the product of AC and DC volt-

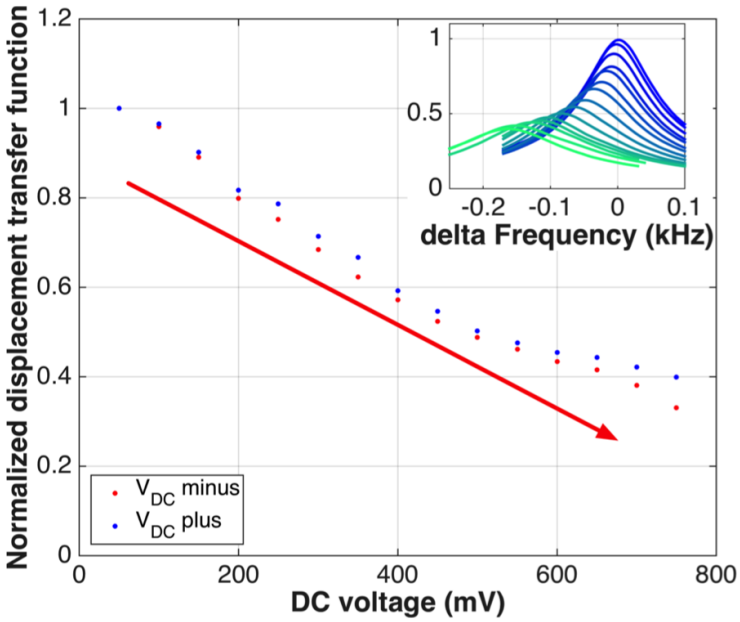

Figure 3.10: *Normalized readout gain of the optomechanical displacement sensor, of the Design 3, is decreased by static actuation. The one standard deviation uncertainty based on fitting network analyzer spectrum data is smaller than the data marker size. Inset: Corresponding normalized transfer function of the transducer for the same excitation force amplitude with different DC offsets. The DC voltage actuates the moving probe away from the microdisk, reducing the readout gain.*

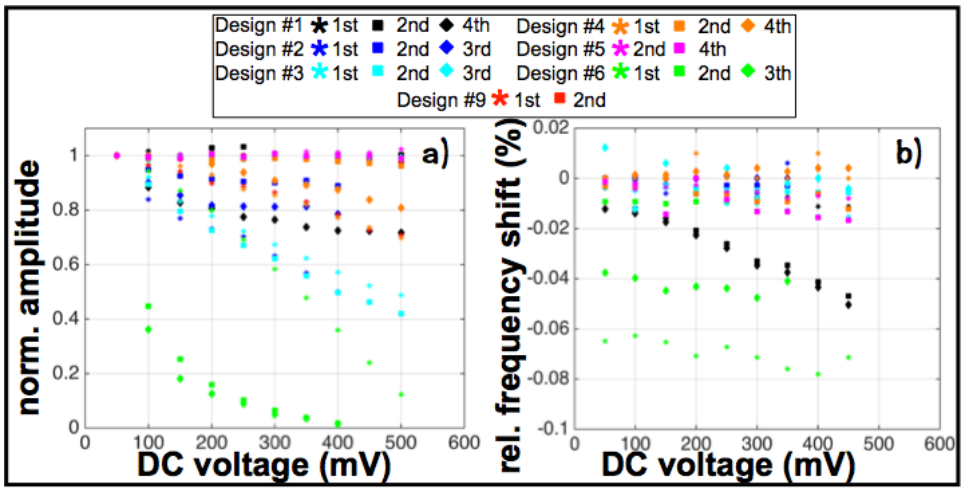

Figure 3.11: *(a) Normalized oscillation amplitude as a function of applied DC voltage. For some designs, especially design # 6, readout tuning is clearly visible. (b) Shows the relative frequency shift between two adjacent transfer functions in %, it can be see that the resonance frequency of some probes is changing due to an increase in applied DC voltage. This can be caused by e.g. thermal heating of the probe. However, some probes show no, or a negligible influence of the DC voltage on the mechanical resonance frequency.*

ages as the actuation force is quadratic in applied voltage. To illustrate the tuning of the optomechanical gain by the actuator, the displacement spectra was first normalized by the DC voltage to account for the stronger drive with larger DC voltage. The resulting normalized displacement transfer function (Figure 3.10) reveals the gain decreasing with increasing bias as the actuator increases the transducer gap and decreases the readout gain of the optomechanical sensor. The results show that the small actuation here is capable of tuning the gain by more than $\approx$ 70 %, for a probe of design # 3.

The probe response on a DC voltage change, supplied to the integrated actuation, depends strongly on the probe design. Some designs, e.g. design # 3 in the 1^{st}-, 2^{nd}- and 3^{th}- mode, show a linear dependency of the readout gain on the supplied DC voltage. In contrast, design # 5 doesn't show any influence of the DC voltage on the readout gain, as shown in Figure 3.11. For this design, the DC offset can be used to adjust the z-position of the cantilever tip, without changing the optical readout. Figure 3.11 (a) shows

that the integrated actuation is able to tune the readout gain on design # 6 by up to 90 %. In general, each mode results in a combination of tilt and z motion of the probe relative to the micodisk, and DC actaution adjusts also both the tilt and the z distance. When the DC actuation tilt is 0, the readout is not sensing the AC tilt, while when DC tilt is significant, the readout becomes sensitive to AC tilt. Therefore, the tuning behavior can be different for different modes.

3.3.3 Frequency Stability

The frequency stability of a probe is another important parameter. In many cases, the detection of physical quantities is based on the detection of a change in the mechanical resonance frequency of a probe, i.e. dynamic atomic force microscopy, resonant accelerometer, and artificial noses. For the reproducible high sensitivity measurement, the stability of the resonance frequency is essential.

Some of the designs studied in this article show strong linear dependency of the resonance frequency on the supplied DC voltage, e.g. design # 1 2^{nd}-, and 4^{th}- mode. This negative shift in frequency can be explained by e.g. thermal heating of the probe causing a softening of the material. Other probe designs, e.g. design # 3, show a higher frequency stability in the presents of a change in DC actuation voltage. This implies that either the thermal drain in much higher compared to the other designs, or the impact of a change in temperature is not as significant on the modal stiffness.

3.3.4 Optical Excitation of the Mechanical Motion

Increasing the optical power coupled into the cavity causes several notable changes in the rf spectrum of some probes, as seen in Figure 3.12 for a device with the design # 6 (Figure 3.8), where the coupled power is changed by fixing the waveguide input power to $\approx$ 5 µW, $\approx$ 1.1 µW at the sensor, and varying the detuning $\Delta\lambda$ between the laser and cavity mode. First, the spectral position of the first mode resonance changes from $f_r \approx 119.35$ kHz at low $\Delta\lambda$ to $f_r \approx 119.33$ kHz at $\Delta\lambda \approx 100$pm before returning to close to its original value at $\Delta\lambda \approx 170$pm. This experiment was performed at a pressure of 5 mPa.

Along with the change in frequency, the amplitude of the first harmonic increases significantly and satellite peaks of the harmonics appear in the spectrum which can be an indicator for self-sustained oscillations of the first two mechanical modes. Inset (c) shows the Allan deviation as a function of integration time for the first mechanical mode at the detuning ≈ -120 pm, black dashed line. The dashed lines represent the thermodynamic limit ($\frac{x_{rms}}{\sqrt{x_{rms\ thermal}}}$) for the measured oscillation amplitude and the mechanical Q (relaxation time) measured at small optical power. The vertical red line represents mechanical energy relaxation time constant t_1 of this cantilever probe. The observed regenerative self-oscillation is most likely excited thermo-optically, aided by the facile thermal actuation of the device. The high frequency stability of the first mechanical mode regenerative oscillation over time can be practically useful for frequency-modulated sensing, such as the FM-AFM mode.

3.4 Conclusion

Development of the design for a fully-integrated cavity optomechanical transducer platform for measurement of physical quantities by transducing them to mechanical motion was summarized. Overhanging mechanical probes with different actuation schemes, geometries, and anchor condition were presented. The transducer behavior was analyzed in terms of displacement sensitivity, readout tuning and frequency stability. The probes are between 25 µm and 60 µm long and cover a frequency range between 100 kHz and 1 MHz for the first harmonic with a spring constant between 0.03 $\frac{N}{m}$ and 100 $\frac{N}{m}$. Displacement sensitivities as low as ≈ 0.14 $\frac{fm}{\sqrt{Hz}}$ have been shown. The integrated electrical actuation can also be used to tune the readout gain of some designs by up to 95 %, which allows us to trade a decrease in displacement sensitivity against an increase in the dynamic measurement range.

The influence of the supplied electrical actuation power on the probe behavior depends strongly on the probe geometry, some show no, or only a negligible influence, others show a significant shift of the probes resonance frequency.

In addition, membranes with four different sizes and integrated electrostatic actuation, to cover the resonance frequency range from a few tens of kilohertz up to a few megahertz, was fabricated.

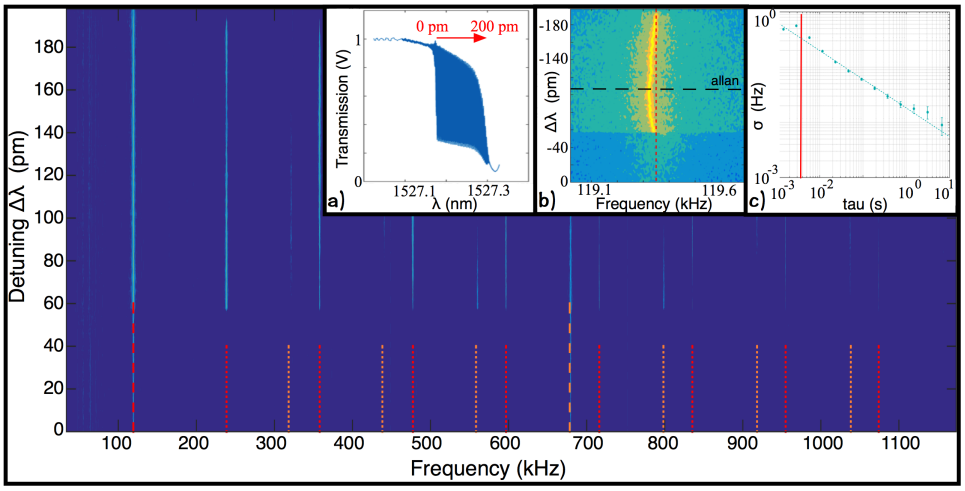

Figure 3.12: *Image plot of the rf spectra as a function of $\Delta\lambda$. The cavity mode used for transduction is shown in inset (a). The first and second mechanical mode are marked with the red and orange dashed line respectively. The thin dashed lines make equally spaced satellite peaks of the respective harmonic. The inset (b) shows a zoomed in view of the first mechanical mode. It shows a shift to lower frequencies at the maximum excitation. Inset (c) shows the Allan deviation as a function of integration time for the first mechanical mode. The dashed lines represent the thermodynamic limit for the measured excitation amplitudes. The curve has been normalized in respect to the input power. The vertical red line represents time constant t_1 of the cantilever probe.*

4.0 Scanning Probe Microscopy

A potential application of these optomechanical transducers with integrated actuation is scanning probe microscopy (SPM) [18, 110–113]. The integration of readout and actuation minimizes the needed external setup and therefore reduces the setup size dramatically. Furthermore, a full integration can improve the usability and can reduce the barrier for inexperience users to use this microscopy technique [114–117].

The improvement in usability is mainly achieved due to the plug-and-play approach for these scanning probes. The user doesn't have to align any external optics or has to setup electronics. For a measurement, the user only has to place the probe chip in the cantilever holder, everything else can be automated. The improvement in the probe handling and force sensitivity have the potential to drive SPM techniques into new applications [118] like clinical analysis, quality inspection in manufacturing, security industry for identification of unique nanostructures, etc.

4.1 SPM Setup

The SPM setup used for the experiments described in section 4.2 and section 4.3 is presented in the following. First, the probe chip integration into the commercial SPM will be described. Only minor modifications have been made to insure the compatibility.

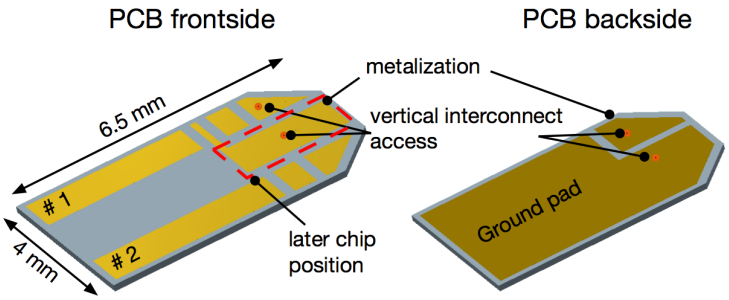

Figure 4.1: *PCB for the electrical and mechanical packaging of the silicon probe chip. The PCB is ≈ 400 µm thick and has a structured ≈ 17 µm thick Au coating on both sides, for contact pads and ground pad. The front- and backside coating is connected with two vertical interconnections. The vertical interconnection in the center is used to connect the cantilever chip to the ground pad on the backside (orange dots). The label # 1 and # 2 highlight the two pads, which are contacted by the copper spring of the cantilever holder, described in the next subsection, to create a mechanical and electrical contact between the PCB and the cantilever holder. The red dashed line marks the area of the later probe chip position.*

4.1.1 Chip Packaging

The packaging of the silicon chip can generally be separated into three areas; packaging for the optical, mechanical, and electrical parts.

1550 nm single mode optical fibers were used to fiber pigtail the chip. The fibers are actively aligned to the chip and hold in place with UV curable epoxy. The optical fibers are spliced to fiber optical patch cables (SMF28E) with FC/APC connectors, for the integration in the optical setup.

For the electrical connection of the probe chip to the electronics of the SPM, a print circuit board (PCB) shown in Figure 4.1 was designed. The chip is wire bonded to the ≈ 17 µm gold plated contact pads on the PCB. The mechanical and electrical ground connection to the chip was achieved with silver epoxy between the chip and the PCB. This also guarantees a sufficient thermal connection of the chip to the setup to minimize thermal drifts in the transducer setup.

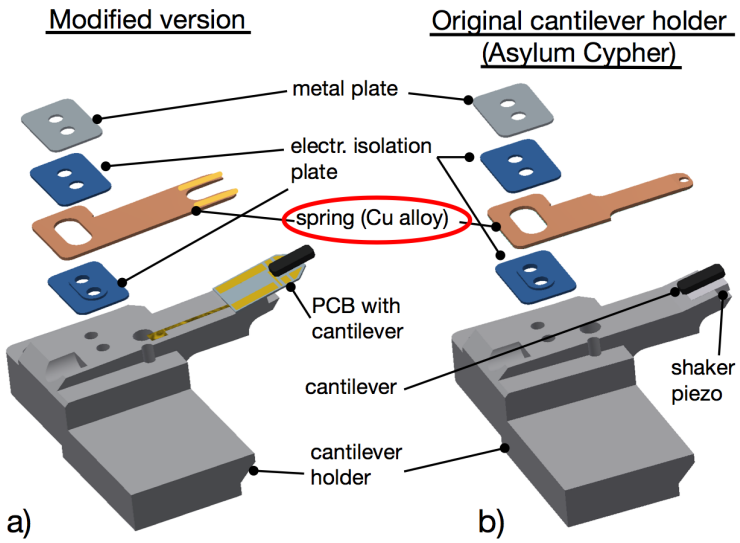

Figure 4.2: *(a) The modified cantilever holder for the SPM. (b) Original cantilever holder of the "Asylum Cypher". The red circle highlights the only element, changed on the cantilever holder, to adjust the cantilever holder for the PCB and probe chip presented earlier.*

4.1.2 Modifications on the Cantilever Holder

All SPM experiments presented in this thesis have been performed with the "Asylum Cypher Scanning Probe Microscope". For the compatibility of the probe chip on top of the PCB with the cantilever holder of the "Asylum Cypher", the copper spring of the cantilever holder has been modified. The spring shape, in the tip area, was changed, to create more space for the Si chip and to shape two "finger contacts", shown in Figure 4.2.

The metal surface of the spring was coated with resist for electrical insulation. On top of the insulation, two contacts out of copper foil have been formed and connected to copper wires (Appendix A.2). The copper wires were connected to the integrated PCB of the cantilever holder for the electrical connection to the SPM electronics. The spring presses on the Au contacts of the probe PCB to provide a reliable and easy way to connect the integrated actuator of the probes to the SPM electronics, shown in Figure 4.3.

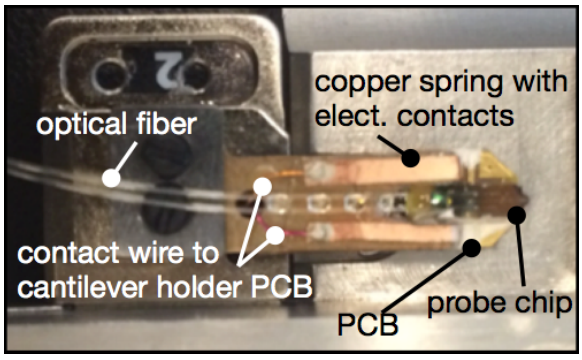

Figure 4.3: *Cantilever chip, mounted on the PCB, placed in the modified cantilever holder of the SPM. The electrical wires connected to the modified copper spring are shown, as well as the optical fibers securely attached to the cantilever chip.*

4.1.3 Setup SPM Measurement

With the modified cantilever holder, the developed probes can be easily installed in the SPM. The cantilever holder with probe, installed in the SPM, is illustrated in Figure 4.4. This SPM setup can be used for single probes as well as for probe arrays, which will be shown in the following sections.

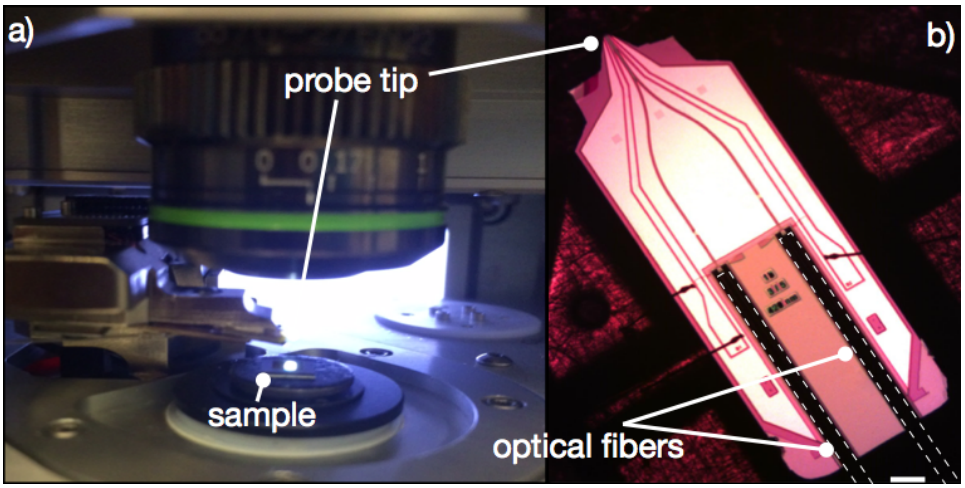

Figure 4.4: *(a) Optomechanical cantilever probe installed in the SPM. (b) Probe chip mounted on the PCB, with attached bone wires and optical fibers for the electrical and optical connection of the chip. The dashed white lines highlight the positions of the optical fibers in the v-grooves. Scale bar corresponds to 300 µm.*

4.2 SPM Experiment

The higher readout sensitivity of these probes, compared to conventional optical beam deflection (OBD) readout, would in principle allow a higher scan speed then shown here. Within the framework of this thesis it was not possible to show high speed SPM imaging, due to the limitations of the used commercial microscope used in our experiment.

For this experiment the same setup as described in section 3.2 was used. Light from a tunable laser (1520 nm to 1630 nm) is sent through a polarization controller and coupled into the fiber pigtailed device. The output of the fiber is analyzed with a photodetector and the built-in lock-in amplifier of the SPM.

Figure 4.5 illustrates the measured thermal mechanical noise spectral density of one cantilever, the SEM of the released probe is shown in the inset, in vacuum (≈ 1 mPa). A clear peak in the noise spectrum occurs at ≈ 123.6 kHz, in good agreement with a finite- element model with a silicon nitride with tensile stress of about ≈ 150 MPa. A mechanical quality factor of better than 1200 is evident from the data. A TM optical mode with an optical quality factor of ≈ 100 000 was used to carry out this measurement at an

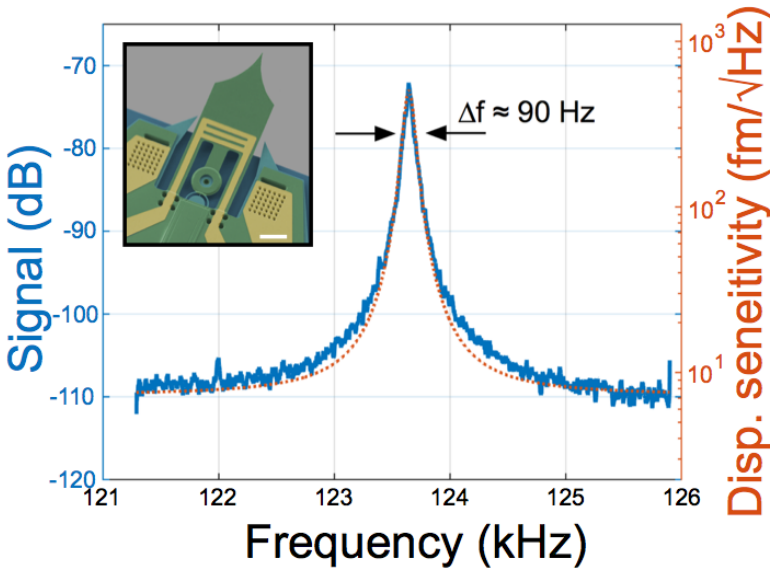

Figure 4.5: *Measured mechanical frequency noise spectrum of a cantilever transducer with Lorentzian fit. Signal power is reported relative to 1 mW. The inset show false-color SEM of the released probe, corresponding to the measurement.*

input excitation optical power level of approximately 9.16 µW (-20.4 dBm), resulting in ≈ 2.7 µW (-25.6 dBm) at the sensor and ≈ 820 nW (-30.9 dBm) at the photodetector, accounting for an estimated ≈ 5.3 dB fiber pigtail coupling losses at each facet. The signal to noise ratio on-resonance is approximately 38 dB.

For the experiment, the laser was locked on the shoulder of the optical resonance peak. The integrated actuator was supplied with a DC signal of ≈ 20 mV and an AC amplitude of ≈ 5 mV, which generates an oscillation amplitude of ≈ 0.8 nm. The photodiode signal was analyzed with the integrated Lock-in amplifier of the SPM to detect the amplitude of the mechanical oscillation.

For the approach of the cantilever probe to the sample surface, the amplitude signals was supplied to the integrated PID controller and used the SPM software for the approach. For imaging, the cantilever was supplied with a constant excitation frequency, which was close to the mechanical resonance frequency of the individual cantilever. The frequency

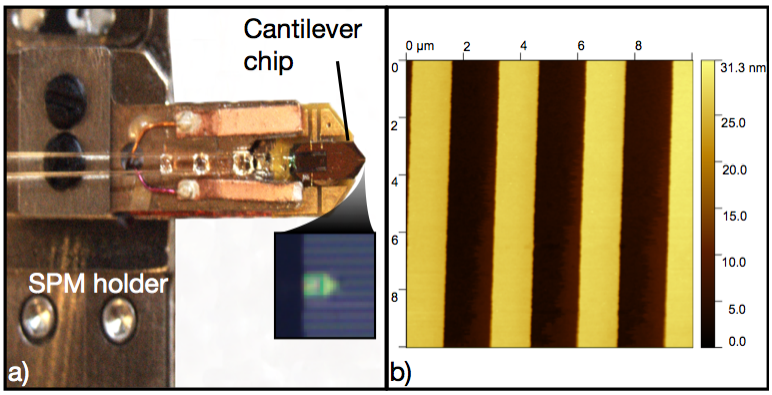

Figure 4.6: *(a) Cantilever chip in the modified SPM holder. The inset illustrates the cantilever chip in close proximity to the sample surface. This images has been taken with the build in camera of the commercial SPM. (b) Shows a 512 x 512 pixel SPM image acquired with a scan speed of 0.5 Hz. The image shows a ≈ 10 x 10 µm sector of a calibration sample.*

was fixed and the change in oscillation amplitude was used as feedback signal. For z-movement, the stage piezo was used, the probe's DC offset voltage was fixed throughout the experiment.The resonance frequency of the cantilever was ≈ 123.6 kHz with a corresponding stiffness of ≈ 22 N/m. Figure 4.6 (b) presents the acquired scanning probe micrograph. The image shows a ≈ 10 x 10 µm sector of a calibration sample, with a resolution of 512 x 512 pixel acquired with a scan speed of 0.5 Hz.

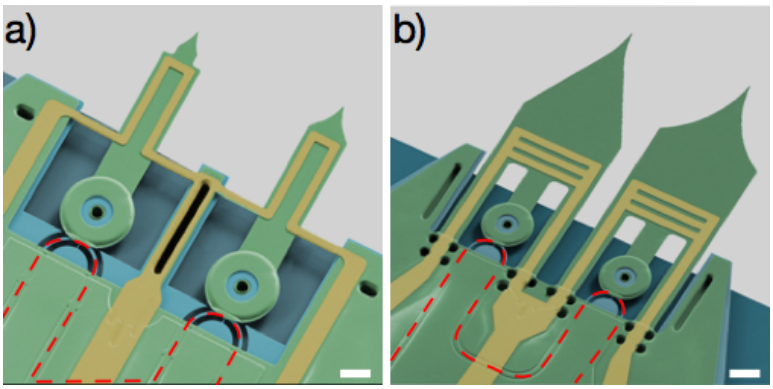

Figure 4.7: *False-color scanning electron micrographs of the released probe arrays, to illustrate the different designs, showing the structural layer (green), metal layer (yellow), silicon device layer (light blue), and silicon handle wafer (dark blue). (a) Probe array with torsional support and with individually addressable bimorph actuation (Array design A). (b) Cantilever probe array with rectangular shape and integrated bimorph actuator (Array designB). The dashed red line highlights the waveguide path, connecting both microdisks in series. Scale bars correspond to 5 µm.*

4.3 SPM Array Experiment

The modular design of the described probe concept allows for parallelization of multiple probes, as shown in Figure 4.7. Here, the use of probe arrays for parallelized SPM [119, 120] is highlighted.

One critical parameter of any SPM is the imaging speed. A reduction of the time needed to acquire a single image would broaden the field of possible applications [121–124]. For this experiment, the SPM with the modification cantilever holder and the optical setup described previously was used, (section 3.2 also shown in Figure 4.8). The physical design of the array has been modified to arrange the cantilever probes in series. The waveguide is first evanescently coupled to one of the microdisks and then to the second microdisk (Figure 4.7). For the actuation, three electrical contact pads were used. The central pad is grounded and channel I and channel II are used to drive cantilever I or II respectively (Figure 4.8).

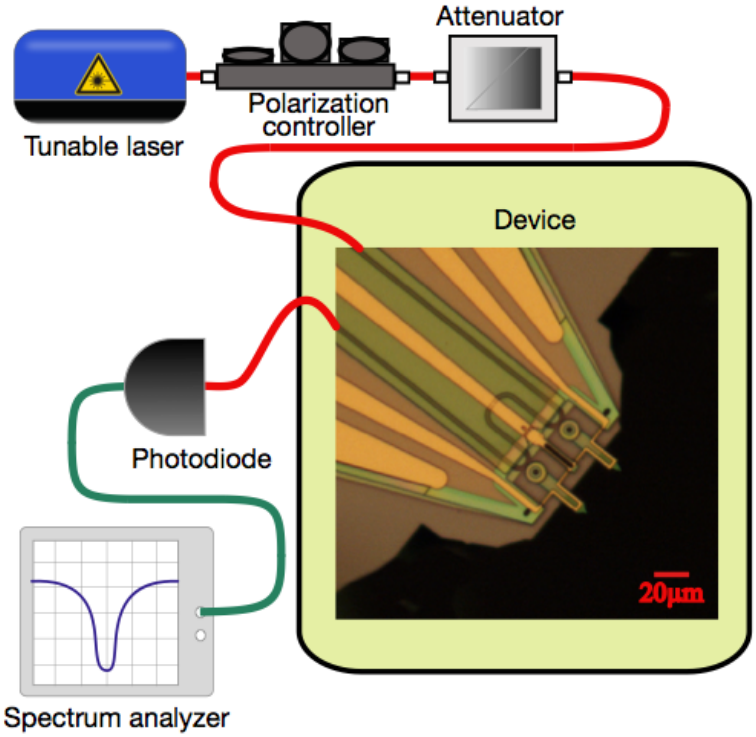

Figure 4.8: *Schematic of the detection setup with an embedded optical micrograph of a cantilever array (Design A) with torsional support (scale bar is 20 µm). Red lines indicate optical fibers for the transducer readout. Blue lines indicate electrical connection to individually address the cantilevers.*

4.3.1 Linear and Nonlinear Operation

For the simultaneous readout of multiple microdisks with one tunable lasers source, the optical microdisks were operated in the non-linear regime.

The non-linear response of the microdisk was first studied by measuring the dependence of the transmission signal line shape on the power input to the fiber pigtailed probe chip. Figure 4.9 illustrates wavelength scans of the cavity transmission for varying power input to the fiber pigtailed chip. This experiment was performed on a transducer chip with one microsdisk, to make this behavior clearly visible. Array transducer behave in a similar way, as can be seen in Figure 4.10.

Increasing the power at the chip input, and consequently the microdisk, results in two readily observable changes in transmission: (i) a shift $\Delta\lambda$ in the resonance frequency, and (ii) broadening and asymmetric distortion of the resonance line shape, eventually leading to a "snap" in the reflection response characteristic of bistability [125–127]. The small SiN pedestal (r ≈ 1.3 µm and l ≈ 2.5 µm) in the R ≈ 5 µm microdisk presented here, provides relatively poor thermal conduction as compared to the radii disks. As a result, thermally induced changes of the refractive index cause a red shift of the resonance wavelength (Figure 4.9), also known as the thermo-optic effect [128]. In case of a typical resonator, this effect increases with increasing optical power in the microdisk mode. Form Figure 4.9 it is evident, that this effect can create significant shifts of the optical resonance. An increase of the optical power by a factor of ≈ 63/$times$ can shift the optical resonance frequency by up to 950 pm.

The optical resonance wavelength position for every microdisk is slightly different due to e.g. small deviations in the disk geometry, contamination on the disk surface, or different pre-deflections of the mechanical member cause slightly different effective refractive indices.

The offset between optical modes of the same family is typically smaller then 1 nm. Therefore, it is in general possible to superimpose optical modes of different cavities with the mode shift cause by thermal heating.

Figure 4.10 shows the optical transmission spectrum of the device at low (blue) and high (orange) optical power. For low laser powers (≈ 0.8 µW at the sensor), the transmission through the coupled microdisk array displays two separate single dips, characteristic for one traveling wave in each microdisk. At slightly higher input powers (≈ 5 µW at the sensor coupling

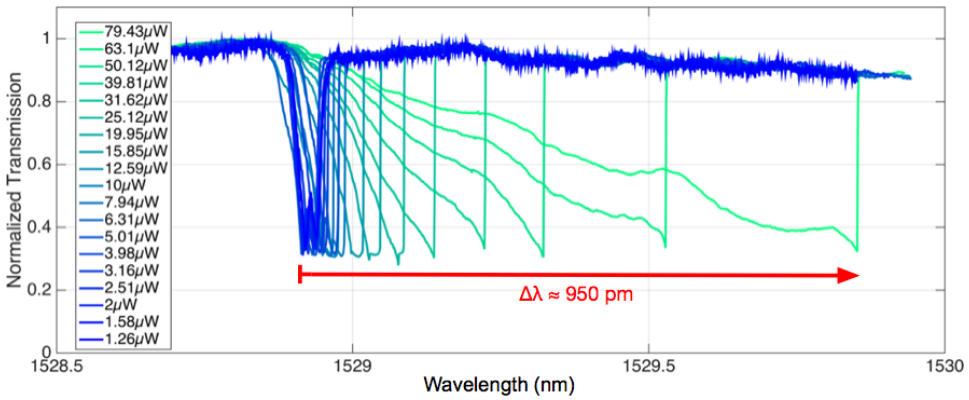

Figure 4.9: *Transmission signal of the probe as a function of input power. Starting with the linear response of the $TM_{2,30}$, of a microdisk, at an input power of ≈ 1.26 μW until the highly non-linear response at an input power of ≈ 79.43 μW. It is evident that a change in optical power by a factor of ≈ 63× can shift the optical resonance frequency by up to 950 pm for this microdisk.*

point) a distorted asymmetric line shape with sharp recovery was observed. The green area highlights the superimposing region of the two optical modes.

For the readout of multiple optical microdisks with one fixed laser wavelength, the laser is first tuned to the blue side of both of the low-power resonance dips. Then, using a high laser power, the laser is slowly red shifted, tracing the orange trace in Figure 4.10, until the nonlinear optical spectrum of the first disk overlays with the linear optical spectrum of the second disk Figure 4.10 (green area).

In this region, the light is coupling into both microdisks. This allows the imprint of the mechanically induced transmission modulation of both microdisks on the transmitted light signal. The light carrying the information of both microdisks is then analyzed with a photodetector and a network analyzer to reveal the ratio of the optical modulation to the driving force with the force applied to each cantilever individually (Figure 4.11).

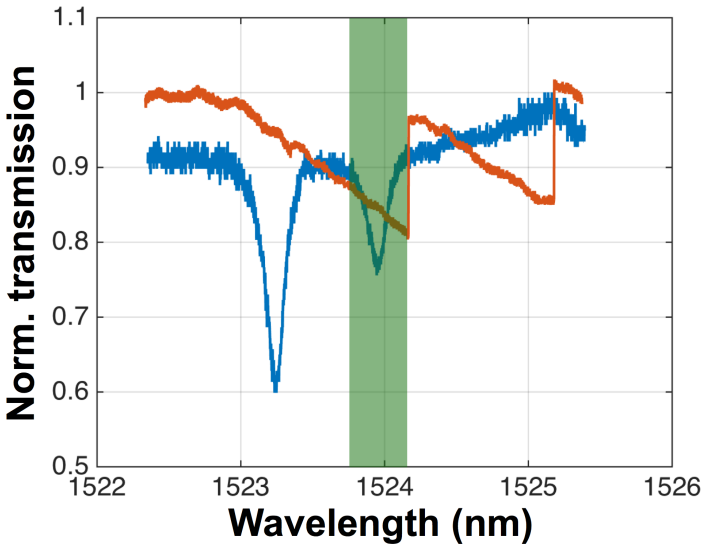

Figure 4.10: *Optical transmission spectrum of the device at low (blue) and high (orange) optical power. The triangular shape, in the high power optical spectrum, is an indication that the optical disk is driven nonlinear. The optical resonances move to higher wavelength, because of a change in the resonance conditions of the disk. This change is mainly induced by a temperature change of the disk and the connected change of the refractive index of silicon. The green area marks the range, where the nonlinear resonance of the first disk overlaps with the linear resonance of the second disk. A laser wavelength in this range will couple into both micordisks. If the light is coupled into both disks, the mechanically induced transmission modulation of both microdisks will be imprinted on the transmitted light.*

4.3.2 Parallel Imaging

For imaging with both cantilevers, the optical microdisks are superimposed as described before. The light carrying the information of both cantilever probes is then analyzed with a photodetector and network analyzer to reveal the ratio of the optical modulation to the driving force applied to both probes individually (Figure 4.11).

In the following, the laser of the SPM OBD system was focused on the backside of one cantilever. The OBD read-out was used for an automated approach of the cantilever and to record a reference image. The image recorded with the cantilever array and the OBD is shown in Figure 4.12 (b), the sample was a test grating with ≈ 2 µm wide and ≈ 40 nm high lines. The image shows a ≈ 8 µm by 8 µm scan with 256 x 256 pixel acquired with a scan line rate of 0.5 Hz.

After the acquisition of a reference image, the deflection input channel of the microscope was switched to the deflection signal provided by the integrated optomechanical readout of the cantilever array. For the experiment, the array shown in Figure 4.7 (b) was used.

The tunable laser was locked as described before, in a position which allows us the readout of both optical cavities simultaneously. The integrated actuators are supplied with a DC signal of ≈ 20 mV and an AC amplitude of ≈ 5 mV, which generates an oscillation amplitude of ≈ 0.8 nm. The photodiode signal was analyzed with two Lock-in amplifiers, to detect the amplitude of each mechanical oscillation.

For the approach of the array, the amplitude signals was supplied to the integrated PID controllers. After sensing the surface with the first cantilever, DC offset voltage on the other cantilever was increased, until the surface was reached with both cantilevers. For imaging, a DC offset of ≈ 20 mV and AC signal of ≈ 5 mV for the right cantilever and a DC offset of ≈ 45 mV and AC signal of ≈ 3 mV for the left cantilever was used. The applied DC offset for the left cantilever creates a reduction of ≈ 15 % in the readout gain of the corresponding cantilever.

Both cantilever have been supplied with constant excitation frequencies, which were close to the mechanical resonance frequencies of the individual cantilever. The frequencies were fixed and the changes in oscillation amplitudes were used as feedback signals for each cantilever independently. The PDI feedbacks were controlling the height of each cantilever by driving

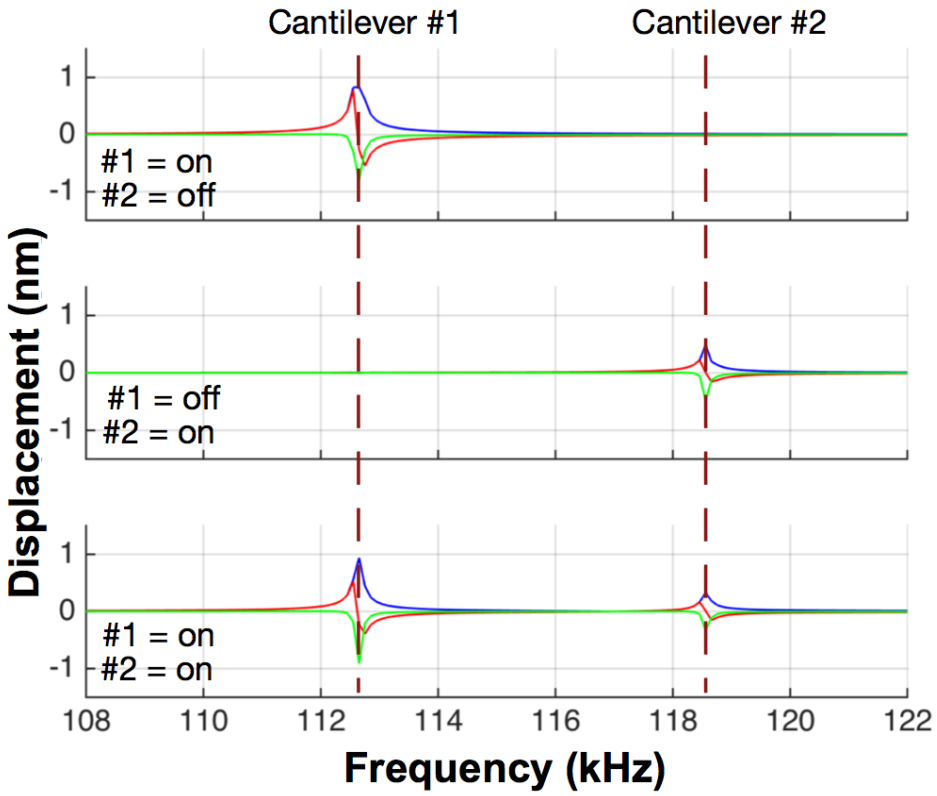

Figure 4.11: *Transfer function of the cantilever array, recorded with a single fixed laser wavelength. The dashed red lines indicate the resonance frequency of the two cantilevers. The three graphs demonstrate independent actuation of the cantilevers. (top) Transfer function with the actuation turned "on" for cantilever #1 and "off" for cantilever #2. (middle) Actuation "off" for cantilever #1 and "on" for cantilever #2. (bottom) Actuation "on" for cantilever #1 and "on" for cantilever #2. The blue trace is the amplitude (R), red is the x-signal from the network analyzer and green is the y-signal of the network analyzer.*

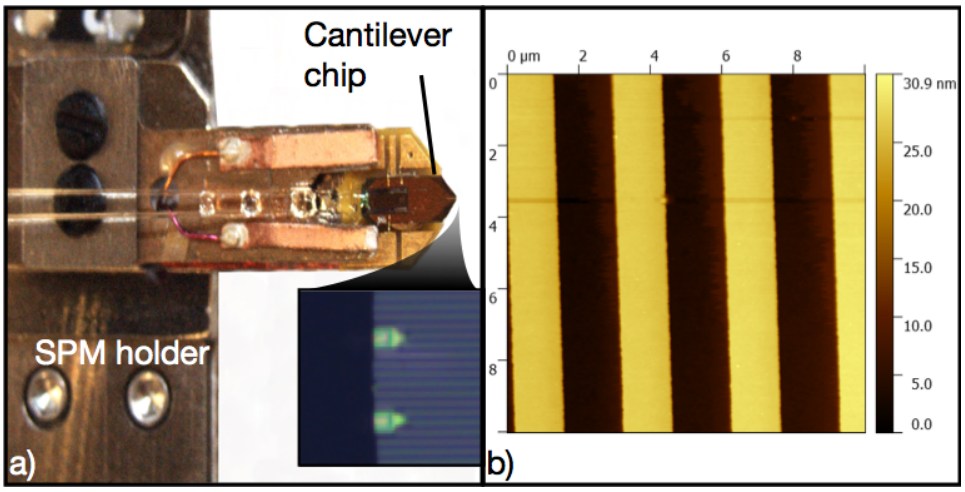

Figure 4.12: *(a) Cantilever array chip in the modified SPM holder. The inset shows the cantilever array in close proximity to the sample surface. This image has been taken with the build in camera of the commercial SPM. (b) Shows a SPM reference image taken with one probe of the array using the OBD readout.*

the DC offset voltages. The resonance frequencies of the cantilevers were ≈ 112.5 kHz (left) and ≈ 118.3 kHz (right) cantilever with a corresponding stiffness between ≈ 0.1 N/m - 5 N/m, also shown in Figure 4.11. SPM stage z position was kept constant and DC offset voltage were used to move the cantilevers in z independently, tracking the grating surface under PID feedback control. Figure 4.13 (a) and (b) show the recorded images for the left and the right cantilever respectively. The insets show a 3D representation of the micrographs. The recorded micrographs show that the integrated optical readout can acquire micrographs in a quality comparable to the OBD, but on an array level.

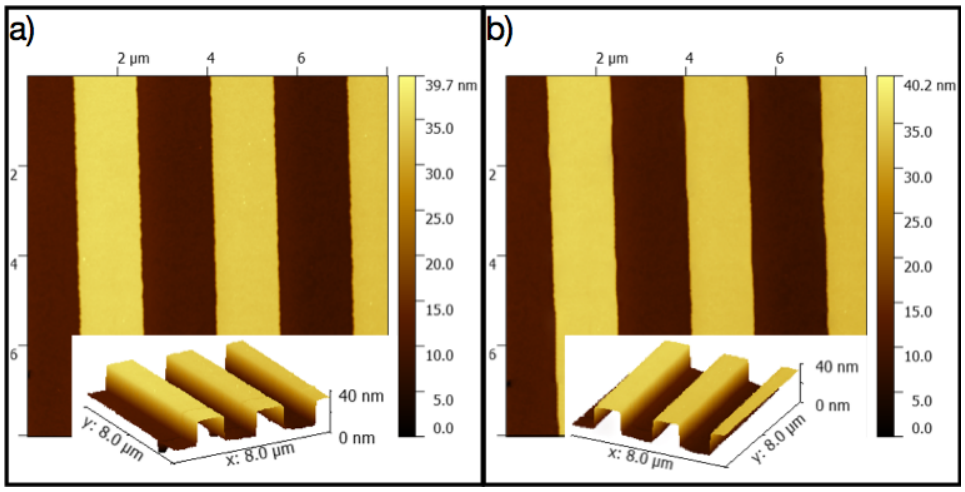

Figure 4.13: *Scanning probe micrographs acquired with the cantilever array. (a) Image acquired with the left cantilever. The image shown in (b) has been acquired with the right cantilever. The insets show 3D topographical views generated based on the measured data.*

4.4 Conclusion

This chapter presented the modification of a "Asylum Cypher" SPM to allow the operation of the probes developed in the scope of this graduate work. A first scanning probe image has been shown.

In addition, the parallelization of the probes and the simultaneous optical readout of multiple optomechanical probes with a single tunable laser at a fixed wavelength was demonstrated. The advantage of this technique is a significant reduction in the readout setup complexity and cost, as well as the simplification of on-chip photonic structures. Two SPM images acquired with the integrated optical readout were presented, showing that the images acquired are comparable to those taken with the conventional SPM OBD readout.

5.0 Optical Inspection Probe

The automated non-destructive electrical testing of devices during the fabrication greatly increases the yield through statistical process control and reduces costs by selecting “known good die" for further processing and packaging, essential for microelectronic manufacturing.

Similar testing is desirable for integrated photonic devices in research and manufacturing. Traditional optical coupling methods, including fiber-end coupling [98] and prism-based coupling [129] require packaging before testing. Incorporating fixed grating couplers for chip and wafer-scale non-destructive testing consumes precious circuit area and provides only fixed levels of optical coupling at pre-specified locations.

A probe achieving variable, controlled and directional coupling of light immediately into and out of unmodified waveguides or photonic devices is desired. One option popular in a research setting is a fiber-taper probe: a single mode fiber is locally stretched, creating a waist of a few hundred nanometer in diameter, and enabling evanescent coupling [130].

While this approach shows excellent low optical loss, high bandwidth and fine polarization control, the resulting thin fiber section is soft and subject to low frequency mechanical noise. In turn, this complicates control over the coupling depth. Shaping such a probe to access specific locations on a dense photonic circuit with sizeable surface topography is difficult, requires artisanal fabrication techniques, and the resulting bend radius is still large [131].

The small and stiff microfabricated optical probe presented here is

immune to low frequency mechanical vibration. The probe is fabricated at the end of a micromechanical cantilever and used in a commercial SPM system to control the probe-sample separation and the evanescent coupling rate. Furthermore, the Si probe's effective index can be set by choosing the waveguide width, and a high effective index allows deep coupling to otherwise inaccessible modes in non-undercut Si and SiN cavities and waveguides without incurring optical losses into their cladding layers.

5.1 Probe Design

The probe design is based on the same fabrication process presented in chapter 2. Figure 5.1 shows the released probe at the end of the fabrication process. The microfabricated waveguide loop is out of high refractive index Si for simpler matching to Si photonic devices.

Alternatively, a SiN photonic layer may be used for applications in the visible. The nominally 500 nm wide on-chip waveguide is tapered down to a minimum width of ≈ 300 nm where it forms a half-circle loop, extending the evanescent field into the surrounding air (Figure 5.1 (b)).

A SiN cantilever structure is used to mechanically support the extending Si waveguide loop. A pattern of deep "anchor" groves is dry-etched through the SiO_2 and SOI before conformal SiN deposition. These anchors attach the nitride and SOI structures to the substrate and to each other for mechanical rigidity.

5.2 Experiment

The probe functionality is demonstrated by using it to conduct swept-wavelength optical spectroscopy on a Si microdisk high Q optical cavity. The optical probe is mounted in the modified cantilever holder of the SPM described in section 4.1 (Figure 5.2 (a)).

The laser of the SPM beam deflection detection system is focused on the SiN cantilever structure (Figure 5.2 (b)).

To set the optical probe height relative to the device under test, a force curve was recorded by moving the probe toward the sample and recording the SPM beam deflection signal (Figure 5.1 (c)).

The force curve is a plot of the cantilever deflection versus the extension of the piezoelectric scanner in z, measured using a position sensitive

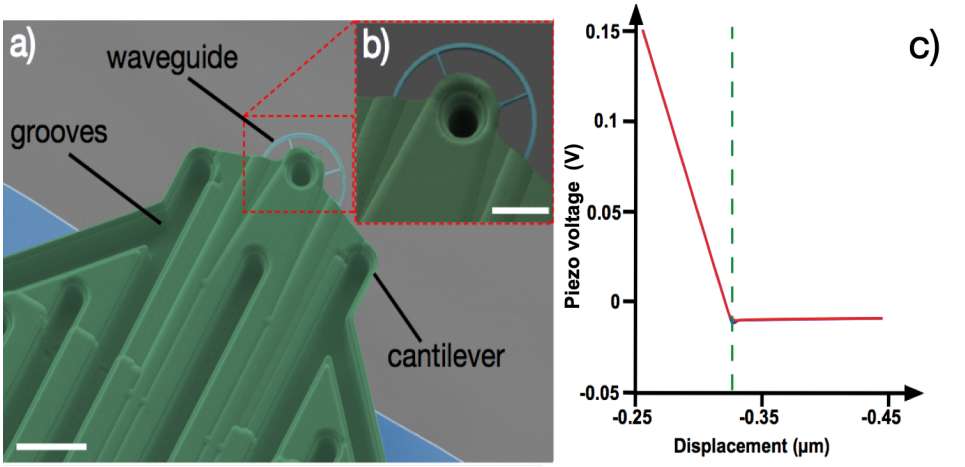

Figure 5.1: *(a) False-color scanning electron micrograph of the release optical probe with light blue and green representing Si and SiN, respectively. Si waveguide loop is supported by additional tethers and attached to the cantilever, which is formed by a combination of SiN and SOI layers. Grooves visible in the SiN structures increase structural rigidity of the cantilever and attach it to the Si substrate (light blue on the left and right of the cantilever). Scale bars are (a) 10 μm and (b) 5 μm. (c) Force curve of the cantilever, used to detect the probe-sample physical contact point. The calibrated Z-piezo of the SPM is then used to make the measurement at the desired probe-sample separation. The dashed green line indicates the position of the sample surface.*

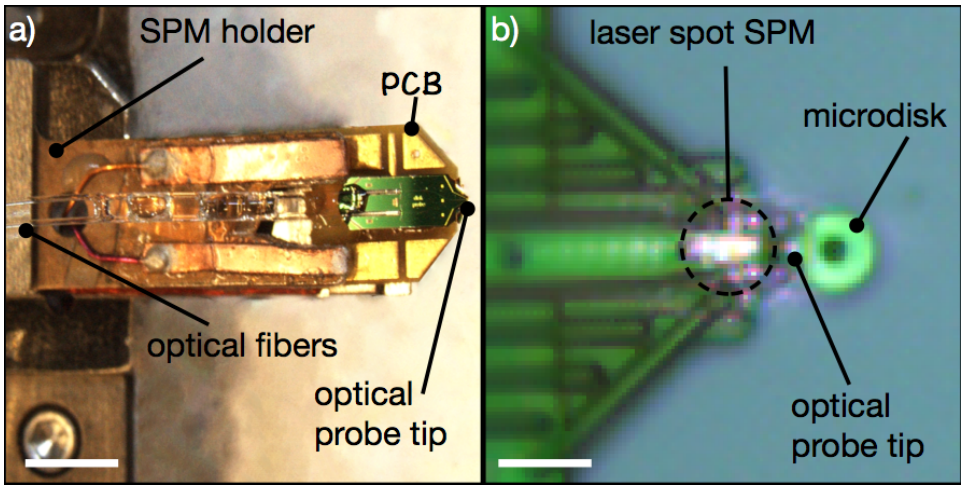

Figure 5.2: *(a) Shows the ≈ 1.5 mm by ≈ 4.5 mm Si chip (green) with the probe at the tip and optical fibers coming out of the V-grooves on the back. The chip and fibers are physically attached to a printed circuit board (PCB, golden) adaptor held in a commercial SPM holder. (b) Shows the SPM camera view of the optical probe positioned in close proximity to a Si microdisk being probed. The laser spot of the beam deflection detection system of the SPM is visible on the probe's cantilever. Scale bars are (a) 4 mm, and (b) 20 µm.*

photodetector [132].

At small separations the probe comes in contact with the surface and the increased cantilever deflection is a linear function of distance. The onset of cantilever deflection marks the point of contact between the probe and the sample. The calibrated close-loop controlled actuation of the SPM can then be used to achieve a desired probe-sample separation.

Optical spectroscopy measurements are based on the optical setup introduced in section 3.2. Light from a laser is sent through a fiber polarization controller and coupled into the probe device input fiber. Polarization is manually adjusted to maximize the evanescent coupling to the photonic structure under investigation. Light intensity from the output fiber is measured with a photodetector. The laser wavelength is swept and the transmission spectrum is recorded, revealing the spectral location and spectral width of the optical cavity modes. Optical power into the probe was ≈ 0.08 mW.

For a first experiment, the Si microdisk with a diameter of ≈ 10 µm,

anchored ≈ 2 µm above the surface of a Si wafer was measured. The microdisk is fabricated from the ≈ 260 nm thick Si device layer of an SOI wafer and has an optical quality factor of ≈ 10^6 [99]. The SPM stage was used to position the disk edge under the probe and the SPM height actuator was used to position the probe in steps of ≈ 50 nm away from the Si micro disk to measure the spectra, revealing the change in optical coupling as a function of the probe/disk gap. Figure 5.3 (b), (c) shows the spectral transmission dips corresponding to a first-radial order transverse magnetic mode of the micro disk for different disk/probe gaps. Figure 5.3 (a) plots the transmission contrast vs. disk-probe gap, and shows that critical coupling is achieved at ≈ 420 nm separation. Near 100 % absorption by the cavity is reached, indicative of good polarization matching.

While an SPM can achieve superior control and automation, for many research and testing applications the calibrated close-loop stage as well as the beam deflection detection system for the automated approach and close-loop control are not necessary. In such situations the probe can be used with a simpler micromanipulator and/or a probe station.

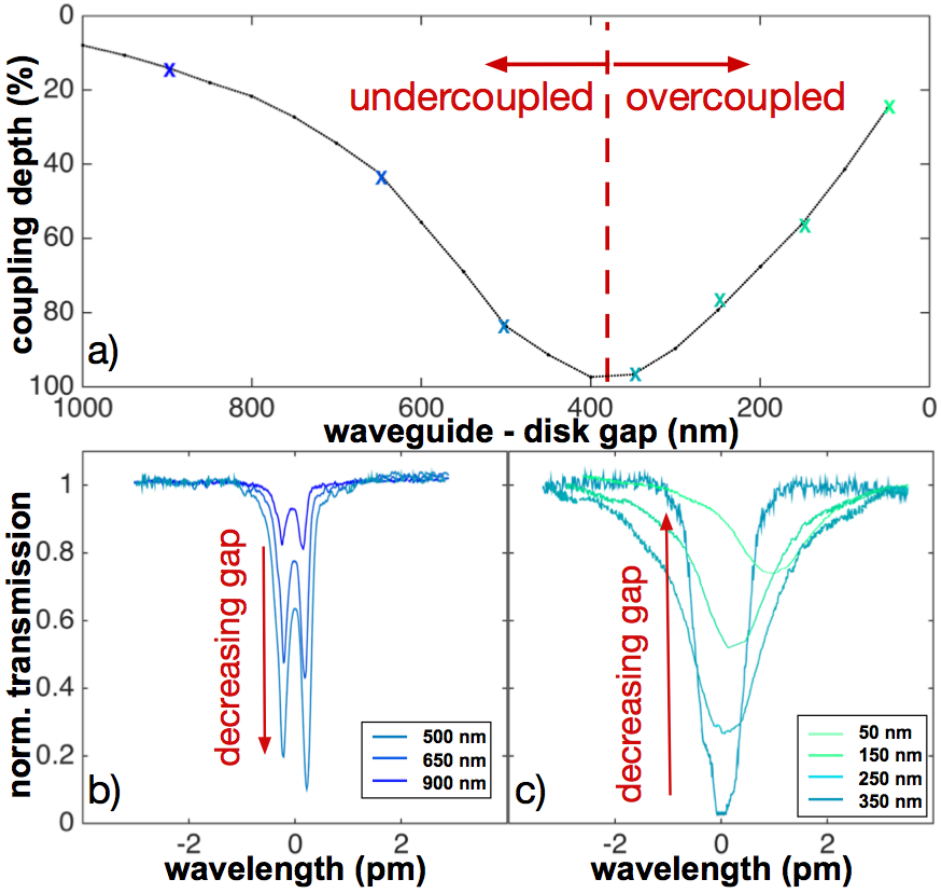

Figure 5.3: *Spectroscopy of a ≈ 10 µm diameter, ≈ 260 nm thick Si microdisk optical cavity using the optical probe. Absorption feature from a transverse magnetic (TM) whispering gallery mode is centered at ≈ 1540.35 nm. (a) Coupling depth as a function of probe- disk spacing with undercoupled and overcoupled regions highlighted. (b) and (c) selected transmission scans taken from the undercoupled and overcoupled regime, as indicated by colored crosses in (a). Intrinsic quality factor of $Q \approx 10^6$ and doublet splitting of ≈ 0.1 GHz are evident from the undercoupled spectra. Based on repeated measurements, the one standard deviation statistical uncertainty is smaller than the data makers.*

5.3 Conclusion

This chapter summarized the development and characterization of a fiber pigtailed optical probe for local, nondestructive testing of photonic structures. The probe was microfabricated in a wafer scale batch-fabrication process. Accurate control over the optical coupling with a commercial scanning probe microscope was demonstrated through spectroscopy of a high quality factor Si micro disk photonic cavity.

6.0 Frequency Stability Measurement

Many transducer applications are on the detection of a change in the mechanical resonance frequency of a resonator, i.e. dynamic atomic force microscopy [111], resonant accelerometer [133] and artificial noses [134]. For a reproducible high sensitivity measurement, the frequency stability of the resonator is essential. It can be affected by noise added to the signal or by fluctuation of the resonator itself [135].

The frequency stability is maximized when random motion of a resonator driven by thermomechanical noise can be resolved by the readout, also called the thermodynamic limit [136–138]. Nevertheless, this limit is often not reached due to numerous sources of frequency fluctuations. They have been theoretically described, like adsorption-desorption [139], temperature noise due to finite heat capacity [140], defect motion [141], or molecular diffusion [135]. Although, the theoretical interest has been attracted, there were only very few experimental studies that identified the sources of the fluctuations [142, 143].

6.1 Experiment

The membrane transducer introduced in section 3.3 were used to investigate the origin of frequency fluctuations. Nanophotonic cavities show a great potential for this measurement application, with the combination of high sensitivity and high bandwidth.

For the frequency stability experiment, a function generator is used to

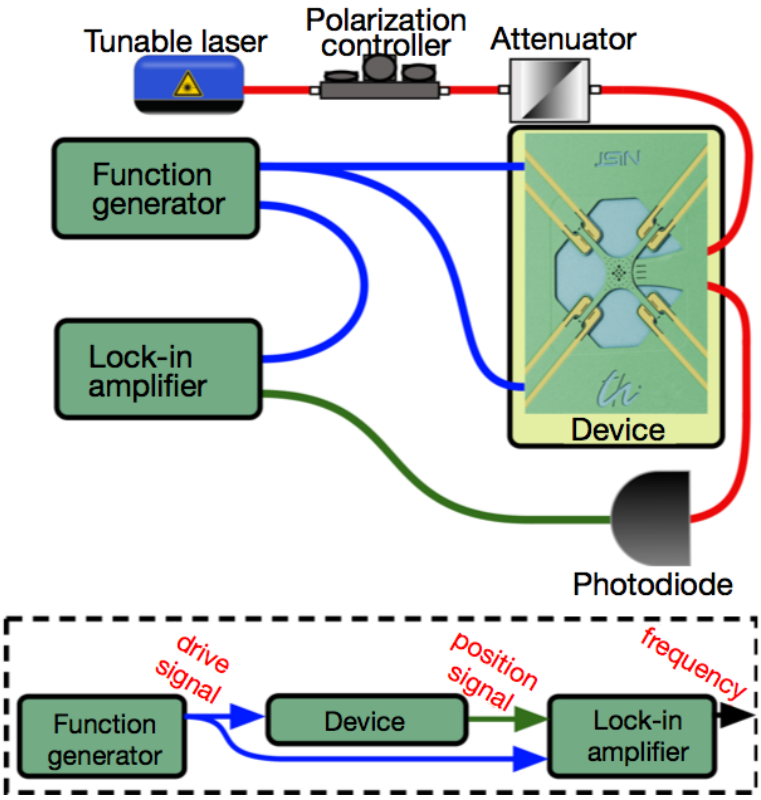

Figure 6.1: *Schematic of the detection setup with an embedded scanning electron micrograph of a membrane transducer. Red lines indicate optical fibers for the transducer readout; blue lines the electrical excitation connection to drive the transducer and supply reference signal for the Lock-in amplifier. The green line represents the electrical read out signal of the transducer. The dashed box (bottom) shows a schematic representation of the electrical signal flow.*

supply an AC signal, with DC offset, to the electrodes of the integrated electrostatic actuator, to excite the membrane with a known signal close to the resonance frequency (319.5 kHz) of the device (Figure 6.1).

The DC offset was chosen to be the peak value of the AC signal. The mechanical motion is transduced through the optical microcavity into an optical transmission modulation and back into an electrical signal by the photodiode.

A lock-in amplifier determines the current resonance frequency of the resonator with the phase value between the reference signal, used to excite the membrane and the signal imprinted on the optical signal. The optical part of the setup is described in section 3.2.

A TM optical mode with an optical quality factor of $\approx 1\text{x}10^6$ was used to carry out this measurement at a very low optical power level of approximately 6.3 µW (- 22 dBm) excitation power, 1.77 µW (-27.5 dBm) at the sensor and 430 nW (-33.6 dBm) at the photodetector, accounting for an estimated 5.5 dB fiber pigtail coupling losses at each facet. Despite the low power, the signal to noise ratio on resonance is approximately 56 dB. Low power was chosen deliberately to eliminate any influence of the optical energy, stored in the cavity mode, on the mechanical resonance frequency of the resonator. This is also known as the optical spring effect [144–148]. This influence was only present above a certain optical energy threshold of ≈ 7 µW (-21.5 dBm). Therefore, the optical input power was reduced to ≈ 1.77 µW (-27.5 dBm) at the sensor, to be well below this threshold.

Figure 6.2 show the Allan deviation as a function of integration time, from ≈ 1 ms to ≈ 30 s [149]. The curves have been labeled by the oscillation amplitude, normalized to the RMS thermal motion:

$$A_{norm} = \frac{A}{x_{rmsthermal}} \tag{6.1}$$

with the oscillation amplitude A and the normlized amplitude A_{norm}. The dashed lines indicate the thermodynamic frequency noise limit corresponding to the individual drive amplitude and the dissipation in the system. The vertical red line represents the energy dissipation time constant t_1 of the membrane resonator, at ≈ 140 ms. The curves for low excitation amplitudes show a good agreement with the thermodynamic limit up to an integration time of ≈ 30 s. At high excitation amplitude, additional, unknown sources of frequency fluctuations have been observed to limit the frequency un-

certainty to slightly below 1 mHz or 15 ppb relative uncertainty across the whole range of the measurement bandwidths.

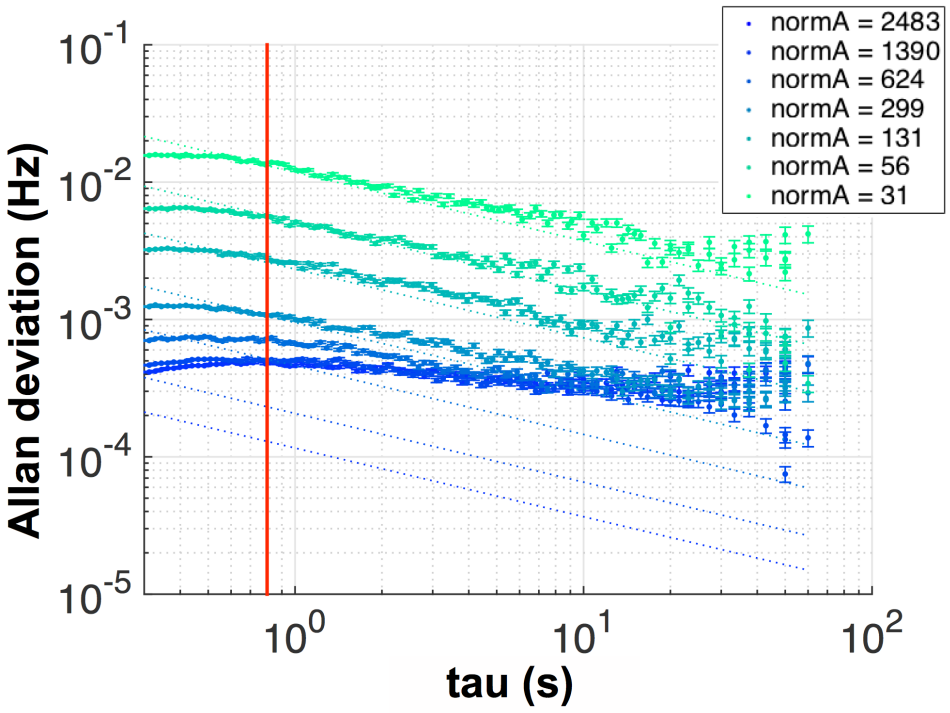

Figure 6.2: *Allan deviation as a function of integration time from 1 ms to 30 s. The dashed lines represent the thermodynamic limit for the measured excitation amplitudes. The curves have been normalized in respect to the driving force used (Eq. 6.1). The dashed lines indicate the thermal noise limit for each drive amplitude and the total additive noise in the system. The vertical red line represents time constant t_1 of the membrane resonator.*

6.2 Conclusion

The performance of the membrane transducers has been studied with the focus on frequency stability. Four different membrane sizes (≈ 650 µm, ≈ 300 µm, ≈ 130 µm, and ≈ 60 µm width) are currently designed to have resonant frequencies ranging from ≈ 70 kHz up to ≈ 1 MHz. A SNR for a thermal motion signal of ≈ 56 dB was presented, which represents an average value for these transducers. The experimentally obtained Allan deviation shows a good agreement of the low motion amplitudes with the thermodynamic limit up to ≈ 30 s. For time scales ≈ 1 s the measured fluctuation amplitudes was smaller then ≈ 0.5 mHz at a resonance frequency of 319 kHz.

7.0 Acceleration Sensor

Micromechanical acceleration sensors have found widespread use in navigation, electronics, motorized vehicles, and vibration monitoring owing to their small size and low power consumption [150]. For example, precise and stable accelerometers could provide a valuable alternative to global positioning systems (GPS) especially in environments where GPS is not available (e.g. tunnels). However, commercially available accelerometer lack sufficient sensitivity for accurate long-distance navigation.

MEMS accelerometers are based on the precise measurement of the displacement of a "proof mass", created by an externally applied acceleration. In most commercial sensors, this displacement is measured capacitively via a change in the gap size between an electrode and the "proof mass", acting as the second electrode [8, 151]. However, the sensitivity that can be reached with this technique is generally limited by the thermal-electronic noise in the readout electronics [150].

Optical readout methods based on interferometry can eliminate this noise and can approach the fundamental thermal-mechanical limit, where the Brownian-motion of the "proof mass" limits the achievable sensitivity [152–155]. This thermal-mechanical noise imposes a fundamental trade-off between bandwidth ($< \omega_m$, the measurable acceleration frequency) and sensitivity (α_{th}) of the accelerometer and can be calculated with the following equation:

$$\alpha_{th} = \sqrt{\frac{4ResBWk_BT}{mQ_m}} \tag{7.1}$$

The equation, derived from the equipartition theorem [156], approximating the accelerometer as a harmonic oscillator with a thermal driven noise force. This equation shows that the product of mQ_m has to be maximized to achieve a high sensitivity for a given bandwidth. However, for a high bandwidth device, a high resolution displacement measurement is required to reach the thermal limit which is difficult to realize with traditional capacitive readout. But this demand in a high resolution displacement measurement can be fulfilled by optomechanical sensors. Recently, acceleration sensors based on optomechanics have been developed, which have the potential to reach the desired sensitivity and bandwidth approaching the thermal-mechanical limit [157, 158]. They already showed sensitivities of a few 100 ng/Hz$^{-1/2}$ with a bandwidth above 10 kHz.

A group at Caltech used optomechanical “zipper cavities" to measure the in-plane motion of a proof mass [159]. The “zipper cavity" consists out of two parallel SiN double side clamped mechanical beam. Each beam has an array of holes that form a 1D photonic crystal cavity. The optical resonance frequency of the cavities is very sensitive to the relative motion between of the two beams due to a high confinement of the optical mode between the beams. This approach reached a sensitivity of ≈ 1 µg at a bandwidth near ≈ 30 kHz. The light was evanescently coupled into the device with optical fiber taper. The light with imprinted motion signal was extracted the same way. The limitations of this approach are the relatively small proof mass of ≈ 10 ng and the coupling procedure used to couple the light in and out of the device.

A cooperation between NIST and the University of Maryland created an accelerometer based on a bulk machined silica proof mass suspended on two leaf springs, with a high finesse fiber-based optical cavity readout [160]. This approach enables the design of a large proof mass (≈ 25 mg), while still maintaining a high mechanical quality factor (≈ 40000). This results in a thermal-noise-limited sensitivity of ≈ 3 ng/Hz$^{-1/2}$ [161]. This approach shows the potential of optomechanics in this field, however, it is challenging to implement the fabrication of these devices in a low-cost batch fabrication process.

7.1 Device Design

An accelerometer based on the batch fabrication process presented earlier (section 2.3) was developed. For the creation of a compact proof mass, the backside anisotropic etch step was replaced by an ICP etch to create a compact proof mass with vertical sidewalls.

False-color scanning electron micrograph of the released device with the fiber-pigtailed chip (Figure 7.1 (a)). The acceleration sensors consists out of four independent sensors, which detect the displacement of a SiN membrane (center). The membrane is connected to the column shaped proof mass shaped out of the Si handle wafer (below the membrane). Sensor #1 and #2 detect the motion of the membrane via a modulation of the gap between the silicon microdisk and the SiN membrane (Figure 7.1 (b)). Sensor #3 detects the resonance frequency of a SiN beam which is on one side connected to the membrane (Figure 7.1 (c)). A moving membrane will modulate the stress in the SiN beam which will be translated into a change in mechanical resonance frequency of the beam. This change in resonance frequency is proportional to the proof mass displacement and allows the measurement of the proof mass position and not only the displacement, compared to sensor #1 and #2. Sensor #1 and #2 can only be used to detect a position change of the proof mass, but not the current position itself.

The principal of operation for sensor #4 is similar to sensor #3. However, sensor #4 has electrodes close to the SiN beam to electrostatically excite the mechanical resonance frequency of the SiN beam (Figure 7.1 (a)). Figure 7.2 (b) shows the measured mechanical frequency noise spectrum of sensor #1. The measurement was performed with a power of ≈ 30 µW at the waveguide/disk coupling region. The measured noise floor correspond to a displacement sensitivity of ≈ 20 fm/Hz$^{-1/2}$. The optical setup used for this measurement was described in section (3.2).

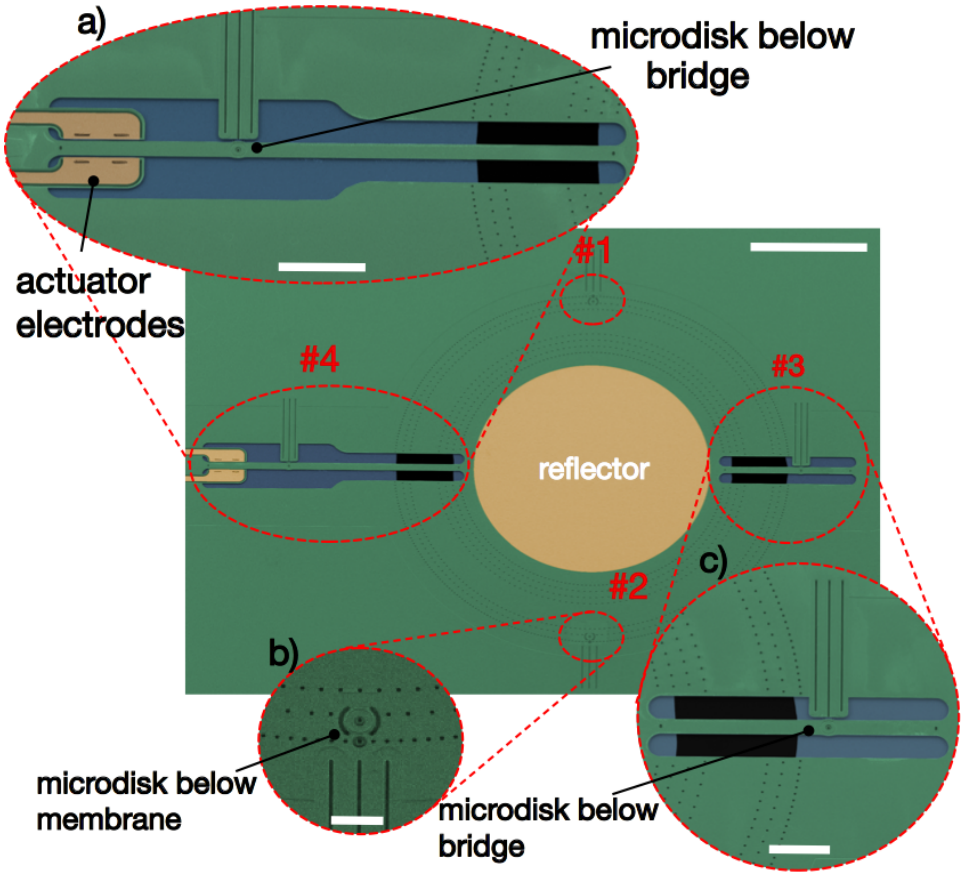

Figure 7.1: *Scanning electron micrograph of the acceleration sensor. The acceleration sensor consist out of four independent sensors. (b) Sensor #1 and #2 are microdisks below the membrane which detect the motion of the membrane. Sensor #3 is a microdisk below a silicon nitride beam. The beam changes the mechanical resonance frequency due to a change of the stress in the beam if the proof mass is moving. This change in mechanical resonance frequency is detected by the microdisk.(a) Sensor #4 is a microdisk below a beam, similar to sensor #3 (c). Furthermore, this sensor has a build-in actuator to electrostatically excite the beam at a given frequency. The seismic mass is located below the center of the membrane. The mass is a ≈ 680 µm high column with a diameter of ≈ 300 µm. In the center of the membrane is a reflector located, which can be used for a reference measurement with an external interferometer. Scale bars are 200 µm, (a) 100 µm, (b) 30 µm and 70 µm.*

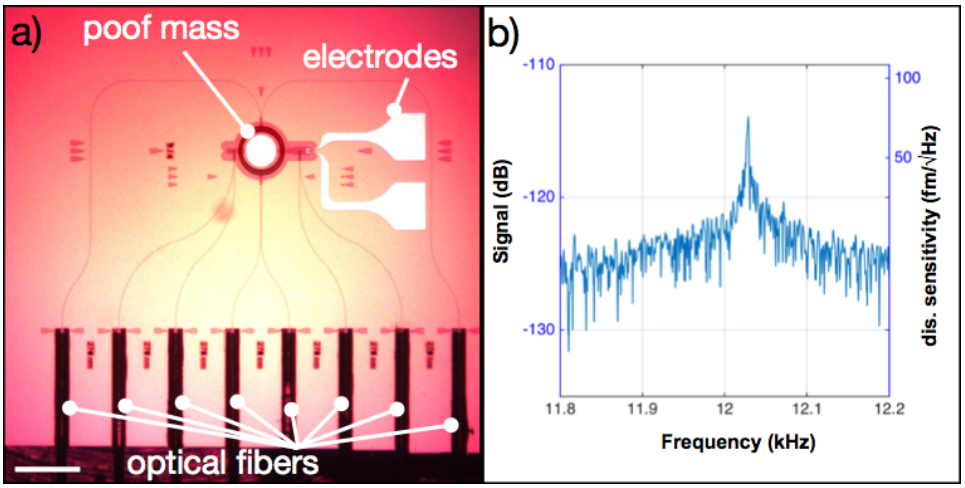

Figure 7.2: *(a) Optical micrograph of the fiber pigtailed acceleration sensor chip. The proof mass is positioned below the circular membrane in the center of the chip; scale bar is 800 µm. (b) Measured mechanical frequency noise spectrum of the membrane, detected with sensor #1. The measurement was performed with a power of ≈ 30 µW at the waveguide/disk coupling region. The measured noise floor correspond to a displacement sensitivity of ≈ 20 fm/Hz$^{-1/2}$. Signal power is reported relative to 1 mW.*

7.2 Conclusion

An acceleration sensor based on seismic mass connected to ≈ 400 µm wide circular membrane was presented. Three different types of optomechanical transducers were introduced to readout the membrane motion. Displacement sensitivities of up to ≈ 20 fm/Hz$^{-1/2}$ have been reported, which corresponds to a Brownian-motion limited acceleration sensitivity of the proof mass at ≈ 20 ng. The advantage of this device compared to the device presented by the cooperation of NIST and UMD is the compatibility with common batch fabrication processes.

8.0 Imaging and Modification of Resonator Modes

Further development of microfabriated resonator-based sensors and transducers necessitates new techniques for device characterization and testing: spectroscopy of optical modes is often insufficient, and rapid, non-invasive techniques for spatial mapping of the mode structures are needed.

Mode mapping is also important for calibration of interaction volumes and local field enhancements as well as for understanding the specific effects of fabrication imperfections. In one example, imperfections can break the spatial symmetry of circular resonators, resulting in spectroscopically observed resonance line splitting. However, spatial information about the imperfections can only be obtained by mapping the modes.

8.1 Introduction

Numerous approaches have been developed for imaging nanoscale photonic and plasmonic resonators including near-field scanning optical microscopy (NSOM) [162–165], cathodoluminescence (CL) [166–169], electron energy loss spectroscopy (EELS) [170], photoemission electron microscopy (PEEM) [171–173], and photo-modulation spectroscopy (PMS) [174, 175]. Each approach presents a distinct set of advantages and tradeoffs. NSOM has been widely used to map nanophotonic devices and encompasses a broad category of tip-based scattering techniques for imaging the electro-magnetic field of nanofabricated optical structures, and advancements in this technique have allowed for local, phase-sensitive measure-

ment of evanescent field vectors [162]. Fundamentally, based on an interaction between the mode's evanescent fields and an externally-introduced physical scatterer, NSOM requires a tradeoff between the scattered signal strength and the probe-induced perturbation to the mode. It is also practically limited by the attainable physical probe geometries. These limitations have insprired the development of probe-less imaging techniques based on both optical and electron beam excitation.

Electron beam techniques includeing CL and EELS have extended imaging of plasmonic structures to the nanometer scale. In these techniques, a focused, scanning electron beams broadly excites a resonator, and the spectrum of cathodoluminescence or electron energy loss provides a map of the local optical density of states [176]. These techniques avoid tip-induced perturbation of the resonator, and are practially limited by the resolution of existing spectrometers to $\approx 800\ cm^{-1}$ in EELS and $\approx 0.5\ cm^{-1}$ in CL. Due to the broad nature of the electron excitation, CL and EELS cannot be used in operando. Photonic modes of dielectric systems have also been mapped using CL including ZnO_2 microdisks [71, 177] and, recently, Si-based photonic crystals [178]. Optical probing techniques including PEEM and PMS use pulsed lasers to generate photoemission and locally modify the refractive index of optical cavities. They are limited in spatial spatial resolution due to diffraction of the pump beam and aberrations in low-energy electron optics, respectively but are capable of achieving extremely high temporal resolution of the electric field.

Recently, focused ion beams (FIB) have been introduced as a promising alternative for spatially-resolved measurement of nanophotonic resonator modes [179]. Such beams penetrate through the evanescent fields and interact with the mode at and just beneath the resonator surface. They exert negligible mechanical force on the resonator structure, and the strength of the probe can be easily adjusted to match the mode's parameters, such as the quality factor (Q). Similar to CL and EELS, the spatial resolution of FIB-based probing is limited only by the volume of the ion collisional cascade which can be of nanometer scale. The spectral resolution is limited only by shot noise in photodetection of the resonance excitation (similar to NSOM) and can be used to probe device in operando. Focused ion beams have also been used to modify photonic devices for suppressions of certain modes [180], and fine control over the location and strength of the FIB-induced

modification of the resonator opens intriguing possibilities for fine-tuning of the optical modes with an unprecedented level of spatial control.

8.2 Experiment

The imaging technique presented here uses the time-varying response of a microdisk resonator to a pulsed ion beam of Li+. The temporal response of the resonator includes two primary effects: a spatially-dependent shift due to local modification of the device index and boundaries, and a rapid thermal shift in the resonance frequency from ion beam heating.

Respectively, these are referred to as the "optical" and "thermal" responses. These two effects occur over separate timescales and can be independently measured. Both responses are useful for device characterization, the optical shift for mapping the optical mode profile and the thermal shift for measuring thermal transport within the device.

In a previous work, a modulated ion beam was used to make linear scans of the optical mode distribution. Here, detailed fitting of the time varying response is used to increase the signal-to-noise ratio for a given ion dose, which allows quantitative separation of the various responses. These improvements enable increased speed of imaging, resulting in an ability to acquire two-dimensional images of the optical field without causing significant change in mode Q or resonant wavelength.

For singlet resonances, azimuthally-symmetric patterns were observed as expected from the associated single-direction traveling wave fields. However, measuring one component of a doublet line in the microdisk spectrum, an azimuthally-periodic standing wave pattern was observed, which is a result of the breaking of the rotational symmetry of the microdisk, presumably by a defect or fabrication imperfections. Notably, it shows that significant persistent modification in the mode spectrum and the spatial pattern can be induced by extended application of the ion beam. As first examples of such mode editing by the focused ion beam, a permanent shifting of the resonance line by more than a linewidth is shown. Also, conversion from a spectral doublet to a singlet with the accompanying restoration of the azimuthally-symmetric traveling wave pattern is shown.

The microdisk device shown in Figure 8.1 (a) is fabricated from a SOI wafer with a device-layer thickness of ≈ 250 nm. The microdisk (≈ 10 μm diameter) and integrated optical waveguides are patterned into the SOI

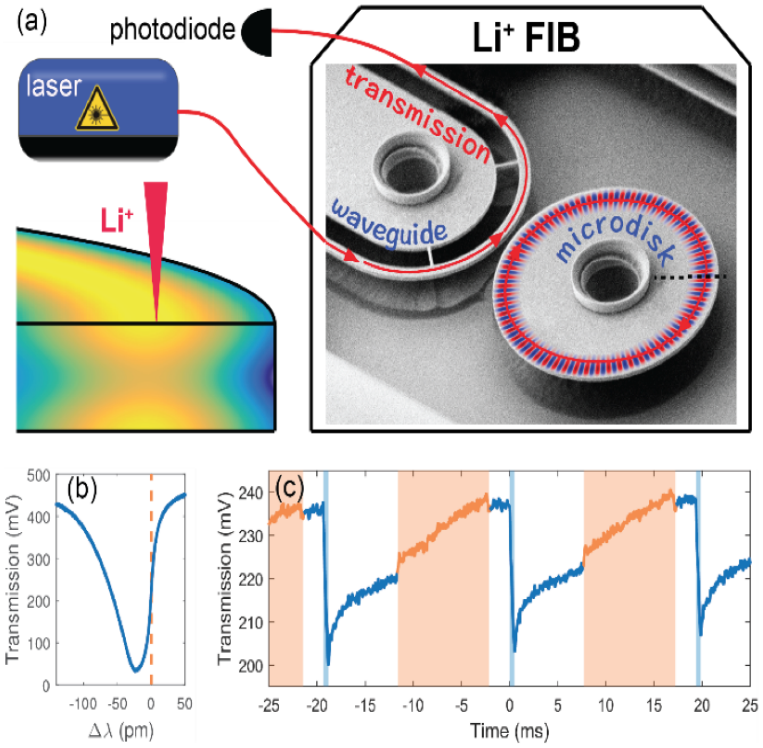

Figure 8.1: *Ion pulse imaging of microdisk resonator modes. (a) The silicon microdisk is housed in a Li+ FIB vacuum chamber with optical fibers connecting the interrogating laser and photodiode to the device. The ion beam is scanned across the resonator mode (dashed line) and perturbs small volumes in the device near the disk surface. The resonator's mode intensity (shown in cross-section) varies both radially and through the device thickness. (b) Spectroscopy of a 0th order transverse magnetic (TM) mode is shown with $Q \approx 20{,}000$ at $\lambda \approx 1523$ nm. The ion pulses incident on the microdisk shift the resonance to longer wavelength, and this shift is read out by tuning the laser (dashed line) to the low frequency side of the resonance and observing the time-varying change in optical transmission of the device. (c) This change is transmission (blue lines) is shown for a series of ≈ 0.5 ms ion pulses (blue bands) incident near the mode maximum, and the absolute magnitude of the spectral shift can be calculated from the transmission measurement in (b). Between each ion pulse, the laser is adjusted to a nominal absorption value (orange band) on the side of the resonance.*

layer using electron beam lithography and reactive ion etching. Annular silicon nitride columns support the microdisk and waveguide structures and are fabricated through an additional multi-step lithographic process. The silicon dioxide cladding layer is removed via wet etching. The gap between the waveguide and the resonator ranges from ≈ 290 nm to ≈ 360 nm and sets the coupling of the waveguide to the resonator. The far ends of the waveguides are tapered to ≈ 100 nm and act as input/output couplers to optical fibers with losses of ≈ 5.5 dB per facet. Further details of the device fabrication are described in Ref [87].

The low-energy, focused pulses of Li+ ions are created from a magneto-optical-trap ion source (MOTIS)-based FIB [181]. The MOTIS employs a laser-cooled gas of neutral $_7$Li as a high-brightness source of ions. The gas is magneto-optically trapped at a temperature of ≈ 0.5 mK and photoionized to generate Li^+ ions with a small spread in both transverse and longitudinal velocity. The ions are accelerated in a uniform electric field to create an ion beam which is scanned and focused using standard ion optics. The ion current is controlled by modulating the photoionization laser power using an acousto-optic modulator which is synchronized with the scanning of the beam deflectors. For this work, the source was operated at an accelerating voltage of ≈ 3.9 keV, and the focal spot size is ≈ 50 nm with ≈ 1 pA of beam current. Details of the microscope are described in Refs. [182, 183]. Spectral shifts of the microdisk resonances are observed by positioning the probing laser on the low frequency side of a microdisk resonance and recording the transmitted power during ion dosing. The transmitted light is measured with a low noise photodetector, and the frequency response of the disk as shown in Figure 8.1 (b) is used to convert changes in optical absorption into a known spectral shift. This is calibrated by simultaneously recording the absorption spectrum from the microdisk and a Fabry-Perot cavity with a calibrated free spectral range of ≈ 1490 MHz. This side-of-line spectroscopic technique provides a direct measure of the resonance shifts, but is susceptible to drift arising from amplitude and frequency noise in the laser, polarization drift in the coupling fibers, and thermal drift of the microdisk resonance. Each of these effects is found to be negligible for the measurement duration described here. Laser frequency and photodetection shot noise are the dominant noise sources. Experiments are nominally performed at room temperature.

The focused Li^+ ion pulses are positioned using the FIB as a microscope and registering the beam position using secondary electron images of fiducial marks on the device. The beam is then step-wise rastered across the structure with a series of ion pulses between 0.2 ms and 0.5 ms in duration. The ion pulses are spaced in time by ≈ 20 ms to allow time for recording the relaxation of the optical shift and for repositioning the laser to a nominal position on the side of the resonance feature where the sensitivity to spectral shifts is maximal. The tuning of the laser between ion pulses is accomplished using a sample-and-hold limited feedback circuit.

The ion-induced shift of the microdisk resonance is analyzed independently for each pulse using least-squares fitting to a two-component model. The two components represent a spatially-local shift arising from ion damage $\Delta_{optical}$ and a position-independent shift arising from ion-beam heating $\Delta_{thermal}$. The optical shift arises from modifications of the silicon lattice that change the local index and boundaries of the device. This modification of the device grows during the ion pulse (with duration t_d) and relaxes afterward; this behavior has been modeled through the piecewise-continuous function of time t expressed in Eq. 8.1.

$$fi£\Delta(t) = \begin{cases} 0 & t \leq 0 \\ \Delta_{thermal} + \Delta_{optical}\frac{e^{-t/\tau_s}-1}{e^{-t_d/\tau_s}-1} 0 \leq t < \leq t_d \\ \Delta_{optical} + \Delta_{relax}[1 - e^{-(t-t_d)/\tau_s}] \ t > t_d \end{cases} \tag{8.1}$$

The optical shift dynamics during the ion dose (0 < t < td) are modeled as linear growth with exponential saturation to capture the finite bound on damage to the device. The relaxation of the shift (t > td) is modelled as exponential decay, similar to the model used to described damage from 3 keV He^+ ions in graphite [184] and is motivated by the linear response to ion damage and relaxation through interstitial-vacancy recombination in the dilute damage limit. Time scales for damage saturation and relaxation in this model are set by τ_s and τ_r, respectively. The maximum optical shift $\Delta_{optical}$ is taken as the value of this fit at td as shown in Figure 8.2 (iii), and the statistical uncertainty in $\Delta_{optical}$ is the fitting uncertainty in this parameter. The thermal response is a constant shift for the duration of the ion pulse and is represented using a stepwise function to capture the rapid thermal shift and recovery of the device as shown in Figure 8.2 (ii). The magnitude and timescale of the optical and thermal responses affords easy separa-

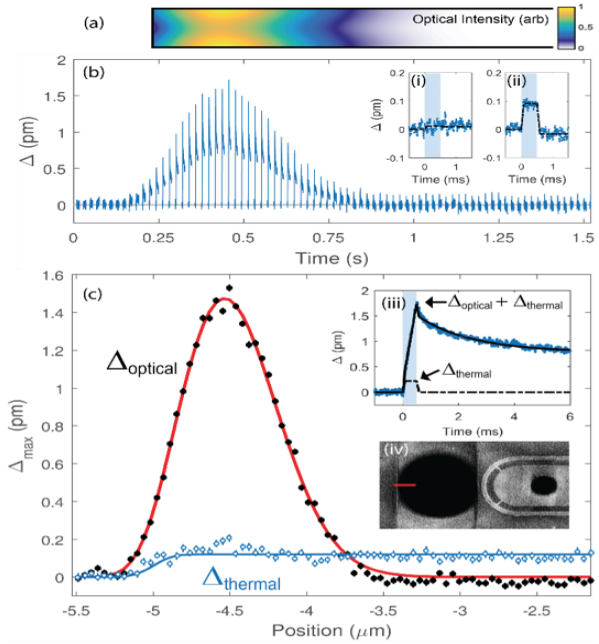

Figure 8.2: *Optical and thermal response of microdisk resonator to ion dose. (a) Across section of the optical mode intensity (color scale) for the 0^{th} radial order mode shown in Figure 8.1 (b) is shown relative to the data in (b) and (c). (b) The ion beam is scanned radially across the edge of the microdisk with a series of ≈ 0.5 ms ion pulses, and the time-varying shift (blue lines) is recorded. Insets show the thermal response to the ion pulses (blue bands) off the disk (i) where no response is observed and on the disk (ii) where the overlap with the optical mode is minimal and only the thermal response of the resonator is observed. Each inset trace (blue points) is an average of 8 consecutive ion pulses with fitting for the thermal shift (dashed line) superposed. (c) The maximum optical shifts (closed circles) and thermal shifts (open circles) are plotted as a function of beam position. Each value is extracted from fitting the time-vary response to Eq. 8.1 as shown in inset (iii). The optical response is compared to numerical simulation of optical mode intensity at the disk surface (red line), and the thermal response is shown to be constant across the disk surface (blue line). Both responses account for the finite size of the ion beam. Inset (iv) shows the orientation of the ≈ 3 μm scan (red bar) using a FIB secondary electron image of the device. Error bars indicate the standard error of the mean; some are smaller than the data point.*

tion through two-component fitting. The response to a series of ion pulses across the edge of the microdisk structure is illustrated in Figure 8.2. In this measurement, a sequence of ≈ 0.5 ms ion pulses containing ≈ 3000 Li^+ ions each is incident near the edge of the microdisk. The magnitude of the response varies as the beam is scanned across the disk edge due to the spatial dependence of the optical mode, and the maximum optical and thermal shifts, $\Delta_{optical}$ and $\Delta_{thermal}$, are extracted at each location. The optical response is compared with a numerically calculated intensity profile of the optical mode intensity near the disk surface in Figure 8.2 (c). The finite size of the ion beam as well as other sources of technical noise blurs the measured signal are included in the data analysis as Gaussian blur. The thermal shift of the resonance is observed to be uniform across the disk surface, and is also limited by the finite probe size at the microdisk edge. Both responses are consistent with a blurring root-mean-square (rms) radius of 100 nm.

The optical shift of the microdisk resonances is understood by considering the effect of the ion beam on the silicon structure including surface swelling and modification of its optical index [179]. The ions interact with the microdisk through a collisional cascade, damaging the Si lattice as the ions scatter and slow in the device. The light mass of the Li+ ion creates a disperse volume of damage with minimal material sputtering [185]. Numerical simulation of the cascade in SRIM [186] shows that 3.9 keV Li+ ions penetrate to a depth of ≈ 31 nm with an rms deviation of ≈ 15 nm. The primary source of damage is due to knock-out collisions that create ≈ 70 silicon interstitial-vacancy pairs per incident ion. Surface sputtering is ≈ 0.3 Si per incident Li+, and ≈ 7 % of the ions backscatter from the device while the rest remain as interstitials in the crystalline silicon (c-Si) lattice. The lateral rms deviation in ion position is ≈ 22 nm. Considering a single ion pulse with 3000 ions and a conservative 100 nm estimation of the beam size, the expected ion flux is ≈ $5{\times}10^12$ cm^{-2} and the vacancy density is ≈ 0.2 % in the center of the damaged volume.

Ion damage shifts the microdisk resonances due to local expansion of the structure and modification of its refractive index. The magnitude of the observed shift in Figure 8.2 is ≈ 1.5 pm for ≈ 3000 ions—this is a fractional shift of the resonant wavelength of ≈ 10^{-6}. The contribution of total shift due to modification of the refractive index can be estimated from the

amorphization fraction, the known ≈ 10 % index difference between crystalline and amorphous Si [187], and the fraction of the mode volume that is damaged. The estimated shift is ≈ 0.15 pm, which is in the same direction as the signal but constitutes only a tenth of the observed value [179, 188]. Calculation of the contribution from surface swelling can be done through optical eigenmode perturbation theory [179], and an expansion of ≈ 0.6 nm would accommodate the observed 1.5 pm shift. The low-energy-Li+-induced expansion of c-Si is unknown and comparison to other measurements of ion-induced expansion are complicated by variation in expansion with ion species, dose, and accelerating voltage. Measurements with 80 keV He+ implanted in c-Si show expansion at the percent level and suggest that surface swelling is likely the explanation for the presently observed signal [189]. Generically, the amplitude of the optical response is expected to differ for fields normal and perpendicular to the disk surface. For the modes explored in this work, the electric field normal to the microdisk surface is negligible, and the expected response can be approximated using the mode intensity. The proximity of the ion damage to the disk surface may also play a role in the magnitude of this effect as self-interstitial silicon has been observed to migrate to the surfaces instead of remaining as lattice interstitials [190].

In addition to the spatially-varying optical response, there is also the rapid thermal shift of the resonance, as shown in Figure 8.2 (ii), caused by ion-beam heating of the microdisk. This response appears independent of the beam location on the microdisk due to rapid thermalization across the structure. The thermal time constant of the microdisk is estimated as $L^2/4DT \approx 300$ ns, where DT is the thermal diffusivity of c-Si ($\approx 0.8\ cm^2 s^{-1}$) and L is the diameter of the disk. Thermalization with the substrate is limited by conduction through the silicon nitride support structure, and the temperature rise of the disk can be estimated through the balance of the ion deposited energy flux (≈ 4 nW) and thermal conduction of the nitride column ($\Delta T\ C_{SiN}\ A/H$), where ΔT is the increase in temperature of the microdisk, A is the cross-sectional area of the support ($\approx 1.4\ \mu m^2$), and H is the height of the support (≈ 2 µm). The thermal conductivity of the nanofabricated silicon nitride structures CSiN is estimated as $\approx 5\ Wm^{-1}K^{-1}$ [191]. Using these values, the temperature rise of the disk was estimated at $\Delta T \approx 0.5$ mK. The thermo-optic coefficient of c-Si ($dn/dT \approx 2\times10^{-4}K^{-1}$ near 1550 nm,

T ≈ 300 K) [192] predicts an expected thermal shift of ≈ 0.15 pm given this temperature rise and is consistent with observed values of ≈ 0.12 pm seen in Figure 8.2. The role of thermal expansion is minimal given the low thermal expansion coefficient of c-Si at ≈ $2.6\times10^{-6}K^{-1}$, two orders of magnitude smaller than the effect from the change in index. In general, microdisk resonators are extraordinarily sensitive thermometers, and the data in Figure 8.2 (ii) show similar capability to state-of-the-art microdisk thermometers [193, 194].

Using the understanding of the time varying response of the microdisk to ion pulses, images of the optical mode intensity were acquired with high signal to noise. Two-dimensional images of 0^{th} and 1st order radial TM modes on two separate devices are shown in Figure 8.3 to demonstrate this ability. For each of these images, an array of ion pulses was positioned near the microdisk edge and the two-component fitting procedure described in Eq. 8.1 was used to extract the optical and thermal response from each ion pulse. The images are composed of 864 and 900 ion pulses lasting 250 µs and 300 µs, respectively (total of ≈ 2 million ions); total image acquisition time is less than 20 s. The measured optical shifts are compared to numerical simulations of the mode intensity. The finite beam width and technical noise are again modelled as a Gaussian blurring of the expected mode profile. The comparison to the predicted mode shows strong agreement that is most visible in the azimuthally averaged data shown in Figure 8.3(b,d). Notably, the agreement indicates that non-linear effects from ion damage are minimal and the ion dose can be considered in the linear-response regime. Higher ion dose leading to significant amorphization is known to have a non-linear scaling and would limit this technique at fluences in the regime of 1016 cm^{-2} [195]. The thermal shifts shown in Figure 8.3 are observed to be constant across the disk surface except near the modal maxima. The resonances used for these images were excited in a quasi-linear regime in which the optical mode spectrum is skewed by a thermal shift due to the absorbed optical power, increasing the apparent slope on the low frequency shoulder of the mode's absorption line. While this non-linear driving is useful for increasing sensitivity to small frequency shifts, it induces hysteretic behavior in the thermal response of the system. This hysteresis is due to interplay between ion heating and rapid modification of the resonance absorption and is evident in the modification of the shape of the thermal

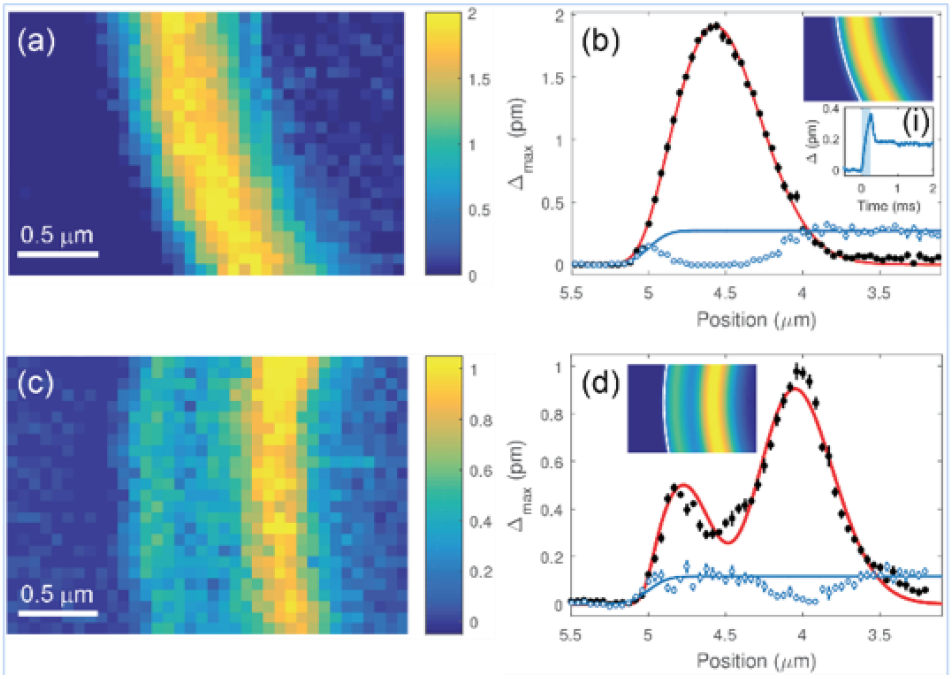

Figure 8.3: *Two-dimensional imaging of nanophotonic modes. (a) Image of the 0^{th} order radial mode showing the spatially-dependent optical shift.(b) Data from (a) are averaged by radial position on the disk. The optical shift (closed circles) is compared with the numerically calculated mode intensity (red line, inset). The thermal shift (open circles) shows effects of non-linear driving of the resonance at the mode position.(i) The thermal response away from the optical mode position shows a hysteretic response in which the original temperature is not restored after the ion pulse. This resonance is the same as described in Figure 8.2 and was interrogated using 250 μs, 1 pA pulses (≈ 1500 ions).(c) Image of a 1^{st} order radial mode showing the optical response to 300 μs ion pulses on a separate device with a $Q \approx 5000$ and λ 1538 nm. (d) The optical response (closed circles) is compared to the numerically calculated mode profile (red line, inset) and the thermal response (open circles) again shows a hysteretic response that is uniform across the disk except at the mode maximum.*

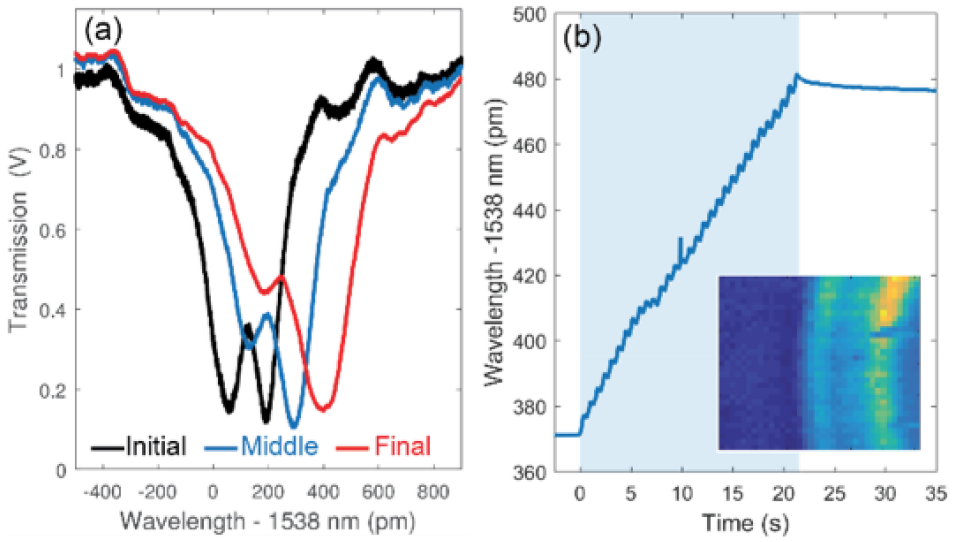

Figure 8.4: *Persistent spectroscopic shifts of microdisk modes due to ion imaging. (a) A doublet mode (same as Figure 8.3 (c) spectrum is measured interleaved around two separate 2D imaging sequences. The curves correspond to the initial spectrum (black), and the spectrum after the first (blue) and second (red) 2D image. The spectra show that the modes are red-shifted and broadened during imaging, and that coupling to the lower-wavelength mode becomes dramatically reduced. (b) The wavelength of the laser is monitored using an optical wavemeter during the second imaging sequence (shaded area) and shows the stepwise shift of the disk resonance as the pulsed ion beam is rastered across the microdisk surface. The inset shows the resulting map of the optical mode.*

response shown in Figure 8.3 (i) away from a step response and in the shift's partial recovery after the ion pulse. This behavior was modeled by fitting to a heuristic function, and the plotted values correspond to the maximum of that function.

Repeated imaging of a disk mode is ultimately limited by broadening of the optical resonances, attributed to increased optical losses due to ion damage. Nevertheless, it is possible to image large areas without significant device degradation. The imaging in Figure 8.3 (c) was repeated 6 times with an estimated total charge of ≈ 2 pC (≈ 0.6 pC in the mode volume). During this process the mode Q decreased by approximately a factor of 2. The loss in sensitivity can be partially offset through increasing the optical power

and thereby decreasing the detection shot noise. A careful measurement of the mode spectrum changes in a doublet resonance during ion imaging is shown in Figure 8.4 (a). Starting from the pristine resonator with the mode used in Figure 8.3 (c), the spectrum before was measured, in the middle, and after two imaging sequences. The spectrum is observed to globally shift to longer wavelength by ≈ 100 pm per image with ≈ 750 000 ions incident on the portion of the microdisk occupied by the mode. At the same time, the lower frequency peak was broadened by ≈ 75 pm per image. The process of adjusting the interrogation laser frequency to follow the resonance is shown in Figure 8.4 (b) during one of the imaging sequences. Here the stepwise shifting of the mode follows the rastering of the ion beam across the disk surface, demonstrating a gradual and controlled shift of the mode line by more than a linewidth. Note that associated with this shift is an inevitable, but relatively minor, change in Q. Understanding and limiting this change in Q is the subject of a future study.

Ion imaging can also be used to explore mode doublets. For perfectly circular disks, clockwise (CW) and counter-clockwise (CCW) whispering gallery modes are degenerate due to rotational symmetry of the disk. However, small fabrication imperfections and defects are in some cases sufficient to break the symmetry, leading to doublets in the mode spectrum. These doublets correspond to pairs of standing wave modes with slightly different energies, arising from mixing between CW and CCW propagating waves. The nodal position of the lower- and higher-energy standing waves is dictated by the details of the spatial symmetry breaking disorder. Modifying the symmetry-breaking disorder and/or modifying the photon lifetime (linewidth) can cause the relative coupling of the two modes to change as is shown in Figure 8.4 (a). In this data, repeated ion dosing dramatically reduces the effective coupling of the high-frequency mode. Additionally, distinct standing wave modes can be individually measured using this technique as shown in Figure 8.5 (a) where a TM, 0^{th} radial order mode is imaged. Given sufficient spectral separation between the modes, independent addressing and imaging can be achieved. Here the lower frequency mode of a doublet was imaged and five peaks on the standing wave pattern were observed. The interferometric visibility of the observed standing wave is ≈ 0.28. The maximum theoretically expected value for the visibility is ≈ 0.7 due to the 90° phase shift of the azimuthal electric field relative to the

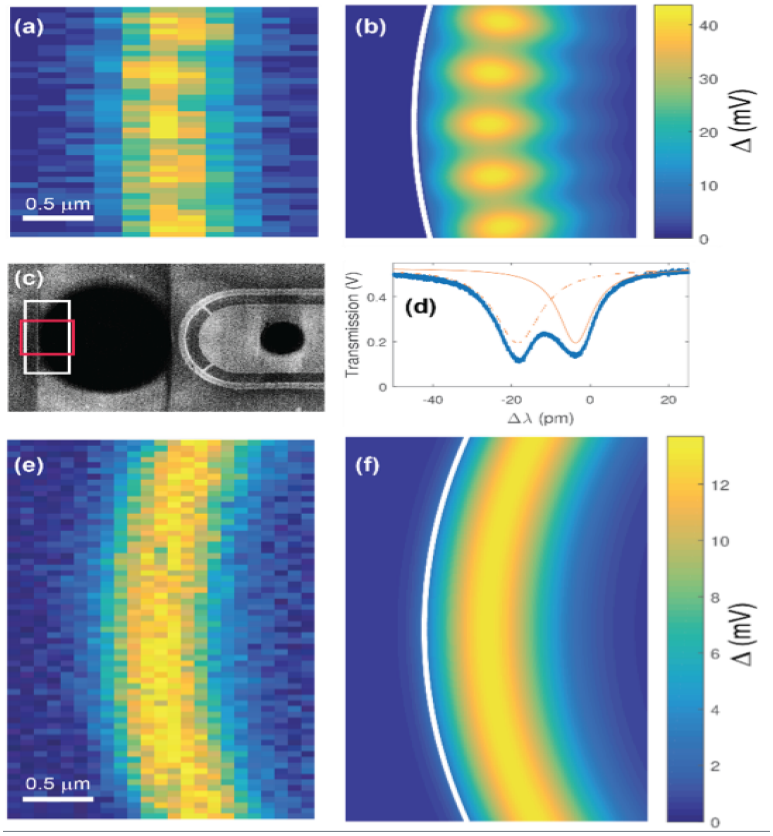

Figure 8.5: *Imaging of optical standing wave and ion beam mode editing. (a) 2D image of a zeroth radial order, TM standing wave showing $\Delta_{optical}$ at each point in space. This image is an average of four data sets taken of the same area; scale bars (white) are 0.5 μm. (b) Comparison of the imaged mode to numerical mode simulation showing interferometric visibility of ≈ 0.28. (c) FIB secondary electron image of microdisk device showing the orientation of the images in parts (a) in red and (e) in white. (d) Optical transmission spectrum of the standing wave resonance before acquiring image in (a). Light solid and dashed lines indicate the two separate resonances. (e) Larger area scan at the same microdisk location after ion beam dose shows no standing wave visibility. No standing wave is apparent in this data and comparison to the expect traveling wave mode shape is shown in (f).*

radial and normal components of the field. The finite resolution of the ion beam and finite spectral mode overlap shown in Figure 8.5 (d) also contribute to a reduction in the standing wave visibility. Assuming Gaussian blurring with an rms radius of 100 nm, one expects a visibility of ≈ 0.29 in the mode response, in strong agreement with the data shown in Figure 8.5 (b). Additionally, the mode order is found to be $l = 35$ in agreement with spectroscopy of the disk modes. Further imaging of this microdisk leads to permanently broadening of the mode's spectrum. When the photon lifetime becomes shorter than the CW-CCW scattering rate, the mode splitting and the resulting standing wave are no longer resolved. Imaging of the mode distribution after this broadening in Figure 8.5 (e) shows no visible standing wave and demonstrates the ability to spatially image and permanently edit high quality factor optical modes.

8.3 Conclusion

The optical and thermal response of a microdisk resonator to pulses of low energy ions from a focused beam was imaged. This enabled to form images of the device's optical mode intensity in the linear response regime with both higher sensitivity and speed. With higher cumulative dose, persistent editing of mode spectra and spatial patterns was demonstrated. Future extensions of this technique using focused ion beams to locally perturb optical structures at higher spatial and temporal resolution will allow for improved imaging of sub-wavelength structures. Fundamentally, the technique is only limited by the volume of the ion cascade in the material, and this volume can be minimized using high resolution, low energy beams that are currently being developed using MOTIS and similar sources [196]. There is also an opportunity to use high energy ions that will penetrate deeper into nanophotonic devices to allow for mapping of optical structures using He+ and other forms of ion microscopy. Additionally, detailed understanding of the time varying optical response will provide insight into the process of thermal annealing of ion damage, which is of relevance to a broad range of electronic and optical materials.

9.0 Conclusion

This thesis describes the basic design, simulation, fabrication and characterization of a fully integrated, fiber pigtailed, optomechanical force and displacement transducer platform with integrated actuation.

The approach of full Si integration of all stationary nanophotonic components with mechanically separated movable components creates an opportunity to independently engineer these two parts for a variety of MEMS and NEMS sensing applications that require high precision, high bandwidth, and small footprint. Further integration of actuators for static and dynamic actuation is also possible.

Overhanging mechanical probes with different actuation schemes, geometries, and anchor condition were presented. The transducer behavior was analyzed in therms of displacement sensitivity, readout tuning and frequency stability. The probes are between 25 µm and 60 µm long and cover a frequency range between 100 kHz and 1 MHz for the first harmonic with a spring constant between 0.03 $\frac{N}{m}$ and 100 $\frac{N}{m}$. The integrated electrical actuation can also be used to tune the readout gain of some designs by up to 95 %, which allows us to trade a decrease in displacement sensitivity against an increase in the dynamic measurement range.

The probes have been operated in a modified SPM in single probe and probe array configuration. The simultaneous optical readout of multiple optomechanical probes with a single tunable laser at a fixed wavelength was demonstrated. The advantage of this technique is a significant reduction in the readout setup complexity and cost, as well as the simplification of

on-chip photonic structures. Two SPM images acquired with the integrated optical readout were presented, showing that the images acquired are comparable to those taken with the conventional SPM OBD readout.

In addition, membranes with four different sizes and integrated electrostatic actuation, to cover the resonance frequency range from a few tens of Kilohertz up to a few Megahertz, have been fabricated. The performance of the membrane transducers has been studied with the focus on frequency stability. Four different membrane sizes (≈ 650 µm, ≈ 300 µm, ≈ 130 µm, and ≈ 60 µm width) are currently designed to have resonance frequencies ranging from ≈ 70 kHz up to ≈ 1 MHz in the first harmonic. A SNR for a thermal motion signal of ≈ 56 dB has been presented, which represents an average value for these transducers. The experimentally obtained Allan deviation shows a good agreement of the low motion amplitudes with the thermodynamic limit up to ≈ 30 s. For time scales ≈ 1 s the measured fluctuation amplitudes was smaller then ≈ 0.5 mHz.

Furthermore, the design and operation of an optical probe for local, non-destructive testing of photonic structures was presented. Accurate control over the optical coupling with a commercial scanning probe microscope has been demonstrated through spectroscopy of a high quality factor Si microdisk photonic cavity.

The universal fabrication process was also used to design acceleration sensors based on seismic mass connected to ≈ 400 µm wide circular membrane. Displacement sensitivities of up to ≈ 20 fm/Hz$^{-1/2}$ have been reported. Which correspond to a Brownian-motion limited acceleration sensitivity of the proof mass at ≈ 20 ng.

In addition, a focus ion beam setup was used to study the optical and thermal response of a microdisk resonator to pulses of low energy ions. This enabled to form images of the device's optical mode intensity in the linear response regime with both higher sensitivity and speed. With higher cumulative dose, persistent editing of mode spectra and spatial patterns was demonstrated. Future extensions of this technique using focused ion beams to locally perturb optical structures at higher spatial and temporal resolution will allow for improved imaging of sub-wavelength structures. Fundamentally, the technique is only limited by the volume of the ion cascade in the material, and this volume can be minimized using high resolution, low energy beams that are currently being developed using MOTIS and

similar sources [196]. There is also an opportunity to use high energy ions that will penetrate deeper into nanophotonic devices to allow for mapping of optical structures using He+ and other forms of ion microscopy. Additionally, detailed understanding of the time varying optical response will provide insight into the process of thermal annealing of ion damage, which is of relevance to a broad range of electronic and optical materials.

Bibliography

[1] Guiti Zolfagharkhani, Alexei Gaidarzhy, Pascal Degiovanni, Stefan Kettemann, Peter Fulde, and Pritiraj Mohanty. Nanomechanical detection of itinerant electron spin flip. *Nature Nanotechnology*, 3(12):720–723, November 2008.

[2] J Chaste, A Eichler, J Moser, G Ceballos, R Rurali, and A Bachtold. A nanomechanical mass sensor with yoctogram resolution. *Nature Nanotechnology*, 7(5):301–304, April 2012.

[3] Silvan Schmid, Luis Guillermo Villanueva, and Michael Lee Roukes. *Fundamentals of Nanomechanical Resonators*. Springer, Cham, June 2016.

[4] C A Regal, J D Teufel, and K W Lehnert. Measuring nanomechanical motion with a microwave cavity interferometer . *Nature Physics*, 4:555–560, April 2008.

[5] M D LaHaye. Approaching the Quantum Limit of a Nanomechanical Resonator. *Science*, 304(5667):74–77, April 2004.

[6] Patrick A Truitt, Jared B Hertzberg, C C Huang, Kamil L Ekinci, and Keith C Schwab. Efficient and Sensitive Capacitive Readout of Nanomechanical Resonator Arrays. *Nano Letters*, 7(1):120–126, January 2007.

[7] C Linder, E Zimmermann, and N F de Rooij. Capacitive polysilicon resonator with MOS detection circuit. *Sensors and Actuators A: Physical*, 27(1-3):591–595, March 2001.

[8] H Kulah, J Chae, N Yazdi, and K Najafi. Noise Analysis and Characterization of a Sigma-Delta Capacitive Microaccelerometer. *IEEE Journal of Solid-State Circuits*, 41(2):352–361, February 2006.

[9] B Yurke, D S Greywall, A N Pargellis, and P A Busch. Theory of amplifier-noise evasion in an oscillator employing a nonlinear resonator. *Physical Review A*, 51(5):4211–4229, May 1995.

[10] W J Venstra, H J R Westra, K Babaei Gavan, and H S J van der Zant. Magnetomotive drive and detection of clamped-clamped mechanical resonators in water. *Applied Physics Letters*, 95(4):1–4, January 2010.

[11] Yossi Weizmann, Roey Elnathan, Oleg Lioubashevski, and Itamar Willner. Magnetomechanical Detection of the Specific Activities of Endonucleases by Cantilevers. *Nano Letters*, 5(4):741–744, April 2005.

[12] T Gotszalk, P Grabiec, and I W Rangelow. Piezoresistive sensors for scanning probe microscopy. *Ultramicroscopy*, 82(1-4):39–48, January 2000.

[13] J Suh, A J Weinstein, C U Lei, E E Wollman, S K Steinke, P Meystre, A A Clerk, and K C Schwab. Piezoresistive sensing of a dielectrically actauted silicon bar resonator. *Science*, 344(6189):1262–1265, June 2014.

[14] Teodor Gotszalk, Piotr Grabiec, and Ivo W Rangelow. Calibration and examination of piezoresistive Wheatstone bridge cantilevers for scanning probe microscopy. *Ultramicroscopy*, 97(1-4):385–389, October 2003.

[15] Anja Boisen. Nanoelectromechanical systems: Mass spec goes nanomechanical. *Nature Nanotechnology*, 4(7):404–405, July 2009.

[16] Yi Qi, Noah T Jafferis, Kenneth Lyons, Jr., Christine M Lee, Habib Ahmad, and Michael C McAlpine. Piezoelectric Ribbons Printed onto

Rubber for Flexible Energy Conversion. *Nano Letters*, 10(2):524–528, February 2010.

[17] Yu Hui, Juan Sebastian Gomez-Diaz, Zhenyun Qian, Andrea Alù, and Matteo Rinaldi. Plasmonic piezoelectric nanomechanical resonator for spectrally selective infrared sensing. *Nature Communications*, 7:11249, April 2016.

[18] Thomas Michels and Ivo W Rangelow. Review of scanning probe micromachining and its applications within nanoscience. *Microelectronic Engineering*, 126(C):191–203, August 2014.

[19] Gerhard Meyer and Nabil M Amer. Novel optical approach to atomic force microscopy. *Applied Physics Letters*, 53(12):1045–1047, September 1988.

[20] S Alexander, L Hellemans, O Marti, J Schneir, V Elings, P K Hansma, Matt Longmire, and John Gurley. An atomic-resolution atomic-force microscope implemented using an optical lever. *Journal of Applied Physics*, 65(1):164–167, January 1989.

[21] D Rugar, H J Mamin, and P Guethner. Improved fiber-optic interferometer for atomic force microscopy. *Applied Physics Letters*, 55(25):2588–2590, December 1989.

[22] I Tittonen, G Breitenbach, T Kalkbrenner, T Müller, R Conradt, S Schiller, E Steinsland, N Blanc, and N F de Rooij. Interferometric measurements of the position of a macroscopic body: Towards observation of quantum limits. *Physical Review A*, 59(2):1038–1044, February 1999.

[23] B W Hoogenboom, P L T M Frederix, J L Yang, S Martin, Y Pellmont, M Steinacher, S Zäch, E Langenbach, H J Heimbeck, A Engel, and H J Hug. A Fabry-Perot interferometer for micrometer-sized cantilevers. *Applied Physics Letters*, 86(7), February 2005.

[24] R Erlandsson, G M McClelland, C M Mate, and S Chiang. Atomic force microscopy using optical interferometrie. *J. Vac. Sci. Technol.*, 6(266):266–270, 1988.

[25] Ivan Favero and Khaled Karrai. Optomechanics of deformable optical cavities. *Nature Photonics*, 3(4):201–205, April 2009.

[26] Michael Först, Jan Niehusmann, Tobias Plötzing, Jens Bolten, Thorsten Wahlbrink, Christian Moormann, and Heinrich Kurz. High-speed all-optical switching in ion-implanted silicon-on-insulator microring resonators. *Optics Letters*, 32(14):2046, 2007.

[27] Vilson R Almeida and Michal Lipson. Optical bistability on a silicon chip. *Optics Letters*, 29(20):2387, 2004.

[28] Yannick Dumeige and Patrice Féron. Dispersive tristability in microring resonators. *Physical Review E*, 72(6):57, December 2005.

[29] P Rabiei, W H Steier, Cheng Zhang, and L R Dalton. Polymer micro-ring filters and modulators. *Lightwave Technology, Journal of*, 20(11):1968–1975, November 2002.

[30] Qianfan Xu, Bradley Schmidt, Sameer Pradhan, and Michal Lipson. Micrometre-scale silicon electro-optic modulator. *Nature*, 435(7040):325–327, May 2005.

[31] Tazawa, Ying-Hao Kuo, Dunayevskiy, Jingdong Luo, Jen, Fetterman, and Steier. Ring resonator-based electrooptic polymer traveling-wave modulator. *Lightwave Technology, Journal of*, 24(9):3514–3519, 2006.

[32] T A Ibrahim, K Amarnath, L C Kuo, R Grover, V Van, and P T Ho. Photonic logic NOR gate based on two symmetric microring resonators. *Optics Letters*, 29(23):2779, 2004.

[33] T A Ibrahim, R Grover, L C Kuo, S Kanakaraju, L C Calhoun, and P T Ho. All-optical AND/NAND logic gates using semiconductor microresonators. *Photonics Technology Letters, IEEE*, 15(10):1422–1424, 2003.

[34] V Van, T A Ibrahim, P P Absil, F G Johnson, R Grover, and P T Ho. Optical signal processing using nonlinear semiconductor microring resonators. *IEEE Journal of Selected Topics in Quantum Electronics*, 8(3):705–713, May 2002.

[35] Chung-Yen Chao and L Jay Guo. Biochemical sensors based on polymer microrings with sharp asymmetrical resonance. *Applied Physics Letters*, 83(8):1527–1529, August 2003.

[36] A Yalcin, K C Popat, J C Aldridge, T A Desai, J Hryniewicz, N Chbouki, B E Little, Oliver King, V Van, Sai Chu, D Gill, M Anthes-Washburn, M S Unlu, and B B Goldberg. Optical sensing of biomolecules using microring resonators. *IEEE Journal of Selected Topics in Quantum Electronics*, 12(1):148–155, 2006.

[37] Katrien De Vos, Irene Bartolozzi, Etienne Schacht, Peter Bienstman, and Roel Baets. Silicon-on-Insulator microring resonator for sensitive and label-free biosensing. *Optics express*, 15(12):7610–7615, 2007.

[38] Fengnian Xia, Lidija Sekaric, and Yurii Vlasov. Ultracompact optical buffers on a silicon chip. *Nature Photonics*, 1(1):65–71, January 2007.

[39] Joyce K S Poon, Jacob Scheuer, Yong Xu, and Amnon Yariv. Designing coupled-resonator optical waveguide delay lines. *Journal of the Optical Society of America B*, 21(9):1665–1673, 2004.

[40] F Morichetti, A Melloni, A Breda, A Canciamilla, C Ferrari, and M Martinelli. A reconfigurable architecture for continuously variable optical slow-wave delay lines. *Optics express*, 15(25):17273–17282, 2007.

[41] Andrea Melloni, Francesco Morichetti, Carlo Ferrari, and Mario Martinelli. Continuously tunable 1 byte delay in coupled-resonator optical waveguides. *Optics Letters*, 33(20):2389–2391, 2008.

[42] Francesco Morichetti, Andrea Melloni, Carlo Ferrari, and Mario Martinelli. Error-free continuously-tunable delay at 10 Gbit/s in a reconfigurable on-chip delay-line. *Optics express*, 16(12):8395, 2008.

[43] Jacob B Khurgin. Optical buffers based on slow light in electromagnetically induced transparent media and coupled resonator structures: comparative analysis. *Journal of the Optical Society of America B*, 22(5):1062–1074, 2005.

[44] Landobasa Yosef Mario and Mee Koy Chin. Optical buffer with higher delay-bandwidth product in a two-ring system. *Optics express*, 16(3):1796–1807, 2008.

[45] J V Hryniewicz, P P Absil, B E Little, R A Wilson, and P T Ho. Higher order filter response in coupled microring resonators. *Photonics Technology Letters, IEEE*, 12(3):320–322, 2000.

[46] Andrea Melloni. Synthesis of a parallel-coupled ring-resonator filter. *Optics Letters*, 26(12):917–919, 2001.

[47] B E Little, S T Chu, P P Absil, J V Hryniewicz, F G Johnson, F Seiferth, D Gill, V Van, O King, and M Trakalo. Very High-Order Microring Resonator Filters for WDM Applications. *Photonics Technology Letters, IEEE*, 16(10):2263–2265, October 2004.

[48] T Barwicz, M A Popovic, M R Watts, P T Rakich, E P Ippen, and H I Smith. Fabrication of add-drop filters based on frequency-matched microring resonators. *Lightwave Technology, Journal of*, 24(5):2207–2218, 2006.

[49] Fengnian Xia, Mike Rooks, Lidija Sekaric, and Yurii Vlasov. Ultra-compact high order ring resonator filters using submicron silicon photonic wires for on-chip optical interconnects. *Optics express*, 15(19):11934, 2007.

[50] Shijun Xiao, Maroof H Khan, Hao Shen, and Minghao Qi. A highly compact third-order silicon microring add-drop filter with a very large free spectral range, a flat passband and a low delay dispersion. *Optics express*, 15(22):14765, 2007.

[51] Shijun Xiao, Maroof H Khan, Hao Shen, and Minghao Qi. Silicon-on-Insulator Microring Add-Drop Filters With Free Spectral Ranges Over 30 nm. *Lightwave Technology, Journal of*, 26(2):228–236, 2008.

[52] Landobasa Yosef Mario Tobing, Pieter Dumon, Roel Baets, and Mee Koy Chin. Boxlike filter response based on complementary photonic bandgaps in two-dimensional microresonator arrays. *Optics Letters*, 33(21):2512, 2008.

[53] Kerry J Vahala. Optical microcavities. *Nature*, 424(6950):839–846, August 2003.

[54] John D Joannopoulos, Steven G Johnson, Joshua N Winn, and Robert D Meade. *Photonic crystals: molding the flow of light; 2nd ed.* Princeton Univ., Princeton, NJ, 2008.

[55] J Vuckovic, O Painter, Yong Xu, A Yariv, and A Scherer. Finite-difference time-domain calculation of the spontaneous emission coupling factor in optical microcavities. *IEEE Journal of Quantum Electronics*, 35(8):1168–1175, 1999.

[56] O Painter, J Vuckovic, and A Scherer. Defect modes of a two-dimensional photonic crystal in an optically thin dielectric slab. *Journal of the Optical Society of America B*, 16(2):275–285, 1999.

[57] Y Xu, J S Vučković, R K Lee, O J Painter, A Scherer, and A Yariv. Finite-difference time-domain calculation of spontaneous emission lifetime in a microcavity. *Journal of the Optical Society of America B*, 16(3):465–474, 1999.

[58] Hansuek Lee, Tong Chen, Jiang Li, Ki Youl Yang, Seokmin Jeon, Oskar Painter, and Kerry J Vahala. Chemically etched ultrahigh-Q wedge-resonator on a silicon chip. *Nature Photonics*, 6(6):369–373, June 2012.

[59] Ehsan Shah Hosseini, Siva Yegnanarayanan, Amir H Atabaki, Mohammad Soltani, and Ali Adibi. High quality planar silicon nitride microdisk resonators for integrated photonics in the visible wavelength range. *Optics express*, 17(17):14543–14551, 2009.

[60] Mohammad Soltani, Siva Yegnanarayanan, and Ali Adibi. Ultra-high Q planar silicon microdisk resonators for chip-scale silicon photonics. *Optics express*, 15(8):4694–4704, 2007.

[61] V B Braginsky, M L Gorodetsky, and V S Ilchenko. Quality-factor and nonlinear properties of optical whispering-gallery modes. *Physics Letters A*, 137(7-8):393–397, May 1989.

[62] S I Shopova, G Farca, A Naweed, and A T Rosenberger. Whispering-gallery-mode microlaser consisting of a HgTe-quantum-dot-coated

microsphere. In *Frontiers in Optics*, pages 365–372, Washington, D.C., 2003. OSA.

[63] Jingming Cao. The entangled quantum photons generation in whispering gallery mode resonator of silica microsphere. In *Frontiers in Optics*, pages 213–217, Washington, D.C., 2017. OSA.

[64] T Carmon, T J Kippenberg, L Yang, H Rokhsari, S Spillane, and K J Vahala. Feedback control of ultra-high-Q microcavities: application to micro-Raman lasers and micro- parametric oscillators. *Optical Express*, 13(9):3358–3360, April 2005.

[65] Karen E Grutter, Alejandro Grine, Myung-Ki Kim, Niels Quack, Tristan Rocheleau, Clark T Nguyen, and Ming C Wu. A Platform for On-Chip Silica Optomechanical Oscillators with Integrated Waveguides. In *CLEO: Science and Innovations*, pages 142–150, Washington, D.C., 2012. OSA.

[66] Karen E Grutter, Anthony Yeh, Alejandro Grine, and Ming C Wu. An Integrated, Silica-Based, MEMS-Actuated, Tunable-Bandwidth Optical Filter with Low Minimum Bandwidth. In *CLEO: Science and Innovations*, pages CTh4F.3–2, Washington, D.C., 2013. OSA.

[67] Ann Britt Petermann, Arthur Varkentin, Bernhard Roth, Uwe Morgner, and Merve Meinhardt-Wollweber. All-polymer whispering gallery mode sensor system. *Optics express*, 24(6):6052–6062, 2016.

[68] Ann Britt Petermann, Bernhard Roth, Uwe Morgner, and Merve Meinhardt-Wollweber. All-polymer whispering gallery mode sensor for application in optofluidics. *Optical Data Processing and Storage*, 3(1):6052, 2017.

[69] K C Balram, Marcelo Davanço, J Y Lim, J D Song, and K Srinivasan. Moving boundary and photoelastic coupling in GaAs optomechanical resonators. *Optica*, 1(6):1–15, September 2014.

[70] Roger Chen, Michael Moewe, Linus C Chuang, Shanna Crankshaw, and Connie Chang-Hasnain. Whispering gallery modes in GaAs nanoneedles. In *2008 International Nano-Optoelectronics Workshop*, pages 259–260. IEEE, 2008.

[71] Sumin Choi, Cuong Ton-That, Matthew R Phillips, and Igor Aharonovich. Observation of whispering gallery modes from hexagonal ZnO microdisks using cathodoluminescence spectroscopy. *Applied Physics Letters*, 103(17):171102, October 2013.

[72] Kun Qian, Jun Tang, Hao Guo, Wenyao Liu, Jun Liu 0005, Chenyang Xue, Yongqiu Zheng, and Chengfei Zhang. Under-Coupling Whispering Gallery Mode Resonator Applied to Resonant Micro-Optic Gyroscope. *Sensors*, 17(1):100, 2017.

[73] Yangcheng Li, Farzaneh Abolmaali, Kenneth W Allen, Nicholaos I Limberopoulos, Augustine Urbas, Yury Rakovich, Alexey V Maslov, and Vasily N Astratov. Whispering gallery mode hybridization in photonic molecules. *Laser & Photonics Reviews*, 11(2):1600278, March 2017.

[74] Xuhui Zhang and Hoi Wai Choi. GaN Nano-Cones Prepared by Jet-Printed Nanospheres Arrays. *IEEE Transactions on Nanotechnology*, 15(3):423–427, 2016.

[75] K H Li, Zetao Ma, and H W Choi. High-Q whispering-gallery mode lasing from nanosphere-patterned GaN nanoring arrays. *Applied Physics Letters*, 98(7):071106, February 2011.

[76] L Maleki and A B Matsko. Lithium Niobate Whispering Gallery Resonators: Applications and Fundamental Studies. In *Ferroelectric Crystals for Photonic Applications*, pages 337–383. Springer Berlin Heidelberg, Berlin, Heidelberg, 2009.

[77] B Sprenger, H G L Schwefel, Z H Lu, S Svitlov, and L J Wang. CaF2 Whispering-Gallery-Mode Resonator Stabilized Narrow Linewidth Laser. *Optics Letters*, 35(17):2870–2872, August 2012.

[78] Lan Yang, Tal Carmon, Bumki Min, Sean M Spillane, and Kerry J Vahala. Erbium-doped and Raman microlasers on a silicon chip fabricated by the sol–gel process. *Applied Physics Letters*, 86(9):091114, February 2005.

[79] T J Kippenberg, S M Spillane, D K Armani, and K J Vahala. Ultralow-threshold microcavity Raman laser on a microelectronic chip. *Optics Letters*, 29(11):1224–1226, 2004.

[80] Lan Yang, D K Armani, and K J Vahala. Fiber-coupled erbium microlasers on a chip. *Applied Physics Letters*, 83(5):825–826, August 2003.

[81] Tao Lu, Lan Yang, Rob V A van Loon, Albert Polman, and Kerry J Vahala. On-chip green silica upconversion microlaser. *Optics Letters*, 34(4):482, 2009.

[82] Jan Niehusmann, Andreas Vörckel, Peter Haring Bolivar, Thorsten Wahlbrink, Wolfgang Henschel, and Heinrich Kurz. Ultrahigh-quality-factor silicon-on-insulator microring resonator. *Optics Letters*, 29(24):2861, 2004.

[83] R Soref and B Bennett. Electrooptical effects in silicon. *IEEE Journal of Quantum Electronics*, 23(1):123–129, January 1987.

[84] W Bogaerts, R Beats, P Dumon, V Wiaux, D Beckx, D Taillaert, and B Luyssaert. Nanophotonic waveguides in silicon-on-insulator fabricated with CMOS technology. *Lightwave Technology, Journal of*, 23(1):401–412, 2005.

[85] Qianfan Xu, David Fattal, and Raymond G Beausoleil. Silicon microring resonators with 1.5-μm radius. *Optics express*, 16(6):4309–4315, 2008.

[86] Kevin K Lee, Desmond R Lim, Lionel C Kimerling, Jangho Shin, and Franco Cerrina. Fabrication of ultralow-loss Si/SiO2 waveguides by roughness reduction. *Optics Letters*, 26(23):1888–1890, 2001.

[87] Thomas Michels, Ivo W Rangelow, and Vladimir Aksyuk. Fabrication Process for an Optomechanical Transducer Platform with Integrated Actuation. *Journal of Research of the National Institute of Standards and Technology*, 121:1–30, December 2016.

[88] Quirin P Unterreithmeier, Eva M Weig, and Jörg P Kotthaus. Universal transduction scheme for nanomechanical systems based on dielectric forces. *Nature*, 458(7241):1001–1004, April 2009.

[89] T Faust, J Rieger, M J Seitner, P Krenn, J P Kotthaus, and E M Weig. Nonadiabatic Dynamics of Two Strongly Coupled Nanomechanical Resonator Modes. *Physical Review Letters*, 109(4):1–4, July 2012.

[90] T G Tiecke, K P Nayak, J D Thompson, T Peyronel, N P de Leon, V Vuletic, and M D Lukin. Efficient fiber-optical interface for nanophotonic devices. *Optica*, 2(2):1–6, January 2015.

[91] *GRIN Lens Assemblies revision*, December 2013.

[92] O Mitomi, K Kasaya, and H Miyazawa. Design of a single-mode tapered waveguide for low-loss chip-to-fiber coupling. *IEEE Journal of Quantum Electronics*, 30(8):1787–1793, 1994.

[93] V R Almeida, R R Panepucci, and M Lipson. Nanotaper for compact mode conversion. *Optical Letters*, 28(15):1–3, June 2003.

[94] Sharee McNab, Nikolaj Moll, and Yurii Vlasov. Ultra-low loss photonic integrated circuit with membrane-type photonic crystal waveguides. *Optics express*, 11(22):2927, 2003.

[95] Long Chen, Christopher R Doerr, Young-Kai Chen, and Tsung-Yang Liow. Low-Loss and Broadband Cantilever Couplers Between Standard Cleaved Fibers and High-Index-Contrast Si_3N_4 or Si Waveguides. *Photonics Technology Letters, IEEE*, 22(23):1744–1746, 2010.

[96] I Moerman, P P Van Daele, and P M Demeester. A review on fabrication technologies for the monolithic integration of tapers with III-V smiconductor devices. *IEEE Journal of Selected Topics in Quantum Electronics*, 6, 1997.

[97] T Shoji, T Tsuchizawa, K Yamada, and H Morta. Low loss mode size converter from 0.3 pm square Si wire waveguide to single mode fiberes. *Electronics Letters*, 38(25):1–2, February 2004.

[98] T W Trask and D J Albares. Optical Fiber to Waveguide Coupling Technique. *Technical Report*, 1(1337):1–15, August 1990.

[99] T Michels and V Aksyuk. Cavity Optical Transducer Platform with Integrated Actuation for Multiple Sensing Applications . In *Hilton Head 2016 Workshop*, pages 1–5, April 2016.

[100] Huan Li, Yu Chen, Jong Noh, Semere Tadesse, and Mo Li. Multichannel cavity optomechanics for all-optical amplification of radio frequency signals. *Nature Communications*, 3:1091–6, 2012.

[101] J Zou, H Miao, T Michels, and V Aksyuk. *Nanotechnology 2013: Electronics, Devices, Fabrication, MEMS, Fluidcs and Computational (Volume 2)*. MEMS & NEMS Devices & Applications: A Novel Integrated Optomechanical Transducer and Its Application in Atomic Force Microscopy. crpress, 2013.

[102] J A Marohn. *The minimum detectable force concept*. Kavli Institute at Cornell Summer School in MRFM, 2006.

[103] Yuxiang Liu, Houxun Miao, Vladimir Aksyuk, and Kartik Srinivasan. Wide cantilever stiffness range cavity optomechanical sensors for atomic force microscopy. *Optics express*, 20(16):18268–, July 2012.

[104] V B Braginsky, Yu I Vorontsov, and K S Thorne. QUANTUM NONDEMOLITION MEASUREMENTS. *Science*, 209(4456):547–557, 1980.

[105] J Suh, A J Weinstein, C U Lei, E E Wollman, S K Steinke, P Meystre, A A Clerk, and K C Schwab. Mechanically detecting and avoiding the quantum fluctuations of a microwave field. *Science*, 344(6189):1262–1265, June 2014.

[106] J D Teufel, T Donner, M A Castellanos-Beltran, J W Harlow, and K W Lehnert. Nanomechanical motion measured with an imprecision below that at the standard quantum limit. *Nature Nanotechnology*, 4(1):820–823, December 2009.

[107] Jie Zou, Marcelo Davanço, Yuxiang Liu, Thomas Michels, Kartik Srinivasan, and Vladimir Aksyuk. Integrated silicon optomechanical transducers and their application in atomic force microscopy. *arXiv.org*, May 2014.

[108] M. T. Rakher M. Davanco K. Srinivasan, H. Miao and V. Aksyuk. Optomechanical transduction of an integrated silicon cantilever probe using a microdisk resonator. *Nano Letters*, Volume 11, 2011.

[109] J G Huang, B Dong, M Tang, Y D Gu, H G Wu, Z C Yang, and Y F Jin. All optomechanical modulation in photonic circuites. *Transducers*, pages 1–4, March 2015.

[110] G Binnig and C F Quate. Atomic force microscope. *Applied Physics Letters*, 56(1):1–5, August 2010.

[111] Thomas Michels, Elshad Guliyev, Michal Klukowski, and Ivo W Rangelow. Micromachined self-actuated piezoresistive cantilever for high speed SPM. *Microelectronic Engineering*, 97(C):265–268, September 2012.

[112] Ivo W Rangelow. Scanning proximity probes for nanoscience and nanofabrication. *Microelectronic Engineering*, 83(4-9):1449–1455, April 2006.

[113] Franz Giessibl. Advances in atomic force microscopy. *Reviews of Modern Physics*, 75(3):949–983, July 2003.

[114] Ahmad Ahmad, Tzvetan Ivanov, Tihomir Angelov, and Ivo W Rangelow. Fast atomic force microscopy with self-transduced, self-sensing cantilever. *Journal of Micro/Nanolithography, MEMS, and MOEMS*, 14(3):031209, July 2015.

[115] Ahmad Ahmad, Tzvetan Ivanov, Alexander Reum, Elshad Guliyev, Tihomir Angelov, Andreas Schuh, Marcus Kaestner, Ivaylo Atanasov, Manuel Hofer, Mathias Holz, and Ivo W Rangelow. Self-actuated, self-sensing cantilever for fast CD measurement. In Jason P Cain and Martha I Sanchez, editors, *SPIE Advanced Lithography*. SPIE, March 2015.

[116] Steve Olson, Bruce Altemus, Balasubramanian Sankaran, Natalya Tokranova, Robert Geer, James Castracane, and Bai Xu. Fabrication of cantilever probes with integrated piezoresistive read-out and built-in piezoelectric actuators. In Albert K Henning, editor, *MOEMS-MEMS Micro & Nanofabrication*, pages 167–175. SPIE, January 2005.

[117] Manuel Hofer, Tzvetan Ivanov, Maciej Rudek, Daniel Kopiec, Elshad Guliyev, Teodor P Gotszalk, and Ivo W Rangelow. Fabrication of self-actuated piezoresistive thermal probes. *Microelectronic Engineering*, 145:32–37, September 2015.

[118] Tihomir Angelov, Ahmad Ahmad, Elshad Guliyev, Alexander Reum, Ivaylo Atanasov, Tzvetan Ivanov, Valentyn Ishchuk, Marcus Kaestner, Yana Krivoshapkina, Steve Lenk, Claudia Lenk, Ivo W Rangelow, Mathias Holz, and Nikolay Nikolov. Six-axis AFM in SEM with self-sensing and self-transduced cantilever for high speed analysis

and nanolithography. *Journal of Vacuum Science & Technology B*, 34(6):06KB01, November 2016.

[119] Y Sarov, A Frank, Tzv Ivanov, J P Zöllner, K Ivanova, B Volland, I W Rangelow, A Brogan, R Wilson, P Zawierucha, M Zielony, T Gotszalk, N Nikolov, M Zier, B Schmidt, and I Kostic. Parallel proximal probe arrays with vertical interconnections. *Journal of Vacuum Science & Technology B: Microelectronics and Nanometer Structures*, 27(6):3132, 2009.

[120] Ahmad Ahmad, Nikolay Nikolov, Tihomir Angelov, Tzvetan Ivanov, Alexander Reum, Ivaylo Atanasov, Elshad Guliyev, Valentyn Ishchuk, Marcus Kaestner, Yana Krivoshapkina, Steve Lenk, Claudia Lenk, Ivo W Rangelow, and Mathias Holz. Large area fast-AFM scanning with active "Quattro" cantilever arrays. *Journal of Vacuum Science & Technology B*, 34(6):1, November 2016.

[121] Ivo W Rangelow, Tzvetan Ivanov, Burkhard E Volland, Denis Dontsov, Yanko Sarov, Katerina Ivanova, Arun Persaud, Denis Filenko, Nikolaj Nikolov, Michael Zier, Bernd Schmidt, Teodor Gotszalk, and Thomas Sulzback. Raster-Sonden-Mikroskopie mit Cantilever-Arrays (Scanning Probe Microscopy with Cantilever Arrays). *tm – Technisches Messen*, 73(9), September 2009.

[122] T Itoh, T Ohashi, and T Suga. Piezoelectric cantilever array for multiprobe scanning force microscopy . *IEEE, Journal of Microelectromechanical Systems*, 5(2):1–5, March 2004.

[123] I W Rangelow, Tzv Ivanov, K Ivanova, B E Volland, P Grabiec, Y Sarov, A Persaud, T Gotszalk, P Zawierucha, M Zielony, D Dontzov, B Schmidt, M Zier, N Nikolov, I Kostic, W Engl, T Sulzbach, J Mielczarski, S Kolb, Du P Latimier, R Pedreau, V Djakov, S E Huq, K Edinger, O Fortagne, A Almansa, and H O Blom. Piezoresistive and self-actuated 128-cantilever arrays for nanotechnology applications. *Microelectronic Engineering*, 84(5-8):1260–1264, May 2007.

[124] I W Rangelow, G Bischoff, J Mueller, Y Sarov, A Frank, J P Zoellner, K H Druee, and T Ivanov. Packaging von selbstaktuierten piezoresistiven Cantilever-Arrays. *Microelectronic Engineering*, pages 1–2, March 2009.

[125] H M Gibbs. *Optical Bistability: Controlling Light With Light*. Published by Academic Pr, 1985.

[126] Paul E Barclay, Kartik Srinivasan, and Oskar Painter. Nonlinear response of silicon photonic crystal microresonators excited via an integrated waveguide and fiber taper. *Optics express*, 13(3):801–, February 2005.

[127] M Borselli, T J Johnson, and Oskar Painter. Beyond the Rayleigh scattering limit in high-Q silicon microdisk: theory and experiment. *Optical Express*, 34:1–16, February 2005.

[128] G Cocorullo and I Rendina. Thermo-optical modulation at 1.5 μm in silicon etalon . *Electronics Letters*, 28(1), January 1992.

[129] D Sarid. High efficiency input-output prism waveguide coupler: an analysis. *Applied Optics*, 18(17):1–6, March 2003.

[130] S Spillane, T J Kippenberg, O J Painter, and K J Vahala. Ideality in a Fiber-Taper-Coupled Microresonator System for Application to Cavity Quantum Electrodynamics. *Physical Review Letters*, 91(4):1–4, July 2003.

[131] C P Michael, M Borselli, T J Johnson, C Chrystal, and O Painter. An optical fiber-taper probe for wafer-scale microphotonic device characterization. *Optics express*, 15:1–8, April 2007.

[132] B Cappella and G Dietler. *Force-distance curves by atomic force microscopy*. Elsevier, May 2003.

[133] S A Zotov, B R Simon, A A Trusov, and A M Shkel. High Quality Factor Resonant MEMS Accelerometer with Continuous Thermal Compensation . *IEEE Sensors*, 15(9), 2015.

[134] B R Ilic, H G Craighead, S Krylov, W Senaratne, C Ober, and P Neuzil. Attogram detection using nanoelectromechanical oscillators . *Journal of Applied Physics*, 95(7), 2004.

[135] J Atalaya, A Isacsson, and M I Dykman. Diffusion-induced dephasing in nanomechanical resonators. *Physical Review B*, 10(045419):1–9, 2011.

[136] J Moser, J Güttinger, A Eichler, J Esplandiu, D E Liu, M I Dykman, and A Bachtold. Ultrasensitive force detection with a nanotube mechanical resonator. *Nature Nanotechnology*, 8:493–496, 2013.

[137] V Gouttenoire, T Barois, S Perisanu, J L Leclersq, S T Purcell, P Vincent, and A Ayari. Digital and FM demodulation of a doubly clamped single-walled carbon-nanotube oscillator: towards a nanotube cell phone. *Small*, 6:1060–1065, 2010.

[138] E Mile, G Jourdan, I Bargatin, S Labarthe, C Marcoux, P Andreucci, S Hentz, C Kharrat, E Colinet, and L Duraffoug. In-plane nanoelectromechanical resonators based on silicon nanowire piezoresistive detection . *Nanotechnology*, 21(165504), 2010.

[139] M I Dykman, M Khasin, J Portman, and S W Shaw. Spectrum of an Oscillator with Jumping Frequency and the Interference of Partial Susceptibilities. *Physical Review Letters*, 105(230601), 2010.

[140] J R Vig and Y Kim. Noise in Microelectromechanical System Resonators. *IEEE Trans. Ultrason. Ferroelectr. Freq. Control*, 46:1558–1565, 1999.

[141] A N Cleland and M L Roukes. Noise processes in nanomechanical resonators. *Journal of Applied Physics*, 92(5):2758–2769, September 2002.

[142] Y T Yang, C Callegari, X L FEng, and M L Roukes. Surface adsorbate fluctuations and noise in nanoelectromechanical systems. *Nano Letters*, 11:1753–1759, 2011.

[143] K Y Fong, W H P Pernice, and H X Tang. Frequency and phase noise of ultrahigh Q silicon nitride nanomechanical resonators. *Physical Review B*, 85(161410), 2012.

[144] Benjamin S Sheard, Malcolm B Gray, Conor M Mow-Lowry, David E McClelland, and Stanley E Whitcomb. Observation and characterization of an optical spring. *Physical Review A*, 69(5):051801, May 2004.

[145] Feng Tian, Guangya Zhou, Yu Du, Fook Siong Chau, and Jie Deng. Optical spring effect in nanoelectromechanical systems. *Applied Physics Letters*, 105(6):061115–5, August 2014.

[146] M Hossein-Zadeh and K J Vahala. Observation of optical spring effect in a microtoroidal optomechanical resonator. *Optics Letters*, 32(12):1–3, June 2007.

[147] Thomas Corbitt, Yanbei Chen, Farid Khalili, David Ottaway, Sergey Vyatchanin, Stan Whitcomb, and Nergis Mavalvala. Squeezed-state source using radiation-pressure-induced rigidity. *Physical Review A*, 73(2):282, February 2006.

[148] S Gigan, H R Böhm, M Paternostro, F Blaser, G Langer, J B Hertzberg, K C Schwab, D Bäuerle, M Aspelmeyer, and A Zeilinger. Self-cooling of a micromirror by radiation pressure. *Nature*, 444(7115):67–70, November 2006.

[149] D B Sullivan, D W Allan, D A Howe, and F L Walls. Characterization of Clocks and Oscillators. NIST Technical Note, 1990.

[150] G Krishnan, C U Kshirsagar, G K Ananthasuresh, and N Bhat. Micromachined High-Resolution Accelerometers. *Journal of the Inadian Institute of Science*, 87:1–29, October 2007.

[151] Cenk Acar and Andrei M Shkel. Experimental evaluation and comparative analysis of commercial variable-capacitance MEMS accelerometers. *Journal of Micromechanics and Microengineering*, 13(5):634–645, May 2003.

[152] U Krishnamoorthy, R H Olsson III, G R Bogart, M S Baker, D W Carr, T P Swiler, and P J Clews. In-plane MEMS-based nano-g accelerometer with sub-wavelength optical resonant sensor. *Sensors and Actuators A: Physical*, 145-146:283–290, July 2008.

[153] Kazem Zandi, Brian Wong, Jing Zou, Roman V Kruzelecky, Wes Jamroz, and Yves-Alain Peter. In-plane silicon-on-insulator optical MEMS accelerometer using waveguide fabry-perot microcavity with silicon/air bragg mirrors. In *2010 IEEE 23rd International Conference on Micro Electro Mechanical Systems (MEMS)*, pages 839–842. IEEE, 2010.

[154] W Noell, P A Clerc, L Dellmann, B Guldimann, H P Herzig, O Manzardo, C R Marxer, K J Weible, R Dandliker, and N de Rooij. Applications of

SOI-based optical MEMS. *IEEE Journal of Selected Topics in Quantum Electronics*, 8(1):148–154, 2002.

[155] T A Berkoff and A D Kersey. Experimental demonstration of a fiber Bragg grating accelerometer. *Photonics Technology Letters, IEEE*, 8(12):1677–1679, 1996.

[156] K Y Yasumura, T D Stowe, E M Chow, T Pfafman, T W Kenny, B C Stipe, and D Rugar. Quality Factors in Micron- and Submicron-Thick Cantilevers. *Journal of Microelectromechanical Systems*, 9(1):1–9, March 2000.

[157] Matt Eichenfield, Ryan Camacho, Jasper Chan, Kerry J Vahala, and Oskar Painter. A picogram- and nanometre-scale photonic-crystal optomechanical cavity (supplementtary). *Nature*, 459(7246):550–555, May 2009.

[158] V B Braginsky, A B Manukin, and William O Hamilton. Measurement of Weak Forces in Physics Experiments. *Physics Today*, 31(2):51–52, February 1978.

[159] Alexander G Krause, Martin Winger, Tim D Blasius, Qiang Lin, and Oskar Painter. A high-resolution microchip optomechanical accelerometer. *Nature Photonics*, 6:1–5, October 2012.

[160] Felipe Guzmán Cervantes, L Kumanchik, J Pratt, and J Taylor. Self-calibrating ultra-low noise, wide-bandwidth optomechanical accelerometer. *Applied Physics Letters*, 1(104), 2013.

[161] A Muller, E B Flagg, J R Lawall, and G S Solomon. Ultrahigh-finesse, low-mode-volume Fabry. *Optics Letters*, 35(13):1–3, June 2010.

[162] N Rotenberg and L Kuipers. Mapping nanoscale light fields. *Nature Photonics*, 8(12):919–926, November 2014.

[163] S Gotzinger, S Demmerer, O Benson, and V Sandoghdar. Mapping and manipulating whispering gallery modes of a microsphere resonator with a near-field probe. *Journal of Microscopy*, 202(1):117–121, April 2001.

[164] S Mujumdar, A F Koenderink, T Sünner, B C Buchler, M Kamp, A Forchel, and V Sandoghdar. Near-field imaging and frequency tuning of a high-Q photonic crystal membrane microcavity. *Optics express*, 15(25):17214–17220, 2007.

[165] J C Knight, N Dubreuil, V Sandoghdar, J Hare, V Lefèvre-Seguin, J M Raimond, and S Haroche. Mapping whispering-gallery modes in microspheres with a near-field probe. *Optics Letters*, 20(14):1515, 1995.

[166] N Yamamoto, K Araya, and F J García de Abajo. Photon emission from silver particles induced by a high-energy electron beam. *Physical Review B*, 64(20):1069, November 2001.

[167] Ernst Jan R Vesseur, René de Waele, Martin Kuttge, and Albert Polman. Direct Observation of Plasmonic Modes in Au Nanowires Using High-Resolution Cathodoluminescence Spectroscopy. *Nano Letters*, 7(9):2843–2846, September 2007.

[168] Martin Kuttge, F Javier García de Abajo, and Albert Polman. Ultrasmall Mode Volume Plasmonic Nanodisk Resonators. *Nano Letters*, 10(5):1537–1541, May 2010.

[169] Mark W Knight, Lifei Liu, Yumin Wang, Lisa Brown, Shaunak Mukherjee, Nicholas S King, Henry O Everitt, Peter Nordlander, and Naomi J Halas. Aluminum Plasmonic Nanoantennas. *Nano Letters*, 12(11):6000–6004, November 2012.

[170] Jaysen Nelayah, Mathieu Kociak, Odile Stéphan, F Javier García de Abajo, Marcel Tencé, Luc Henrard, Dario Taverna, Isabel Pastoriza-Santos, Luis M Liz-Marzán, and Christian Colliex. Mapping surface plasmons on a single metallic nanoparticle. *Nature Physics*, 3(5):348–353, April 2007.

[171] O Schmidt, M Bauer, C Wiemann, R Porath, M Scharte, O Andreyev, G Schönhense, and M Aeschlimann. Time-resolved two photon photoemission electron microscopy. *Applied Physics B*, 74(3):223–227, February 2014.

[172] M Cinchetti, A Gloskovskii, S A Nepjiko, G Schönhense, H Rochholz, and M Kreiter. Photoemission Electron Microscopy as a tool for

the investigation of optical near fields. *Physical Review Letters*, physics.optics(4):1, May 2005.

[173] Pascal Melchior, Deirdre Kilbane, Ernst Jan Vesseur, Albert Polman, and Martin Aeschlimann. Photoelectron imaging of modal interference in plasmonic whispering gallery cavities. *Optics express*, 23(25):31619, 2015.

[174] Roman Bruck, Ben Mills, Benedetto Troia, David J Thomson, Frederic Y Gardes, Youfang Hu, Goran Z Mashanovich, Vittorio M N Passaro, Graham T Reed, and Otto L Muskens. Device-level characterization of the flow of light in integrated photonic circuits using ultrafast photomodulation spectroscopy. *Nature Photonics*, 9(1):54–60, November 2014.

[175] Roman Bruck, Kevin Vynck, Philippe Lalanne, Ben Mills, David J Thomson, Goran Z Mashanovich, Graham T Reed, and Otto L Muskens. All-optical spatial light modulator for reconfigurable silicon photonic circuits. *Optica*, 3(4):396, 2016.

[176] F J García de Abajo. Optical excitations in electron microscopy. *Review of modern physics*, 1(1):209–275, March 2009.

[177] Thomas Nobis, Evgeni M Kaidashev, Andreas Rahm, Michael Lorenz, and Marius Grundmann. Whispering Gallery Modes in Nanosized Dielectric Resonators with Hexagonal Cross Section. *Physical Review Letters*, 93(10):103903, September 2004.

[178] Benjamin J M Brenny, Daryl M Beggs, Ruben E C van der Wel, L Kuipers, and Albert Polman. Near-Infrared Spectroscopic Cathodoluminescence Imaging Polarimetry on Silicon Photonic Crystal Waveguides. *ACS Photonics*, 3(11):2112–2121, November 2016.

[179] Kevin A Twedt, Jie Zou, Marcelo Davanço, Kartik Srinivasan, Jabez J McClelland, and Vladimir A Aksyuk. Imaging Nanophotonic Modes of Microresonators using a Focused Ion Beam. *Nature Photonics*, 10(1):35–39, December 2015.

[180] A A Bogdanov, I S Mukhin, N V Kryzhanovskaya, M V Maximov, Z F Sadrieva, M M Kulagina, Yu M Zadiranov, A A Lipovskii, E I Moiseev,

Yu V Kudashova, and A E Zhukov. Mode selection in InAs quantum dot microdisk lasers using focused ion beam technique. *Optics Letters*, 40(17):4022–4025, 2015.

[181] J J McClelland, A V Steele, B Knuffman, K A Twedt, A Schwarzkopf, and T M Wilson. Bright focused ion beam sources based on laser-cooled atoms. *arXiv.org*, 1(1):011302, October 2015.

[182] B Knuffman, A V Steele, J Orloff, and J J McClelland. Nanoscale focused ion beam from laser-cooled lithium atoms. *New Journal of Physics*, 13(10):103035, October 2011.

[183] Kevin A Twedt, Lei Chen, and Jabez J McClelland. Scanning ion microscopy with low energy lithium ions. *Ultramicroscopy*, 142:24–31, July 2014.

[184] E Asari, M Kitajima, K G Nakamura, and T Kawabe. Thermal relaxation of ion-irradiation damage in graphite. *Physical Review B*, 47(17):11143–11148, May 1993.

[185] Gary S Was. *Fundamentals of Radiation Materials Science*. Metals and Alloys. Springer, New York, NY, July 2016.

[186] James F Ziegler, M D Ziegler, and J P Biersack. SRIM – The stopping and range of ions in matter (2010). *Nuclear Instruments and Methods in Physics Research Section B: Beam Interactions with Materials and Atoms*, 268(11-12):1818–1823, June 2010.

[187] J E Fredrickson, C N Waddell, W G Spitzer, and G K Hubler. Effects of thermal annealing on the refractive index of amorphous silicon produced by ion implantation. *Applied Physics Letters*, 40(2):172–174, January 1982.

[188] P K Giri, V Raineri, G Franzo, and E Rimini. Mechanism of swelling in low-energy ion-irradiated silicon. *Physical Review B*, 65(1):3702, December 2001.

[189] V Raineri, S Coffa, E Szilágyi, J Gyulai, and E Rimini. He-vacancy interactions in Si and their influence on bubble formation and evolution. *Physical Review B*, 61(2):937–945, January 2000.

[190] P K Giri. Studies on the surface swelling of ion-irradiated silicon: Role of defects. *Materials Science and Engineering: B*, 121(3):238–243, August 2005.

[191] Ankur Jain and Kenneth E Goodson. Measurement of the Thermal Conductivity and Heat Capacity of Freestanding Shape Memory Thin Films Using the 3ω Method. *Journal of Heat Transfer*, 130(10):102402, 2008.

[192] J Komma, C Schwarz, G Hofmann, D Heinert, and R Nawrodt. Thermo-optic coefficient of silicon at 1550 nm and cryogenic temperatures. *Applied Physics Letters*, 101(4):041905, July 2012.

[193] Haitan Xu, Mohammad Hafezi, J Fan, J M Taylor, G F Strouse, and Zeeshan Ahmed. Ultra-sensitive chip-based photonic temperature sensor using ring resonator structures. *Optics express*, 22(3):3098–3104, 2014.

[194] Liron Stern, Alex Naiman, Gal Keinan, Noa Mazurski, Meir Grajower, and Uriel Levy. Ultra-precise optical to radio frequency based chip-scale refractive index and temperature sensor. *Optica*, 4(1):1, 2017.

[195] Lourdes Pelaz, Luis A Marqués, and Juan Barbolla. Ion-beam-induced amorphization and recrystallization in silicon. *Journal of Applied Physics*, 96(11):5947–5976, December 2004.

[196] B Knuffman, A V Steele, and J J McClelland. Cold atomic beam ion source for focused ion beam applications. *Journal of Applied Physics*, 114(4):044303, July 2013.

[197] L Vina and M Cardona. Effect of heavy doping on the optical properties and the band structure of silicon. *Physical Review B*, pages 1–13, June 1984.

[198] W Kern. The Evolutionof Silicon Wafer CleaningTechnology. *J. Electrochem. Soc.*, 137(6):1–6, August 1990.

[199] M Mohammad, K Koshelev, T Fito, D Zheng, M Stepanova, and S Dew. Study of Development Processes for ZEP-520 as a High-Resolution Positive and Negative Tone Electron Beam Lithography Resist. *Japanese Journal of Applied Physics*, pages 1–9, June 2012.

[200] L E Ocola and A Stein. Effect of cold development on improvement in electron-beam nanopatterning resolution and line roughness. *J. Vac. Sci. Technol.*, 6(24):1–6, September 2006.

[201] Deirdre L Olynick, J A Liddle, Bruce D Harteneck, Stefano Cabrini, and I W Rangelow. Nanoscale pattern transfer for Templates, NEMs, and Nano-optics. In *SPIE*, pages 1–8, February 2007.

[202] Andrew L Goodyear, Sinclair Mackenzie, Deirdre L Olynick, and Erik H Anderson. High resolution inductively coupled plasma etching of 30 nm lines and spaces in tungsten and silicon. *J. Vac. Sci. Technol.*, pages 1–5, November 2000.

[203] M Shearn, X SUn, M Henry, A Yariv, and A Scherer. Advanced Plasma Processing: Etching, Deposition, and Wafer Bonding Techniques for Semiconductor Applications. *Etching*, 12(5):1–27, June 2012.

[204] M L Wagner and R Nine. The Use of HBr in Polysilicon Etching. *Etching*, 10:1–7, July 2013.

[205] S Lis, R Dylewicz, J Mysliwiec, A Miniewicz, and S Patela. Application of flowable oxides in photonics. *Materials Science-Poland*, 26(1):1–6, May 2008.

[206] Amir H Safavi-Naeini, Simon Gröblacher, Jeff T Hill, Jasper Chan, Markus Aspelmeyer, and Oskar Painter. Squeezed light from a silicon micromechanical resonator. *Nature*, 500(7461):185–189, August 2013.

[207] K Williams, K Gupta, and M Wasilik. Etch rates for micromachining processing-part II. *IEEE, Journal of Microelectromechanical Systems*, 12(6):1–18, July 2003.

[208] H Tanaka, S Yamashita, Y Abe, M Shikida, and K Sato. Fast Wet anisotropic Etching of Si100 and 110 with a Smooth Surface in Ultra-High Temperature KOH Solutions. In *Solid State Sensors and Actuators*, pages 1–4, August 2003.

[209] M Borselli. *High-Q Microresonators as Lasing Elements for Silicon Photonics*. PhD thesis, California Institute of Technology, California Institute of Technology, September 2016.

A.0 Appendix

A.1 Mechanical Simulation - Coupling Region

Simulation results for the first four mechanical eigenfrequencies of the waveguide, to verify that the mechanical motion of the waveguide in the coupling region doesn't produce any artifacts in the mechanical spectrum read out of the transducer. Two different option have been simulated. In the first option, three bridges connect the waveguide with a silicon support structure to hold the waveguide in place. The first four eigenfrequencies are well above 10 MHz, which is much higher then the highest target frequency for the transducers. This design, however, has a silicon bridge right in the area where the waveguide is very close to the disk. This interaction area defines the optical coupling characteristics.

The second design hold the waveguide with only two bridges, which reduces the optical loss in this area of the waveguide by a factor of $\approx 2/3$. Furthermore, this option has no support bridge in the center of the coupling region, which reduces the influence of the support structure on the optical coupling behavior. The simulation results for the mechanical eigenfrequencies show the first four eigenfrequencies well above the target frequency range for the transducer.

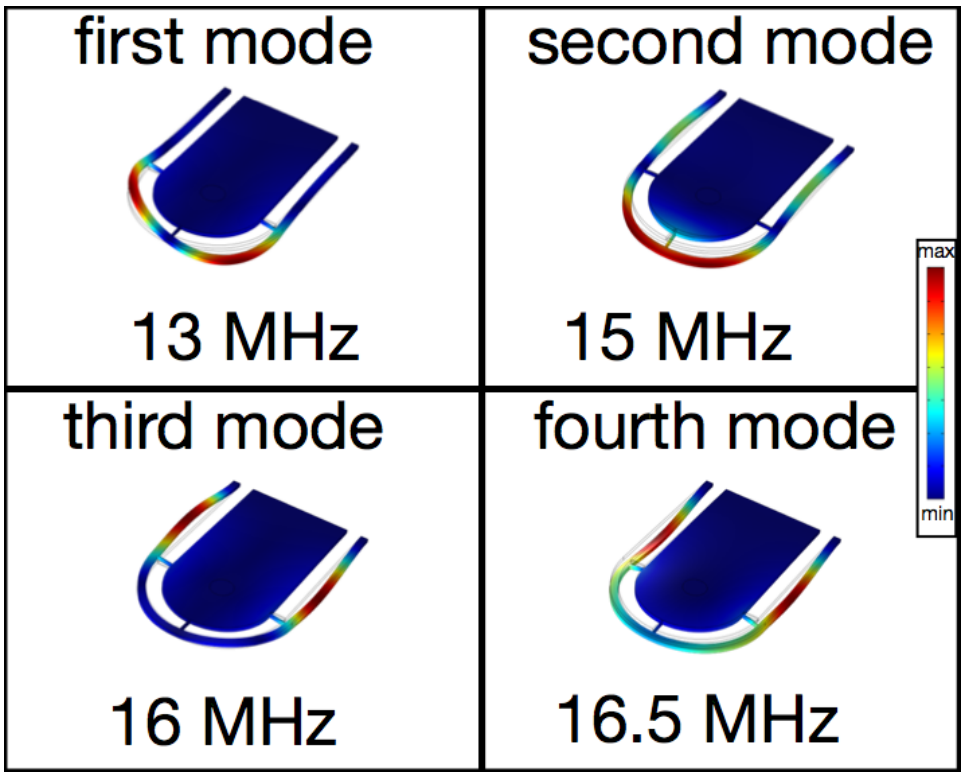

Figure A.1: *Simulation result for the mode shape of the first four mechanical eigenfrequencies for the waveguide in the coupling region for a waveguide with three support structures.*

Mode	f_{res} (Three support points)	f_{res} (Two support points)
1st	13 MHz	11 MHz
2nd	15 MHz	12.5 MHz
3rd	16 MHz	15.7 MHz
4th	16.5 MHz	23 MHz

Table A.1: *Summary of the simulation results for the eigenfrequencies for the waveguide with three or two support points.*

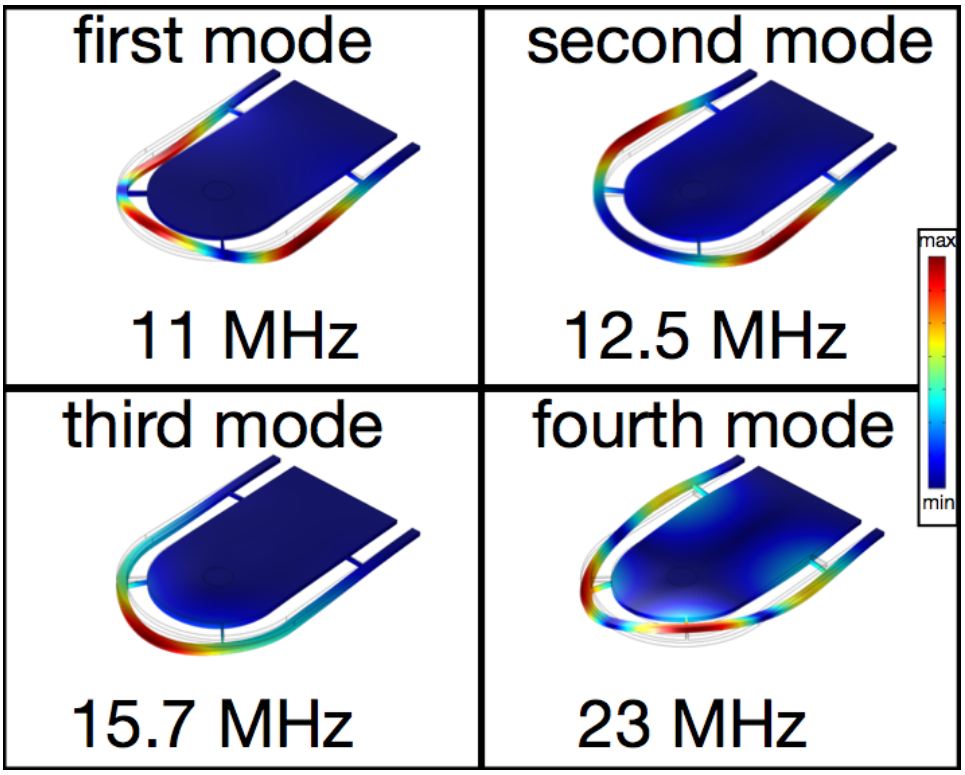

Figure A.2: *Simulation result for the mode shape of the first four mechanical eigenfrequencies for the waveguide in the coupling region for a waveguide with two support structures.*

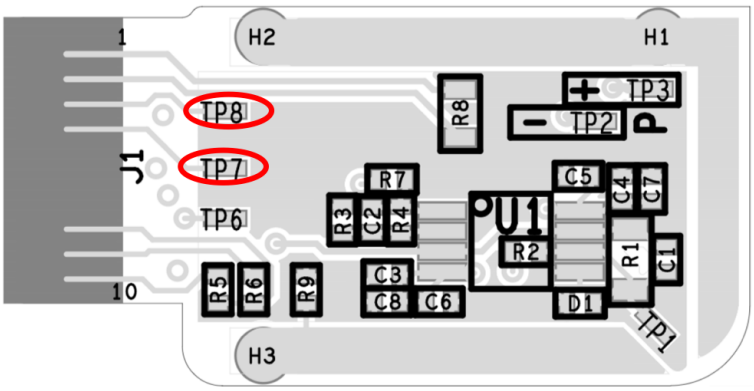

Figure A.3: *Schematic of the internal PCB of the cantilever holder. The red circle highlight the end points of the copper wires, connecting the PCB with the two contacts of the copper spring.*

A.2 Wiring Cantilever Holder

The two contact pads of the spring were connected to the contacts TP 7 and TP 8 , shown in Figure A.3 , of the integrated PCB to connect the probe chip to the internal electronics of the SPM.

B.0 Detailed fabrication process

In this section we will explain the fabrication process in detail and will provide all information to successfully reproduce the transducers.

The described fabrication process is based on a 100 mm SOI wafer. The device layer thickness of the wafer is ≈ 260 nm with low doping to insure good optical transmission [197]. The buried oxide layer has a thickness of ≈ 2 µm, which is important to prevent leakage of the optical energy in the guided mode from the photonic structure into the silicon handle wafer. The crystal orientation in the handle wafer and the device layer is ⟨100⟩ which results in the desired V-groove and cantilever chip shape after the anisotropic etching.

B.1 Backside polishing

The fabrication starts with polishing the backside of the SOI wafer for better control of the anisotropic backside etching as one of the final fabrication steps. The polishing is achieved with a table-top chemical- mechanicals-polishing (CMP) system. For the protection of the front side of the wafer during the polishing process, a combination of a silicon dioxide hard mask and a photoresist soft mask are used. The hard mask is created with a flowable oxide (i.e. FOX 16). The flowable oxide is based on an inorganic polymer in a methyl isobutyl ketone (MIBK) carrier solvent, the solvent volatilizes rapidly from the resin, leaving a planar surface. The soft mask consists of a thick photoresist mask.

B.1.0.1 Cleaning

- the wafer is cleaned with N-Methyl-2-pyrrolidone (Resist remover 1165) at ≈ 70 °C for ≈ 15 min
- followed by a rinse with isopropyl alcohol and blow dry with nitrogen gun
- alternatively, the wafer can be dried in the spin dryer, this is especially useful for batch fabrication runs with more then one wafer

B.1.0.2 Frontside protection - hard mask

- "FOX 16" diluted ≈ 1:10 with MIBK is used for the hard mask
- the FOX is applied with the following spin coater setting of ≈ 10.47 rad/s (≈ 100 rpm) for ≈ 5 s followed by ≈ 314.16 rad/s (≈ 3000 rpm) for ≈ 40 s
- the mask is cured in three consecutive soft bake steps to prevent the layer from cracking. Starting with ≈ 90 °C for ≈ 1 min, followed by ≈ 180 °C for ≈ 1 min, and ≈ 400 °C for ≈ 1 min, resulting in a cured thickness of ≈ 400 nm.

B.1.0.3 Frontside protection - soft mask

- the soft mask is created with a thick photo resist layer ("AZ 10xT") with the following spin coater parameter of ≈ 10.47 rad/s (≈ 100 rpm) for ≈ 5 s followed by ≈ 209.44 rad/s (≈ 2000 rpm) for ≈ 45 s
- the polymer layer is cured in a soft bake step of ≈ 115 °C for ≈ 10 min, resulting in a cured thickness of ≈ 12 µm.

B.1.0.4 Chemical mechanical polishing

- a slurry solution based on colloidal silica ("Ultra-Sol 556") diluted with deionized water in a ratio of ≈ 4:10 is used for the polishing process
- the process steps for the conditioning of the system are summarized below

- for the conditioning of the polishing pad, the “Conditioner" is lowered on our CMP system (“Bruker - TMT model CP-4"). The conditioning step is used to break in the polishing pad for reproducible results.

Step #1	
Time:	5 min
Force:	2.5 kg
Pump # 1:	0 ml/min (Slurry)
Pump # 2:	40 ml/min (H_2O)
Pad:	≈ 4.7 rad/s (≈ 45 rpm) (CW)
Wafer:	0 rad/s (0 rpm)
Slider:	50 mm to 70 mm (5 min^{-1})

Step #2	
Time:	5 min
Force:	2.5 kg
Pump # 1:	50 ml/min (Slurry)
Pump # 2:	0 ml/min (H_2O)
Pad:	≈ 4.7 rad/s (≈ 45 rpm) (CW)
Wafer:	0 rad/s (0 rpm)
Slider:	50 mm to 70 mm (5 min^{-1})

- after the conditioning, the “Conditioner" is raised to allow the wafer-/polishing pad contact

- the following parameters are chosen to polish the backside of the wafer down to a polished surface (This entire polishing step removes ≈ 20 µm of material on the rough wafer backside of a single-side polished wafer)

Step #1	
Time:	1 min
Wafer:	100 mm
Force:	17.236 kN/m^2
Pump # 1:	20 ml/min (Slurry)
Pump # 2:	0 ml/min (H_2O)
Pad:	≈ 3.66 rad/s (≈ 35 rpm) (CW)
Wafer:	≈ 3.14 rad/s (≈ 30 rpm) (CCW)
Slider:	50 mm to 70 mm (10 min^{-1})

Step #2	
Time:	2 h + 30 min
Wafer:	100 mm
Force:	45.642 kN/m^2
Pump # 1:	20 ml/min (Slurry)
Pump # 2:	0 ml/min (H_2O)
Pad:	$\approx$ 3.66 rad/s ($\approx$ 35 rpm) (CW)
Wafer:	$\approx$ 3.14 rad/s ($\approx$ 30 rpm) (CCW)
Slider:	50 mm to 70 mm (10 min^{-1})

Step #3	
Time:	15 min
Wafer:	100 mm
Force:	3.447 kN/m^2
Pump # 1:	0 ml/min (Slurry)
Pump # 2:	50 ml/min (H_2O)
Pad:	≈ 3.66 rad/s (≈ 35 rpm) (CW)
Wafer:	≈ 3.14 rad/s (≈ 30 rpm) (CCW)
Slider:	50 mm to 70 mm (5 min^{-1})

- it is very important that the slurry doesn't sit on the wafer for a long time after the polishing finished, because the slurry will attack the surface immediately
- to avoid an attack of the surface, the wafer is rinsed throughly with DI water right after the polishing to remove all slurry residues and dried with nitrogen.

B.1.0.5 Cleaning

- the wafer is cleaned with N-Methyl-2-pyrrolidone (Resist remover 1165) at ≈ 70 °C for ≈ 15 min
- followed by a rinse with isopropyl alcohol and deionized water DI water (DIW) dump rinse
- buffered oxide etch (16 % BOE) is used for the removal of the hard mask. This etch is performed in cycles of 30 s of etching and a DI water dump rinse until the silicon surface is hydrophobic. This step takes ≈ 1 min for the described oxide thickness.
- before the start of the patterning processes, the wafer is cleaned using the Radio Corporation of America cleaning (RCA clean) [198]. The following table lists the parameters used
- RCA Clean

RCA I	
Solution:	DIW / NH_4OH / H_2O_2 (50 ml / 10 ml / 10 ml)
Time:	≈ 10 min
Temperature:	≈ 75 °C

HF dip	
Solution:	HF / DIW (2 ml / 100 ml)
Time:	≈ 30 s
Temperature:	room temperature (RT)

RCA II	
Solution:	DIW / HCl / H_2O_2 (50 ml / 10 ml / 10 ml)
Time:	≈ 10 min
Temperature:	≈ 75 °C

- for this step, the wafer should be placed in a 100 mm cassette for the handling
- it is important to add the hydrogen peroxide only a few minutes before the cleaning, otherwise the hydrogen peroxide will be consumed by the bath before the actual cleaning. The hydrogen peroxide for RCA II should not be added earlier then ≈ 7 min before the bath is used.
- the wafers are dump rinsed between every step.
- after the last cleaning bath, the wafers are dried in the spin dryer.
- a good test during the cleaning is to check the hydrophobicity of the silicon surface after the HF dip. The surface should be hydrophobic, if this is not the case, the HF dip should be repeated.

B.1.1 Alignment marks

The following step defines alignment marks for the electron beam lithography. We use the flat of the wafer to align the wafer to the electron beam lithography layer and to the crystallographic orientation of the silicon wafer. For the alignment of the electron beam lithography, we create alignment marks with a contact mask aligner and a silicon etch on the wafer. We then use these alignment marks to actively align the lithography pattern written by the electron beam system to the crystal orientation of the wafer. The alignment marks are also used for drift check during the electron beam write, to minimize stitching between the write fields. The depth of these alignment marks is very important to create a mark with good contrast in the electron beam tool. The alignment marks are lithographically defined using an i-line stepper lithography.

B.1.1.1 Lithography

- Hexamethyldisilazane is used for the preparation of the wafer surface to improve the adhesion between resist and wafer surface
- the wafer is heated up in a vacuum furnace to ≈ 120 °C
- after a short bake-out (≈ 20 min), Hexamethyldisilazane vapor is flowed into the chamber for the deposition, followed by a couple of purge cycles to remove the Hexamethyldisilazane from the chamber prior to venting to atmosphere
- a standard positive photoresist is used for this lithography process ("S1813")
- the resist layer is applied in a spin coating process, with the following spin speed parameters of ≈ 10.47 rad/s (≈ 100 rpm) for ≈ 5 s followed by ≈ 418.88 rad/s (≈ 4000 rpm) for ≈ 45 s (final resist layer thickness ≈ 800 nm)
- the resist is soft baked at ≈ 115 °C for ≈ 1 min
- the wafer is exposed with 140 mJ/cm^2 (I-line 365 nm) at 365 nm with a focus of 0 µm, numerical aperture of 0.6, and a sigma of 0.7 in the "annular" illumination mode
- the pattern is developed in "MF 319" for ≈ 60 s followed by a DIW rinse and dried with nitrogen

B.1.1.2 Pattern transfer

- the structure is transferred with a parallel plate reactive ion etcher ("RIE Uniaxis 790")
- the silicon device layer is etched with a sulfur hexafluoride chemistry, followed by an etch based on fluorocarbon chemistry for the silicon oxide layer (the BOX layer of the SOI wafer)
- the parameters of the etch are summarized below

Si etch	
Tool:	RIE #2 (RIE Unaxis 790)
Time:	3 min
Gases:	SF_6 / CF_4
Flow rates:	≈ 6 mL/min (≈ 6 sccm) / ≈ 24 mL/min (≈ 24 sccm)
Pressure:	≈ 1 Pa (8 mTorr)
RF power:	≈ 200 W
Ref. RF power:	≈ 0 W
DC Bias:	≈ 516 V
Etch rate:	≈ 100 nm/min

SiO_2 etch	
Tool:	RIE #2 (RIE Unaxis 790)
Time:	12 min
Gases:	O_2 / CHF_3
Flow rates:	5 mL/min (5 sccm) / 45 mL/min (45 sccm)
Pressure:	6.7 Pa (50 mTorr)
RF power:	200 W
Ref. RF power:	≈ 0 W
DC Bias:	≈ 516 V
Etch rate:	≈ 35 nm/min

- the depth of the final marks have to be more then 750 nm to be clearly visible in the electron beam lithography system

B.1.1.3 Cleaning

- after the dry etch, the wafer is cleaned in a piranha solution (H_2SO_4 : H_2O_2) to remove the resist as well as the polymers which have been created during the etch process

- a piranha solution with the ratio H_2SO_4 : H_2O_2 (3:1) is used

- the wafers are placed in the fresh solution for ≈ 10 min

- followed by a dump rinse and spin dry

B.1.2 Electron beam lithography

This step defines the photonic structures in the silicon device layer. The nominal width of the final waveguide is ≈ 500 nm and the gap between the waveguide and the disk is defined to be ≈ 340 nm. The waveguide is linearly tapered down to a width of ≈ 100 nm over the distance of ≈ 50 µm at both waveguide ends for low loss coupling to optical fibers. All dimensions are positively biased by 10 nm for the electron beam lithography to take dimension change due to oxidation into account. We use the electron beam resist "ZEP 520A" with a base dose of ≈ 460 µC. The base dose is modulated to compensate proximity effects in the lithography process, which is critical for the disk/waveguide gap as well as for the waveguide taper width. Small variations in these dimensions have a significant effect on the optical device performance. The electron beam lithography is performed on a gaussian beam electron beam system (JOEL 6300-FS) with a write field of 1 mm^2. The structures are written with "floating" write fields to optimize the lithography results. "Floating" fields are primarily used to eliminate stitching in critical areas. Floating field pattern fracturing forces the field stitch boundaries to known areas, which are typically chosen to contain straight sections of a waveguide. Additionally, the layout and pattern conversion are optimized to reduce the writing time between consecutive fields containing stitched elements. This reduces any drift induced stitching errors. The resist is developed with hexyl acetate at ≈ 0 °C to improve the contrast [199, 200], followed by a transfer step for the generated pattern into the silicon device layer. We transfer the pattern with a hydrogen bromide and chlorine chemistry (HBr / Cl_2) [201, 202]. This etch was chosen as it is known to be a highly anisotropic silicon etch with good control over the sidewall angle. HBr also produces fewer defects in the surface. Alternatively, we tried a pseudo gas- chopping approach with a plasma chemistry based on octafluorocyclobutane and sulfur hexaflouride (C_4F_8 / SF_6). The paragraph (B.1.2.2) will show a quick comparison and will try to explain the decision for the HBr chemistry. The lithography step combined with the transfer into the silicon device layer is a critical step in this fabrication process, since a small deviation in the created lateral device dimension can have a significant influence on the optical performance of the devices.

B.1.2.1 Lithography

- for the electron beam lithography the resist “ZEP 520A" is used, because of its good selectivity in our silicon etch process (An alternative product is “CSAR62")
- the resist is applied with a spin coater and the following spin speeds of ≈ 10.47 rad/s (≈ 100 rpm) for ≈ 5 s followed by ≈ 366.52 rad/s (≈ 3500 rpm) for ≈ 35 s (Which results in a final layer thickness of ≈ 400 nm)
- the resist is soft baked at ≈ 180 °C for ≈ 2 min
- to minimize charging effects during the electron beam lithography, a thin charge dissipation layer based on ≈ 15 nm of aluminum is used. This thin metal layer has a negligible influence on the electron beam resolution but shows a sufficient conductivity to reduce charging of the resist. Furthermore, aluminum can be easily removed with tetramethylammonium hydroxide (TMAH) based developer after the exposure. The aluminum layer is applied via thermal evaporation (The evaporation with a source based on electron beam heating might affect the resist properties due to unwanted exposure to electron beams)
- for the exposure of the prepared wafer, a “JOEL-JBX 6300-FS" electron beam lithography tool is used, with a base dose of ≈ 460 µC
- after the exposure, the aluminum layer is removed in TMAH based developer (“MF319") for less then 1 min. Shortly after dipping the exposed sample into the developer, the exposed area will appear in the aluminum layer, before the aluminum layer starts to disappear
- the wafer is rinsed with DIW to remove residuals of the developer and dried with nitrogen
- the wafer electron beam resist is developed in hexyl acetate at ≈ 0 °C to improve the contrast (A cooling plate based on peltier elements is used to achieve a sufficient temperature control)
- the development in cold hexyl acetate takes ≈ 120 s

- the wafer is removed from the developer and dried with nitrogen immediately to remove developer residuals
- alternatively, the wafer can be rinsed with MIBK and isopropyl alcohol (IPA) before dying (However, MIBK can create cracks in “ZEP 520A" with a thickness of more than about ≈ 400 nm)

B.1.2.2 Pattern transfer

- before the pattern can be transferred into the silicon device layer, the chamber has to be conditioned for the etch chemistry. Depending on the starting conditions, this sometimes takes more time than mentioned in this recipe.
- the conditioning starts with a bare 100 mm silicon wafer, which is etched for ≈ 20 min. After the etching the wafer surface should be shiny and not dark black. The shiny surface is a good indicator that the chamber is clean and in reasonable condition. A black surface indicates the creation of black silicon on the wafer, which is an indicator that the chamber condition is not ideal.

Conditioning	
Tool:	Oxford instrument Plasma etcher (Plasmalab System 100)
Time:	≈ 20 min
Substrate:	≈ 100 mm silicon wafer
Gases:	HBr / Cl_2
Flow rates:	≈ 10 ml/min (≈ 10 sccm) / ≈ 5 ml/min (≈ 5 sccm)
ICP power:	≈ 700 W
Ref. ICP power:	≈ 6 W
RF power:	≈ 60 W
Ref. RF power:	≈ 1 W
Pressure:	≈ 2 Pa (≈ 15 mTorr)
Temperature:	≈ 20°C
Helium backing:	≈ 2.6 Pa (≈ 20 Torr)
DC Bias:	≈ 155 V

- the conditioning with the bare silicon wafer is followed by a silicon wafer with resist pattern. The exposed silicon area of this wafer is approximately the area which will be etched on the process wafer as well. The only difference is, that this is a bare silicon wafer with a resist mask created via stepper lithography, to create waveguide structures for visual inspection of the etch results.

Conditioning	
Recipe:	Oxford instrument Plasma etcher (Plasmalab System 100)
Time:	≈ 2 min 30 s
Substrate:	≈ 100 mm silicon wafer with resist mask
Gases:	HBr / Cl_2
Flow rates:	≈ 10 ml/min (≈ 10 sccm) / ≈ 5 ml/min (≈ 5 sccm)
ICP power:	≈ 700 W
Ref. ICP power:	≈ 6 W
RF power:	≈ 60 W
Ref. RF power:	≈ 1 W
Pressure:	≈ 2 Pa (≈ 15 mTorr)
Temperature:	≈ 20°C
Helium backing:	≈ 2.6 Pa (≈ 20 Torr)
DC Bias:	≈ 142 V

- the etch results are inspected in the scanning electron microscope to determine the sidewall angle, etch rate, and uniformity across the wafer. Typical sidewall angles are between ≈ 90° and ≈ 87°, the typical etch rate is ≈ 95 nm/min with a etch rate uniformity of ± 5 nm in lateral dimension. The sidewall angle can be adjusted with the process pressure. The test etch is repeated until the desired etch profile is reached.

Pattern transfer	
Recipe:	Oxford instrument Plasma etcher (Plasmalab System 100)
Time:	adjusted with results from test etch
Substrate:	≈ 100 mm SOI wafer with ZEP 520A
Gases:	HBr / Cl_2
Flow rates:	≈ 10 ml/min (≈ 10 sccm) / ≈ 5 ml/min (≈ 5 sccm)
ICP power:	≈ 700 W
Ref. ICP power:	≈ 6 W
RF power:	≈ 60 W
Ref. RF power:	≈ 1 W
Pressure:	≈ 2 Pa (≈ 15 mTorr)
Temperature:	≈ 20°C
Helium backing:	≈ 2.6 Pa (≈ 20 Torr)
DC Bias:	≈ 142 V

- the structure is over etched to create vertical sidewalls across the whole wafer und compensate for possible non uniformities in the vertical etch rate. The displayed DC Bias will change if the surface of the buried oxide layer is reached. The etch rate of the resist is ≈ 72 nm/min. An overetch into the BOX layer is acceptable as the etch rate on silicon oxide is ≈ 50 times higher than that of silicon.

Comparison of Silicon etches

Another commonly used etch chemistry for photonic structures is an ICP etch based on sulfur hexafluoride and octafluorocyclobutane [203]. In contrast to the standard gas chopping process, where these gases are used in alternating steps of “etching" (sulfur hexafluoride) and “passivation" (octafluorocyclobutane), they are used simultaneously instead to create very smooth sidewalls. However, this simultaneous etching and passivation makes the process difficult to use because of a small process window for a stable etch. The rate at which the passivation is deposited on the side wall and bottom of the trench strongly depends on the chamber conditions, i.e.

polymers build-up on the chamber walls. We were able to realize devices with similar optical quality factors with this etch chemistry. However, the process strongly depends on the etch load and the chamber conditions and therefore has to be adjusted for every sample. This makes this etch preparation very time consuming. Furthermore, this etch is very sensitive to over etching. During an over-etch, BOX layer will charge up, which creates a deflection of the ions at the bottom. These defected ions etch the sidewall passivation and create notching.

In contrast to this, an over-etch with the HBr chemistry does not create notching, because the anisotropic properties of the etch are not created by a side wall passivation [204]. The vertical side walls depend on the directional kinetic energy of the HBr radicals. The etch is based on the amporphization effect of Cl_2 and HBr on silicon.

B.1.2.3 Cleaning

- the wafer is cleaned with a combination of solvents to remove the plasma baked resist after the etching
- in the first step, a solvent based on N-Methylpyrrolidone and N-(2-Hydroxyethyl)-2-Pyrrolidone ("EKC-Remover") at $\approx 70°C$ for ≈ 10 min
- followed by a dump rinse and spin dry
- piranha solution ($H_2SO_4 : H_2O_2$) is used to remove the bulk polymer in a ratio of $H_2SO_4 : H_2O_2$ (3:1) for ≈ 10 min
- followed by a dump rinse and spin dry

B.1.3 Silicon device layer pattern

The electron beam lithography is followed by an i-line stepper lithography to define larger-area structures in the silicon device layer. This step defines a trench around the cantilever chip and removes the silicon device layer below the future cantilever structure. The stepper lithography uses a standard positive photoresist and is followed by an inductive plasma etch process to transfer the structure into the silicon. The HBr chemistry has been chosen for this step because of the high etch selectivity between silicon and silicon

dioxide. The stepper lithography and the earlier electron beam lithography overlap in certain areas to create continuous regions with removed silicon. The high etch selectivity reduces the step between the two areas, which is created in the this etch process.

B.1.3.1 Lithography

- the wafer is prepared as described in section (B.1.1.1)
- the wafer is exposed with 140 mJ/cm^2, a focus of 0 µm, a numerical aperture of 0.6, and a sigma of 0.7 in the "angular" illumination mode
- the pattern is developed in "MF 319" for ≈ 60 s followed by a DIW rinse and dried with nitrogen

B.1.3.2 Pattern transfer

- the pattern is transferred with the HBr recipe used earlier (B.1.2.2)

Pattern transfer	
Recipe:	Oxford instrument Plasma etcher (Plasmalab System 100)
Time:	adjusted with results from test etch
Substrate:	≈ 100 mm SOI wafer with resist mask
Gases:	HBr / Cl_2
Flow rates:	≈ 10 ml/min (≈ 10 sccm) / ≈ 5 ml/min (≈ 5 sccm)
ICP power:	≈ 700 W
Ref. ICP power:	≈ 6 W
RF power:	≈ 60 W
Ref. RF power:	≈ 1 W
Pressure:	≈ 2 Pa (≈ 15 mTorr)
Temperature:	≈ 20°C
Helium backing:	≈ 2.6 Pa (≈ 20 Torr)
DC Bias:	≈ 142 V

- the structure is over etched by 10 % to ensure uniform results

B.1.3.3 Cleaning

- the wafer is cleaned with piranha solution ($H_2SO_4 : H_2O_2$) to remove the bulk polymer as well as etch residuals. A ratio of $H_2SO_4 : H_2O_2$ (3:1) is used for $\approx$ 10 min.

- followed by a dump rinse and spin dry

B.1.4 Waveguide cladding and spacer layer

The waveguide cladding layer consists of silicon dioxide. The cladding is created in a thermal oxidation and a chemical vapor deposition (CVD) step where low temperature oxide (LTO) is deposited. A first thermal oxidation step is used to clean the silicon surface from any contamination, as well as defects created during the silicon etch. This clean will also remove the halogenated and amphorizied surface layer, which has been created by Cl_2 and HBr during the silicon etch. The created oxide is removed with a wet oxide etch followed by a second thermal oxidation. The second thermal oxidation creates a good interface layer between the silicon crystal and the silicon dioxide layer created by CVD. Unfortunately, the thickness of the oxide layer created by our deposition tool has a non-unformity of $\approx \pm 10$ %. To reduce the influence on the deposited layer, the deposition process is spit into three separate depositions. The wafer is turned between the depositions by $\approx 120°$. After the first LTO deposition, the layer is etched back with a silicon dioxide dry etch to prevent the creation of encapsulated cavities in the oxide due to the growth dynamics of the CVD process. The dry etch is based on a tetraflourmethane (CF_4) chemistry, because this chemistry creates fewer etch residuals. This is important to avoid any contaminations of the cladding layer. This step is followed by two LTO depositions and a high temperature anneal in a nitrogen atmosphere. The annealing process drives the hydrogen out of the layer and improves the mechanical, electrical, optical, and chemical (etch rate) properties. The N_2 atmosphere is very important to prevent a further oxidation of the silicon device layer.

B.1.4.1 Cleaning

- before the deposition of the cladding layer, the wafer is cleaned with a RCA clean. The wafer is cleaned as described in section (B.1.0.5)

B.1.4.2 Thermal oxidation

- the SOI wafer is placed with one clean bare monitor silicon wafer on each side in the furnace boat. The monitor wafers are used to determine the grown silicon dioxide thickness after the run.
- the wafers are dry oxidized at ≈ 1000 °C for ≈ 10 min, which will create an oxide thickness of ≈ 12 nm. Therefore, the original silicon surface is moved ≈ 5 nm into the silicon, since the volume of thermal oxide consists of ≈ 44 % silicon.
- the wafers are removed from the furnace and the oxide is stripped in diluted HF (≈ 2 %), followed by a dump rinse and spin dry. The wafer is etched in diluted HF until the surface is hydrophobic.
- the thermal oxidation is repeated once with the same parameters

B.1.4.3 LTO deposition

- for the CVD deposition, it is important to determine the deposition rate with a full wafer boat and only on the wafers in the center of the boat. The non-uniformity in this process between wafers can be significant. The wafers in the center are in general more uniform then wafers on the sides of the boat.
- the SOI wafer is placed in the center of the boat with one clean monitor silicon wafer on each side. The monitor wafers are used to determine the grown silicon dioxide thickness after the run.
- the deposition is performed at ≈ 400 °C for ≈ 400 nm
- the wafers are removed and etched in a parallel plate reactive ion etcher, the parameter are summarized below:

Etch back	
Tool:	RIE Unaxis 790
Depth:	≈ 200 nm
Gases:	O_2 / CF_4
Flow rates:	≈ 5 sccm / ≈ 25 sccm
Pressure:	≈ 6.7 Pa (≈ 50 mTorr)
RF power:	≈ 200 W

- after the etch back, the wafers are loaded into the CVD furnace for the next LTO deposition.
- the deposition is again performed at ≈ 400 °C for ≈ 400 nm
- the wafers are rotated to improve the uniformity of the deposition, followed by the last deposition
- the deposition is performed at ≈ 400 °C for ≈ 600 nm
- after the final deposition, the wafers should have a final silicon dioxide thickness of ≈ 1.2 µm
- to finish up the LTO deposition, the wafers are annealed at ≈ 1000 °C in a N_2 atmosphere for ≈ 1 h. The annealing process drives the hydrogen out of the layer and improves the mechanical, electrical, optical, and chemical (etch rate) properties. The N_2 atmosphere is very important to prevent a further oxidation of the silicon device layer.

B.1.4.4 An alternative approach to create the cladding

An alternative approach to create the waveguide cladding layer is FOX [205], used earlier for the polishing hard mask. The advantage of FOX is the outstanding planarization capability, which will level all topographical steps and therefore simplify the lithographies for the following fabrication steps. In addition, the processing time for FOX compared to the LTO deposition is lower and less expensive.

FOX is applied in a spin coating process and soft baked on a hot plate, followed by a rapid thermal annealing (RTA) and a 1 h annealing in a nitro-

gen atmosphere.
However, we observed problems with FOX as waveguide cladding for this process. The silicon waveguide is defined by a trench, with an aspect ratio of (1:2), on each side. In test experiments we cured the FOX layer with different temperatures and atmospheres and were able to create a planar layer without any visible defects or cracks. However, if we released test chips with trench structures in HF, we observed a much higher lateral etch rate for the oxide in the trench compared to the oxide elsewhere. To rule out any effects originating form the interface between the silicon and the oxide cladding we introduced a thin silicon dioxide layer (created with LTO) as interface layer. Figure B.1 shows the cleaved cross section of the test structure before (left) and after the HF etch (right). The red circle #1 points out that there is still LTO left in the corners of the tench, which shows that the lateral etch rate of the LTO is lower compared to the lateral etch rate of FOX in the tench. However, circle #2 shows that the lateral etch rates for both layers (LTO and FOX) are comparable outside the trench. This suggests that the high internal stress of the FOX layer in the trench has an influence on the lateral etch rate. Since no defects are visible in the optical microscope and scanning electron microscope, we assume that the stress creates nanometer size cracks along the trench which allow a significant increase of the etch rate in HF along the trench. Figure B.2 shows a top view of an etch SOI wafer with trench structure, LTO, FOX, and SiN. The difference in the etch rates is clearly visible. We can see an etch rate of 160 nm min^{-1} on the planar surface and 4800 nm min^{-1} in the trench.
Another indicator for nanometer size cracks along the trench was found in a second etch experiment with BOE. BOE is known to attack silicon dioxide, but due to a different surface tension it doesn't creep into narrow cracks. The second etch experiment shows a significantly smaller difference between the lateral etch rate in the trench and on planar surface.

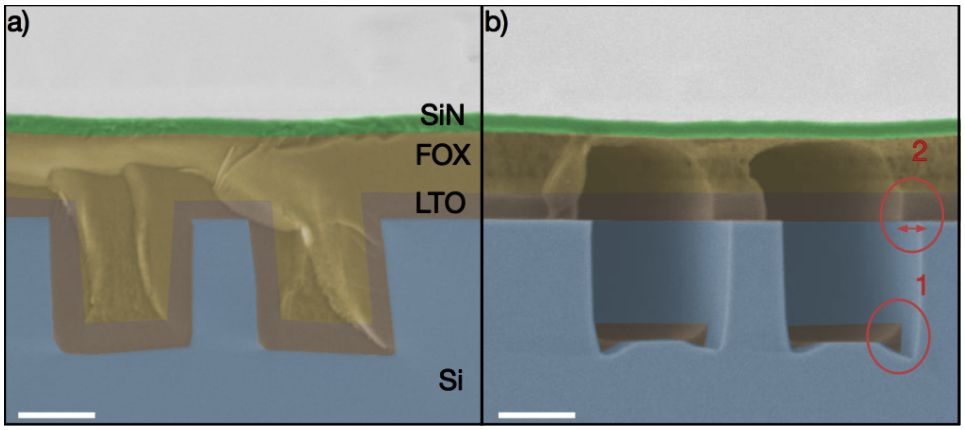

Figure B.1: *Cross sectional view of a test sample before (a) and after (b) the exposure to HF. The red circle in #1 points out that there is still LTO left in the corners of the tench, which shows that the lateral etch rate of the LTO is lower compared to the lateral etch rate of FOX in the tench. However, circle #2 shows that the lateral etch rates for both layers (LTO and FOX) are comparable outside the trench. This clearly indicates that the high internal stress of the FOX layer in the trench has an influence on the lateral etch rate. The scale bars correspond to 400 µm.*

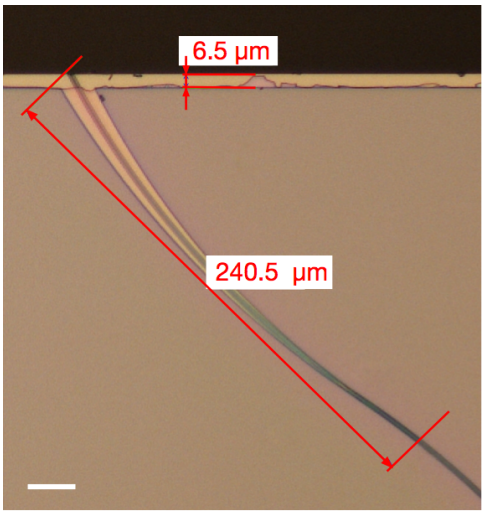

Figure B.2: *Top view of a cleaved test sample after the sample was exposed to HF for several minutes. The test sample consists of an SOI wafer structured with a waveguide. The waveguide structure is covered with a layer of LTO, FOX, and SiN. The images shows the difference between the lateral etch rate of the LTO/FOX stack on the planar surface and in the trench aside the waveguide. The scale bars correspond to 30 µm.*

B.1.5 Definition of the optomechanical coupling region and anchor point

The definition of the gap between the silicon micro disk and the mechanical member (i.e. cantilever or membrane) is important for the optical performance of the transducer. For smaller gaps the optomechanical coupling increases exponentially. However, a smaller gap also decreases the optical quality factor of the disk due to increased loss of optical energy from the disk mode into the silicon nitride structure. Simulations show that a reasonable value for the gap is ≈ 400 nm. Therefore, to reach this value the cladding layer on top of the micro disk has to be thinned down to ≈ 400 nm. Furthermore, an anchor point is created to hold the photonic structures in place after the final removal of the silicon dioxide sacrificial layer. To improve the future anchor point of the micro disk and the transition, between the area with the thick LTO cladding and a thinner LTO layer on top of the disk, a combination of dry etching and wet oxide etching is used. The dry etch creates a step profile in the oxide and the wet etch is used to round the corners of this step profile as well as undercut the silicon micro disk around the future anchor point. Figure B.3 shows these process steps in detail.

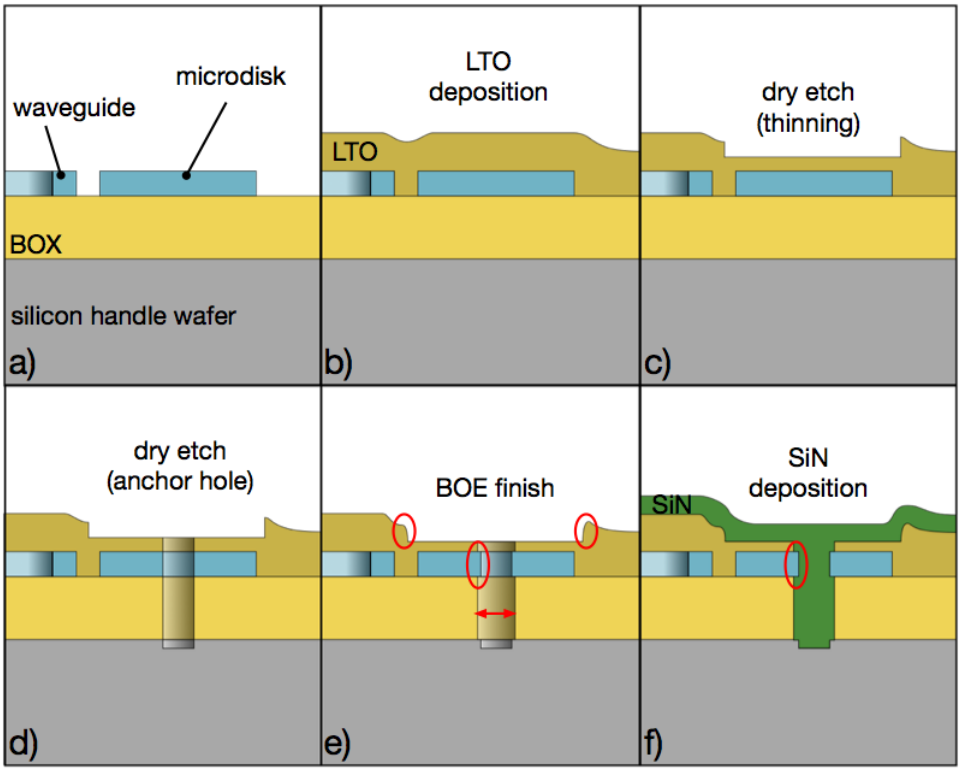

Figure B.3: *Representation of selected process steps: (a) after the transfer of the photonic structure, (b) formation of the cladding layer, (c) dry etch step of the thinning process, (d) dry etch of the anchor hole, (e) BOE finishing of the coupling region and shaping of the anchor hole, and (f) SiN deposition*

B.1.5.1 Lithography - Thinned region

- a bottom antireflective coating (ARC) is used to decouple the optical properties of the sample from the lithography process. The correct thickness of this layer is essential for its functionality. A standard ARC used for this process is "AZ BARLi-II" with a final thickness of ≈ 180 nm. This is achieved with the spin coat parameter summarized below.

- the ARC is followed by a layer of positive photo resist ("SPR 220-3").

- a resist thickness of ≈ 1.2 µm has been chosen, because it supplies enough resist for the etch processes as well as good coverage of all topographical steps. The process parameters are summarized below:

Resist	
Resist layer 1: BARLi II	
Spin speed:	≈ 10.5 rad/s (≈ 100 rpm) for ≈ 5 s / ≈ 209.4 rad/s (≈ 2000 rpm) for ≈ 40 s
Soft bake:	≈ 200°C for ≈ 60 s
Resist layer 2: SPR 220-3	
Spin speed:	≈ 10.5 rad/s (≈ 100 rpm) for ≈ 5 s / ≈ 314.2 rad/s (≈ 3000 rpm) for ≈ 40 s
Soft bake:	≈ 115°C for ≈ 90 s

- the wafer is exposed with 190 mJ/cm^2, a focus of 0.4 µm, a numerical aperture of 0.48, and a sigma of 0.5 in the "conventional" illumination mode

- the resist is treated with a post exposure bake, of ≈ 110 °C for ≈ 60 s, to improve the result of the lithography process.

- in the following, the structure is developed in "AZ 300 MIF" for ≈ 60 s followed by a DIW rinse and dried with nitrogen

B.1.5.2 Pattern transfer

- the transfer process starts with a long descum to remove the ARC at the bottom of the lithographically defined structures

- the used oxygen plasma etch only removes the organic part of the ARC; the inorganic part will be removed in the following etch based on tetraflourmethane chemistry

- the etch step with tetraflourmethane chemistry is also used to thin the oxide cladding layer in the region above the disk to a final thickness of ≈ 600 nm (Figure B.3 c))

- the process parameters are summarized in the table below, the etch is performed in a parallel pate reactive ion etcher:

Descum	
Tool:	RIE Unaxis 790
Time:	≈ 7 min
Gases:	O_2 / Ar
Flow rates:	≈ 5 ml/min (≈ 5 sccm) /≈ 20 ml/min (≈ 20 sccm)
Pressure:	≈ 4 Pa (≈ 30 mTorr)
RF power:	≈ 50 W
Ref. RF power:	≈ 0 W

SiO_2	
Depth:	until a final cladding thickness of ≈ 600 nm above the silicon disk is reached
Gases:	O_2 / CF_4
Flow rates:	≈ 5 ml/min (≈ 5 sccm) /≈ 25 ml/min (≈ 25 sccm)
Pressure:	≈ 6.7 Pa (≈ 50 mTorr)
RF power:	≈ 200 W

B.1.5.3 Cleaning

- the wafers is cleaned with a combination of solvents and acids to remove the plasma baked resist after the etching as well as the ARC

- the first step of the cleaning is a solution based on N-Methyl-2- pyrrolidone (Resist remover 1165) at ≈ 70 °C for ≈ 15 min finished with a dump rinse

- the next step is an acid clean with piranha solution (H_2SO_4 : H_2O_2). The solution is used in a ratio of H_2SO_4 : H_2O_2 (3:1) for ≈ 10 min, followed by a dump rinse

- the last step is a solvent clean to remove the inorganic residuals of the ARC. The piranha solution can only remove the organic structure of the ARC but leaves the inorganic backbone of the resist on the surface. The recommended stripper for "AZ BARLi-II" is "AZ 300T stripper", which is used at ≈ 80 °C for ≈ 10 min, followed by a dry rinse and spin dry

B.1.5.4 Lithography- Anchor holes

- this lithography defines anchor holes, which go all the way down to the silicon handle wafer, to hold the released photonic structures in place. This requires a long etch process, which requires a UV cross linked resist to improve the resist performance during the etch.

- the first layer is an ARC which improves the adhesion between resist and sample. The process parameter have been summarized in section (B.1.5.1)

- the ARC is followed by a layer of positive photo resist ("SPR 220-3").

- a resist thickness of ≈ 3.1 µm has been chosen, because it supplies enough resist for the etch processes as well as good coverage of all topographical steps. The process parameter are summarized below:

Resist layer 2: SPR-220 3	
Spin speed:	≈ 10.5 rad/s (≈ 100 rpm) for ≈ 5 s / ≈ 157 rad/s (≈ 1500 rpm) for ≈ 40 s
Soft bake:	≈ 115°C for ≈ 90 s

- the wafer is exposed with 200 mJ/cm^2, a focus of 1 µm, a numerical aperture of 0.48, and a sigma of 0.5 in the “conventional" illumination mode

- the resist is treated with a post exposure bake, of ≈ 110 °C for ≈ 60 s, to improve the result of the lithography process.

- in the following, the structure is developed in “AZ 300 MIF" for ≈ 60 s followed by a DIW rinse and dried with nitrogen

- subsequently the wafer is exposed with UV light (≈ 300 kJ/cm^2) at a temperature of ≈ 90 °C. This crosslinks the resist and lowers the etch rate in dry etch significantly.

B.1.5.5 Pattern transfer

- the transfer process starts with a descum to remove the ARC at the bottom of the lithographically defined structures

- the used oxygen plasma etch does only remove the organic part of the ARC the inorganic part will be removed in the following etch based on fluoroform (CHF_3) chemistry.

- the etch step with fluoroform chemistry is used to etch through the LTO cladding layer, the silicon device layer, the buried oxide layer, and a few nm into the silicon handle wafer (Figure B.3 (d)).

- the process parameters are summarized in the table below, the etch is performed in a parallel pate reactive ion etcher:

Descum	
Tool:	RIE Unaxis 790
Time:	≈ 7 min
Gases:	O_2 / Ar
Flow rates:	≈ 5 ml/min (≈ 5 sccm) / ≈ 20 ml/min (≈ 20 sccm)
Pressure:	≈ 4 Pa (≈ 30 mTorr)
RF power:	≈ 50 W
Ref. RF power:	≈ 0 W

SiO_2	
Depth:	until the silicon handle wafer is reached
Gases:	O_2 / CHF_3
Flow rates:	≈ 5 ml/min (≈ 5 sccm) / ≈ 45 ml/min (≈ 45 sccm)
Pressure:	≈ 6.7 Pa (≈ 50 mTorr)
RF power:	≈ 200 W
Ref. RF power:	≈ 0 W
DC Bias:	≈ 516 V
Etch rate:	≈ 35 nm/min (SiO_2) / ≈ 20 nm/min (Si)

B.1.5.6 Cleaning

- the wafers are cleaned with a combination of solvents and acids to remove the plasma baked resist after the etching as well as the ARC. Followed by an RCA clean and a BOE etch to complete the thinning process as well as the formation of the anchor holes.
- the first step of the cleaning is using a solution based on N-Methyl-2-pyrrolidone (Resist remover 1165) at ≈ 70 °C for ≈ 15 min finished with a dump rinse
- the next step is an acid clean with piranha solution (H_2SO_4 : H_2O_2). The solution is used in a ratio of H_2SO_4 : H_2O_2 (3:1) for ≈ 10 min, followed by a dump rinse
- the last step is a solvent clean to remove the inorganic residuals

of the ARC. The recommended stripper for “AZ BARLi-II" is “AZ 300T stripper", which is used at ≈ 80 °C for ≈ 10 min, followed by a dry rinse and spin dry

- subsequently an RCA clean as described earlier (B.1.0.5) is performed
- the RCA clean is followed by a wet oxide etch to complete the thinning process as well as the formation of the anchor holes. Diluted buffered hydrofluoric acid (BOE 6:1) is used for this etch, because this acid smoothes the oxide step but does not attack the interfaces between silicon and silicon dioxide, as would be attacked by diluted hydrofluoric acid.
- the sample is exposed to the diluted BOE (6:1) for ≈ 1 min and 30 s to remove ≈ 200 nm of silicon dioxide (Figure B.3(e)), followed by a dump rinse and dry.

B.1.5.7 Deposition of silicon nitride

- Low stress silicon nitride is used as the mechanical material, because it has high etch resistivity against hydrofluoric acid and potassium hydroxide.
- the final thickness of the silicon nitride layer is ≈ 400 nm with the net tensile stress of ≈ 300 MPa (Figure B.3 (f))
- the deposition is performed at ≈ 850 °C
- the wafer boat is filled with dummy wafers and one clean bare silicon wafer on both sides of the SOI wafer to aid in uniformity

B.1.6 Electrodes and wire bond pads

The metal lines and wire bond pads, to connect the cantilever chip to a printed circuit board (PCB), are created in a metal lift off process. The process is based on “Lift-off" resist in combination with a positive photoresist. Chromium and Gold (Cr/Au) are used as metals [206, 207]. The Cr functions as an adhesion layer for the Au. This combination is not attacked by the HF and KOH, and is stable to temperatures of up to 350 °C. A stack of three

resist layers is used for the “Lift-off" process. The first layer is the ARC, followed by a layer of “Lift-off" resist, and finalized by a layer of positive photo resist. “Lift-off" resist is usually based on the solvent 1-methoxy-2-propanol to avoid mixing with the positive photoresist, which is usually based on anisole as solvent. “Lift-off" resist is not photo sensitive and therefore it is non-selectively dissolved by the developer, which creates an undercut of the photoresist layer. This undercut can be tuned with the soft bake temperature and time and is very important for a clean and reproducible “lift-off" process. After the lithography process, the sample has to be treated with an descum process and a short etch based on fluoroform chemistry, to remove the ARC at the bottom of the lithographically defined structures, to expose the silicon nitride below. The short dry etch also etches into the silicon nitride which further improves the adhesion of the metal to the silicon nitride.

B.1.6.1 Lithography

- the resist stack starts with an ARC prepared with the same parameter as in section (B.1.5.1)
- the second layer consist out of the “Lift-off" resist (“LOR 3A")
- followed by a layer of positive photoresist

- all parameter for the preparation of these three layers are summarized in table below:

Resist	
Resist layer 1: Barli II	
Spin speed:	≈ 10.5 rad/s (≈ 100 rpm) for ≈ 5 s / ≈ 209.4 rad/s (≈ 2000 rpm) for ≈ 40 s
Soft bake:	≈ 200°C for ≈ 60 s
Typ. thickness:	≈ 180 nm
Resist layer 2: LOR 3A	
Spin speed:	≈ 10.5 rad/s (≈ 100 rpm) for ≈ 5 s / ≈ 314 rad/s (≈ 3000 rpm) for ≈ 40 s
Soft bake:	≈ 210°C for ≈ 20 min
Typ. thickness:	≈ 300 nm
Resist layer 3: SPR-220 3	
Spin speed:	≈ 10.5 rad/s (≈ 100 rpm) for ≈ 5 s / ≈ 314 rad/s (≈ 3000 rpm) for ≈ 40 s
Soft bake:	≈ 115°C for ≈ 90 s
Typ. thickness:	≈ 1200 nm

- the wafer is exposed with two different doses to clear the deep anchor hole and avoid overdosing the other structures
- the first exposure is for all metal lines. This exposure uses 160 mJ/cm^2, a focus of 0.2 µm, a numerical aperture of 0.48, and a sigma of 0.5 in the “conventional" illumination mode.
- the second exposure is for all anchor holes and deep trenches. This exposure uses 200 mJ/cm^2, a focus of 0.6 µm, a numerical aperture of 0.48, and a sigma of 0.5 in the “conventional" illumination mode.
- the resist is treated with a post exposure bake, of ≈ 110 °C for ≈ 60 s
- in the following, the structure is developed in “AZ 300 MIF" for ≈ 60 s followed by a DIW rinse and nitrogen dry

B.1.6.2 Descum and removal of ARC

- the transfer process starts with a descum to remove the ARC at the bottom of the lithographically defined structures.

- the etch step with fluoroform chemistry is used to remove the residual of the ARC and to etch into the first few nanometer of the silicon nitride layer for an improvement of the adhesion between the metal and the silicon nitride layer.

- the process parameters are summarized in the table below, the etch is performed in a parallel pate reactive ion etcher:

Descum	
Tool:	RIE Unaxis 790
Time:	≈ 7 min
Gases:	O_2 / Ar
Flow rates:	≈ 5 ml/min (≈ 5 sccm) / ≈ 20 ml/min (≈ 20 sccm)
Pressure:	≈ 4 Pa (≈ 30 mTorr)
RF power:	≈ 50 W
Ref. RF power:	≈ 0 W

ARC + SiN	
Time:	≈ 1 min
Gases:	O_2 / CHF_3
Flow rates:	≈ 5 ml/min (≈ 5 sccm) /≈ 45 ml/min (≈ 45 sccm)
Pressure:	≈ 6.7 Pa(≈ 50 mTorr)
RF power:	≈ 200 W
Ref. RF power:	≈ 0 W
DC Bias:	≈ 516 V
Etch rate:	≈ 35 nm/min

B.1.6.3 Metal deposition

- the metal is deposited via evaporation

- it is important for the adhesion of the metal layer to the silicon nitride that the descum is done shortly before the loading of the wafers. Furthermore, it is important that the Cr crucible is clean of any contamination.

- the Cr is deposited at a rate of 0.05 nm/s until a final thickness of 10 nm is reached

- the Au is deposited at a rate of 0.25 nm/s until a final thickness of 120 nm is reached

- the “Lift-off" process is completed by dissolving the resist mask with a solvent solution based on N-Methyl-2-pyrrolidone at ≈ 70 °C for ≈ 3 h

- the ARC is removed with piranha solution and “AZ 300T" as described in section (B.1.5.3)

B.1.7 Structuring of the mechanical member

The mechanical member of the transducer is shaped out of the silicon nitride layer. The shape is defined with a positive photoresist mask. Furthermore, the metal layer serves as a hard mask to improve the overlay error in critical regions. The lithography is based on ARC and positive photoresist. A dry etch process is used to transfer the structure into the silicon nitride layer. The etch chemistry based on fluoroform creates an etch rate of ≈ 60 nm/min for silicon nitride and ≈ 30 nm/min for the silicon dioxide layer underneath. The silicon nitride layer is over etched to ensure a good pattern transfer across all topographical steps.

B.1.7.1 Lithography

- the resist layers are prepared as described in section (B.1.5.1)
- the resist is exposed with 190 mJ/cm^2, a focus of 0.4 µm, a numerical aperture of 0.48, and a sigma of 0.5 in the "conventional" illumination mode
- the resist is treated with a post exposure bake, of ≈ 110 °C for ≈ 60 s
- in the following, the structure is developed in "AZ 300 MIF" for ≈ 60 s followed by a DIW rinse and nitrogen dry

B.1.7.2 Pattern transfer

- the pattern transfer starts with a descum step to remove the ARC at the bottom of the lithographically defined structures
- the etch step with fluoroform chemistry is used to remove the residual of the ARC and to etch through the silicon nitride layer into the silicon dioxide layer
- the process parameters are summarized in the table below, the etch is performed in a parallel pate reactive ion etcher:

Descum	
Tool:	RIE Unaxis 790
Time:	≈ 7 min
Gases:	O_2 / Ar
Flow rates:	≈ 5 ml/min (≈ 5 sccm)/ ≈ 20 ml/min (≈ 20 sccm)
Pressure:	≈ 4 Pa (≈ 30 mTorr)
RF power:	≈ 50 W
Ref. RF power:	≈ 0 W

ARC + SiN + SiO_2	
Time:	≈ 1 min
Gases:	O_2 / CHF_3
Flow rates:	≈ 5 ml/min (≈ 5 sccm)/ ≈ 45 ml/min (≈ 45 sccm)
Pressure:	≈ 6.7 Pa (≈ 50 mTorr)
RF power:	≈ 200 W
Ref. RF power:	≈ 0 W
DC Bias:	≈ 516 V
Etch rate:	≈ 60 nm/min (SiN)/ ≈ 30 nm/min (SiO_2)

B.1.7.3 Cleaning

- the sample is cleaned with piranha solution followed by "AZ 300K" as described in section (B.1.5.3)

B.1.8 Hard mask preparation for anisotropic etching

In the following step, a hafnium oxide (HfO) hard mask is deposited on the wafer to protect the frontside, specifically the exposed areas of LTO, from potassium hydroxide (KOH)[208], which is used to etch V-grooves into the frontside of the wafer and to shape the backside of the cantilever chip. The quality of the HfO layer is very important to ensure proper protection of the frontside. The etch rate of HfO in KOH depends on the carbon content of the HfO layer. The carbon content originates from the organic molecule (tetrakis(ethylmethylamino)hafnium (TEMAH)) which is used in the atomic layer deposition (ALD) process. The content of carbon in the final layer can be lowered by the use of a plasma induced deposition and with an increase purge time, as well as purge flow rates. The HfO layer is later patterned with the openings for the KOH etch on the front- and backside of the wafer. The used process for the lithography and pattern transfer is very similar for both sides. The lithography is performed in a frontside and backside contact mask aligner lithography. The pattern is transferred with a sulfur hexafluoride chemistry into the HfO layer and a fluoroform chemistry for

the transfer into the underlying SiN / SiO_2 / Si / SiO_2 until the silicon handle wafer is reached.

For the reasons of ease of process and device development the actual work has been done on chips. We are describing it as wafers, because we see no reason why this could not have been done on full wafers in principle, for a fully batch fabricated process.

B.1.8.1 Hafnium oxide deposition

- the parameters chosen for the HfO deposition are summarized in the table below. The parameters are separated into the seven steps of the ALD process (surface cleaning, deposition, TEMAH dose, TEMAH purge, gas stabilization, O_2 plasma, plasma purge). The final thickness of the ALD layer is ≈ 20 nm, which provides enough protection against KOH and can encapsulate small contaminations on the wafer surface.

Cleaning	
Recipe:	H2 surface clean
Pressure:	≈ 7.5x10^{-7} Pa
Gas:	H_2
Flow rate:	≈ 15 ml/min (≈ 15 sccm)
Time (etch):	≈ 5 min
Temperature:	≈ 300°C
Time (purge):	≈ 1 min

Deposition	
Recipe:	opt_HfO
Cycles:	200
Pressure:	≈ 7.5x10^{-7} Pa
Temperature:	≈ 300°C

TEMAH dose	
Time:	≈ 0.6 s
Gases:	Ar / TEMAH
Flow rate:	≈ 250 ml/min (≈ 250 sccm) / ≈ 1 mL/min (≈ 1 sccm)

TEMAH purge	
Time:	≈ 5 s
Gases:	Ar / O_2
Flow rate:	≈ 100 ml/min (≈ 100 sccm) / ≈ 50 mL/min (≈ 50 sccm)

opt_gas stabil	
Time:	≈ 1 s
Gases:	O_2
Flow rate:	≈ 60 ml/min (≈ 60 sccm)

O_2 plasma	
Time:	≈ 2 s
Gases:	O_2
Flow rate:	≈ 60 ml/min (≈ 60 sccm)

Plasma purge	
Time:	≈ 3 s
Gases:	Ar
Flow rate:	≈ 100 ml/min (≈ 100 sccm)

B.1.8.2 Lithography

- the wafer surface is prepared with hexamethyldiloxane as described in section (B.1.1.1)
- a thick positive photoresist is used to cover all topographical steps (“AZ 10xT")
- the resist is applied with a spin coater with a spin speed of ≈ 10.47 rad/s (≈ 100 rpm) for ≈ 5 s followed by ≈ 418.88 rad/s (≈ 4000 rpm) for ≈ 45 s to create a final resist thickness of ≈ 10 µm.
- the resist is soft baked ≈ 110 °C for ≈ 180 s
- the wafer is exposed in a mask aligner lithography with a dose of ≈ 1000 mJ/cm^2
- the pattern is developed in diluted “AZ 400K" (1:3) for ≈ 180 s followed by a DIW rinse and dried with nitrogen

B.1.8.3 Pattern transfer

- the pattern transfer starts with a sulfur hexafluoride chemistry to transfer the structure into the HfO layer

- this etch is followed by an etch based on fluoroform chemistry to transfer the structure into the underlying SiN / SiO_2 / Si / SiO_2 until the silicon handle wafer is reached

- the process parameters are summarized in the table below, the etch is performed in a parallel pate reactive ion etcher:

HfO	
Tool:	RIE Unaxis 790
Time:	≈ 5 min
Gases:	SF_6 / CF_4
Flow rates:	≈ 6 ml/min (≈ 6 sccm)/ ≈ 24 mL/min (≈ 24 sccm)
Pressure:	≈ 1 Pa (≈ 8 mTorr)
RF power:	≈ 200 W
Ref. RF power:	≈ 0 W
DC Bias:	≈ 516 V
Etch rate:	≈ 10 nm/min (HfO)

SiO_2 / SiN / Si	
Tool:	RIE Unaxis 790
Depth:	until the silicon handle wafer is exposed
Gases:	O_2 / ChF_3
Flow rates:	≈ 5 ml/min (≈ 5 sccm)/ ≈ 45 mL/min (≈ 45 sccm)
Pressure:	≈ 6.7 Pa (≈ 50 mTorr)
RF power:	≈ 200 W
Ref. RF power:	≈ 0 W
DC Bias:	≈ 516 V
Etch rate:	≈ 35 nm/min

B.1.8.4 Backside lithography and pattern transfer

The process steps described in section (B.1.8.2) and (B.1.8.3) have to be repeated on the backside of the wafer to define the openings for the backside anisotropic etching. The resist on the front side of the wafer is used as frontside protection during the backside lithography and pattern transfer process.

B.1.9 Bulk micromachining

This step defines the frontside V-grooves for the fiber attachment and it shapes the cantilever chip to make it compatible with commercial scanning probe microscopes. The anisotropic etching process is separated into two parts. In the first part, the front- and backside are etched simultaneously until the V-grooves on the front side reach the final depth of ≈ 80 µm. At this point, the wafer is placed in a etch chuck to physically protect the frontside of the wafer from the etch solution and expose only the backside of the wafer. The backside is then etched until the backside etch reaches the frontside of the wafer and the membrane around the chip changes from a red, to an orange, and then to a clear color in the transmitted light. At this point, all the silicon on the membrane is gone and only the silicon dioxide membrane is left over.

B.1.9.1 Cleaning

- the photoresist on the front- and backside of the wafer is removed with N-Methyl-2-pyrrolidone at ≈ 110 °C for ≈ 15 min
- followed by a dump rinse and spin dry

B.1.9.2 Anisotropic etching

- the wafer is etched with a 30 % solution of KOH in DIW at a temperature of ≈ 60 °C
- the beaker should be covered to avoid a change in concentration due to evaporation
- both sides are etched until the final depth of ≈ 80 µm for the frontside

V-grooves is reached

- at this point, the wafer is placed in a etch chuck to physically protect the frontside of the wafer from the etch solution and expose only the backside of the wafer
- the etch is continued at ≈ 80 °C for ≈ 16 h. Until the backside etch reaches the front side of the wafer and the membrane around the chip changes from a red, to an orange, and then to a clear color in the transmitted light. At this point, all the silicon on the membrane is gone and only the silicon dioxide membrane is left over.
- the wafer can be removed from the chuck and cleaned in warm DIW several times.
- followed by a clean in IPA and a carful drying with nitrogen

B.1.10 Release

The final release step consist out of an cleaning with HCl and DIW, followed by an HF sacrificial layer etch, which is completed with an intensive rinse with DIW. After the DIW rinse, the wafer is placed into several bathes of IPA to replace the DIW in all cavities with IPA. The wafer should stay in every bath for a couple of minutes. After all the DIW is replaced with IPA, the wafer is placed in an critical point dryer to critical point dry the released transducer. A study about the influence of the cleaning solutions and etch solutions used for the release and their influence on the optical performance of the disk has been done by Borselli [209].

B.1.10.1 Critical point drying

- the release starts with a cleaning in HCl for ≈ 10 min to remove residuals of KOH
- followed by a dump rinse cycle until a sufficient bath resistivity is reached again
- after the wafer is cleaned, the HfO protection layer and SiO_2 sacrificial layer are etched in HF (49 %) until all mechanical structures are

sufficiently undercut. The release etch for the described structure is ≈ 4 min and 30 s, which results in an undercut of ≈ 7 µm.

- the HF etch is followed by extensive dump rinse cycles to remove all HF residuals form the substrate
- in the following is the DIW replaced with IPA. This takes place in several bathes, each bath ≈ 10 min
- before the sample is placed in the critical point dryer to dry the released transducers

C.0 Summary of the Characterization Results

C.1 Probe Design # 1

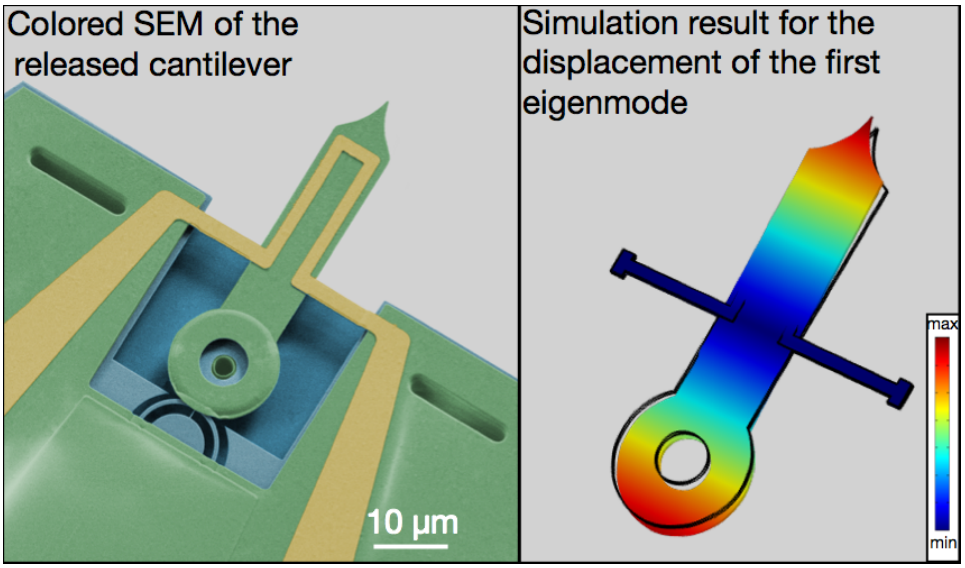

Figure C.1: *(left) Scanning electron micrograph of the released cantilever. (right) Simulation result for the displacement of the first eigenmode, to illustrate the cantilever movement.*

C.1.0.1 Mechanical spectrum

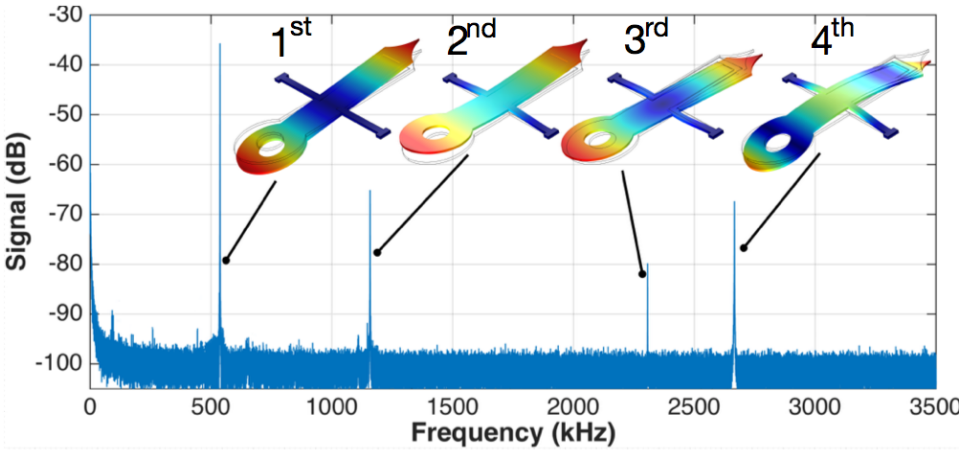

Figure C.2: *Mechanical spectrum in vacuum (blue (5 mPa)) for the cantilever layout # 1.*

Mode	f_{res}	f_{sim}	m_{eff}	k_{disk}	k_{tip}
1st	537 kHz	532 kHz	2.8*10^{-15} kg	0.05 $\frac{N}{m}$	0.03 $\frac{N}{m}$
2nd	1.16 MHz	1.21 MHz	3.25*10^{-13} kg	24 $\frac{N}{m}$	17 $\frac{N}{m}$
4th	2.66 MHz	2.69 MHz	2.88*10^{-14} kg	28 $\frac{N}{m}$	8 $\frac{N}{m}$

Mode	$\sqrt{S_{VV\ peak}}$	Q_{air}	Q_{vacuum}
1st	1.34*10^{-6} $\frac{V}{\sqrt{Hz}}$	-	2325
2nd	1.4*10^{-9} $\frac{V}{\sqrt{Hz}}$	-	2316
4th	0.9*10^{-9} $\frac{V}{\sqrt{Hz}}$	-	3245

Table C.1: *The mechanical parameter of the cantilever are summarized in this table.* $\sqrt{S_{VVpeak}}$ *has been measured with a laser power of* $\approx$ *. 10 µW at the disk coupling region.*

Mode	α_{tip}	dyn. range tip
1st	11 $\frac{fm}{\sqrt{Hz}}$	235 nm
2nd	10 $\frac{fm}{\sqrt{Hz}}$	10 nm
4th	10 $\frac{fm}{\sqrt{Hz}}$	14 nm

Table C.2: *The optical parameter related to the tip of the cantilever are summarized in this table.*

Parameter	Value
g_{OM}	33 $\pm$ 3.5 $\frac{GHz}{nm}$
β	12 $\pm$ 1.5 $\frac{V}{nm}$
α_{disk}	8.6 $\pm$ 1.7 fm
dyn. range disk	$\approx$ 8.6 nm

Table C.3: *The general optical parameter for the cantilever are summarized in this table.*

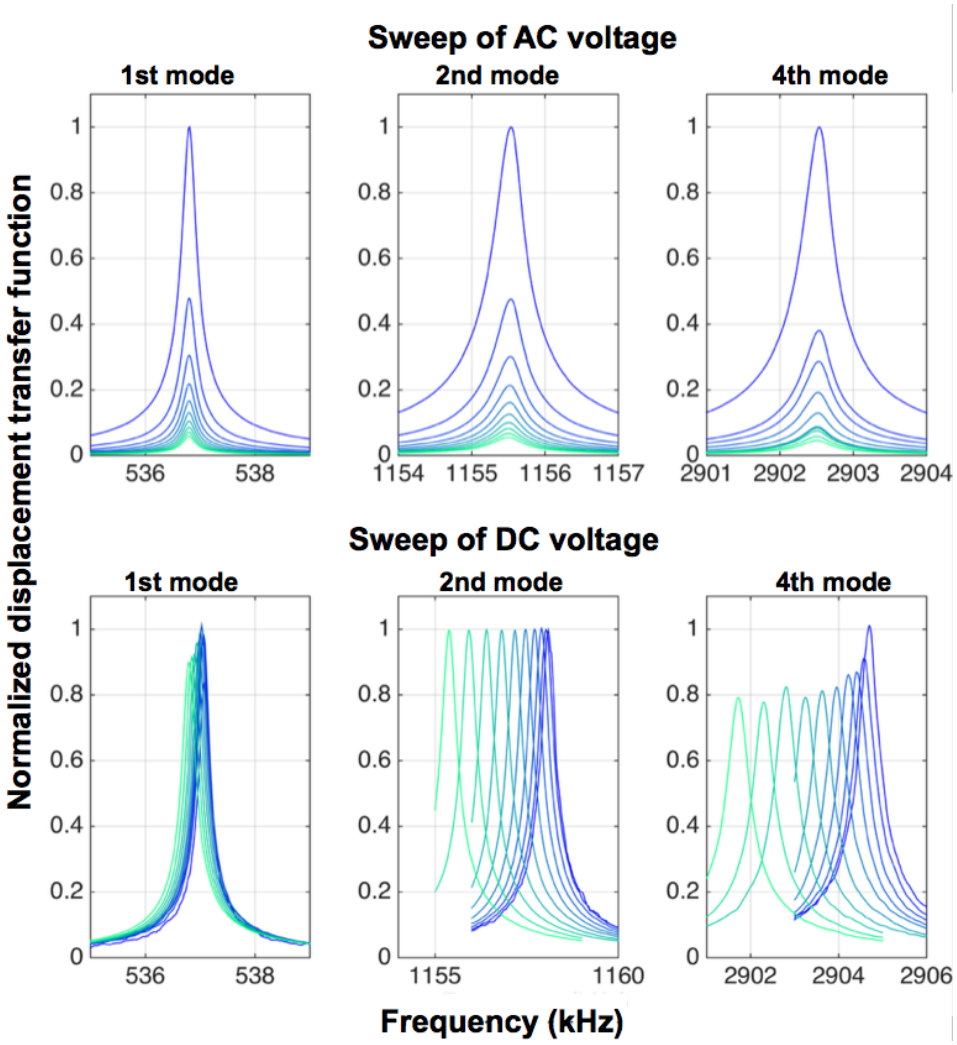

Figure C.3: *Transferfunction in air*

C.2 Probe Design # 2

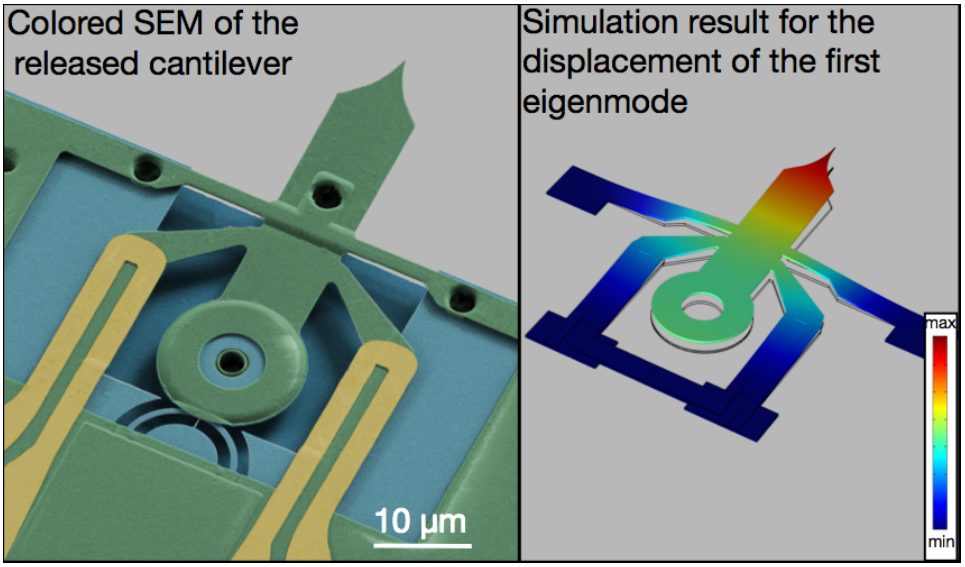

Figure C.4: *(left) Scanning electron micrograph of the released cantilever. (right) Simulation result for the displacement of the first eigenmode, to illustrate the cantilever movement.*

C.2.0.1 Mechanical spectrum

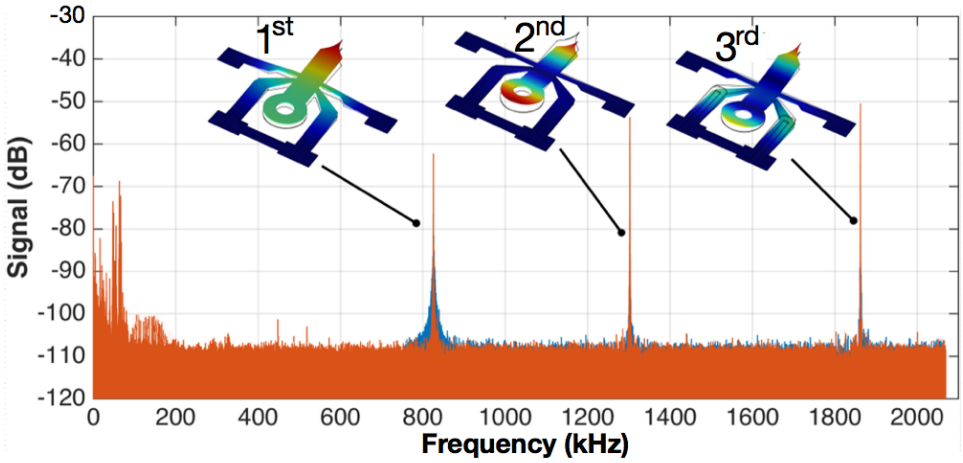

Figure C.5: *Mechanical spectrum in air (blue) and vacuum (orange (5 mPa)) for the cantilever layout # 2.*

Mode	f_{res}	f_{sim}	m_{eff}	k_{disk}	k_{tip}
1st	825 kHz	847 kHz	7.2*10^{-13} kg	36 $\frac{N}{m}$	7 $\frac{N}{m}$
2nd	1.3 MHz	1.2 MHz	2.5*10^{-14} kg	2.6 $\frac{N}{m}$	1 $\frac{N}{m}$
3rd	1.86 MHz	1.9 MHz	1.17*10^{-13} kg	351 $\frac{N}{m}$	0.6 $\frac{N}{m}$

Mode	$\sqrt{S_{VV\ peak}}$	Q_{air}	Q_{vacuum}
1st	2.7*10^{-9} $\frac{V}{\sqrt{Hz}}$	-	3200
2nd	21*10^{-9} $\frac{V}{\sqrt{Hz}}$	-	3900
3rd	45*10^{-9} $\frac{V}{\sqrt{Hz}}$	-	2500

Table C.4: *The mechanical parameter of the cantilever are summarized in this table.* $\sqrt{S_{VV\,peak}}$ *has been measured with a laser power of* $\approx .8\ \mu W$ *at the disk coupling region*

Mode	α_{tip}	dyn. range tip
1st	6.4 $\frac{fm}{\sqrt{Hz}}$	23 nm
2nd	5.4 $\frac{fm}{\sqrt{Hz}}$	6 nm
3rd	0.14 $\frac{fm}{\sqrt{Hz}}$	0.33 nm

Table C.5: *The optical parameter related to the tip of the cantilever are summarized in this table.*

Parameter	Value
g_{OM}	32 ± 3.5 $\frac{GHz}{nm}$
β	11 ± 1.3 $\frac{V}{nm}$
α_{disk}	3.2 ± 1.1 fm
dyn. range disk	≈ 8 nm

Table C.6: *The general optical parameter for the cantilever are summarized in this table.*

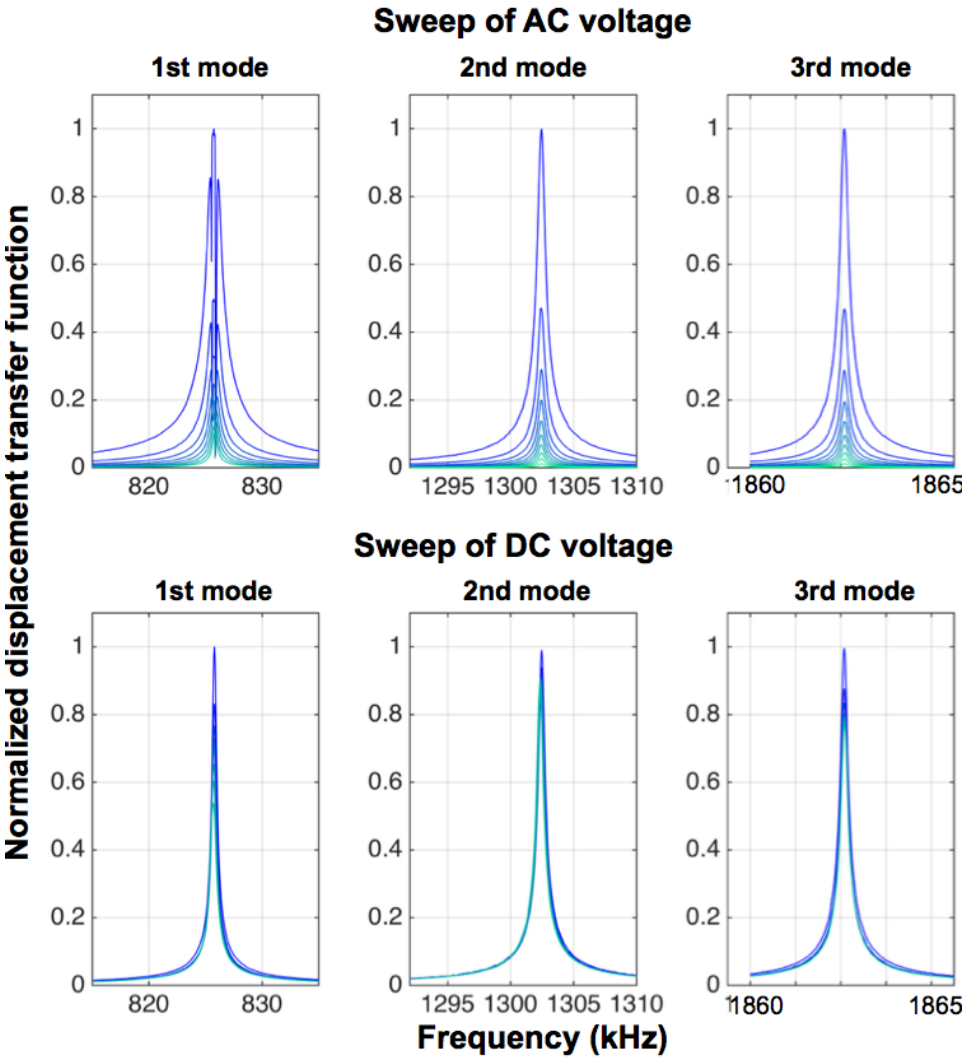

Figure C.6: *Transferfunction in air*

C.3 Probe Design # 3

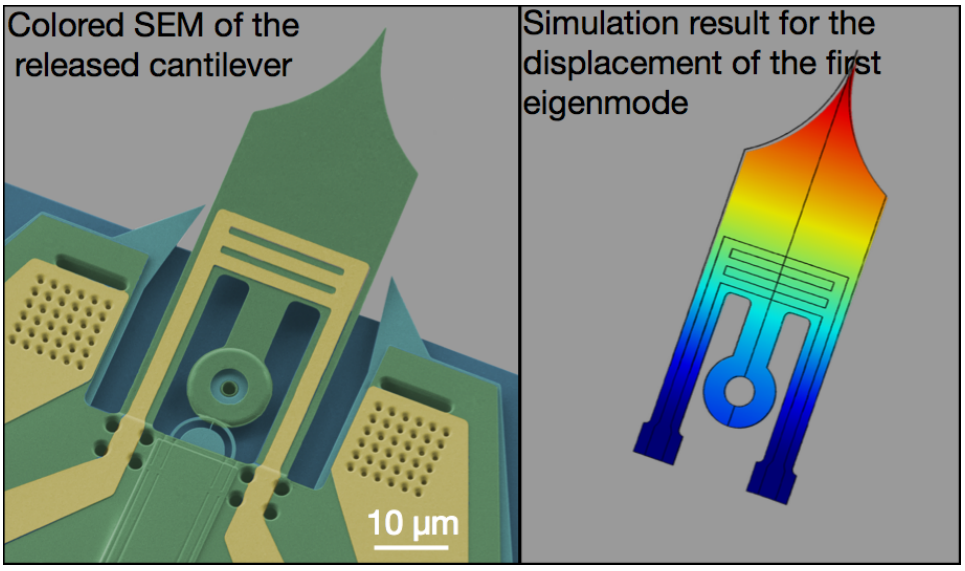

Figure C.7: *(left) Scanning electron micrograph of the released cantilever. (right) Simulation result for the displacement of the first eigenmode, to illustrate the cantilever movement.*

C.3.0.1 Mechanical spectrum

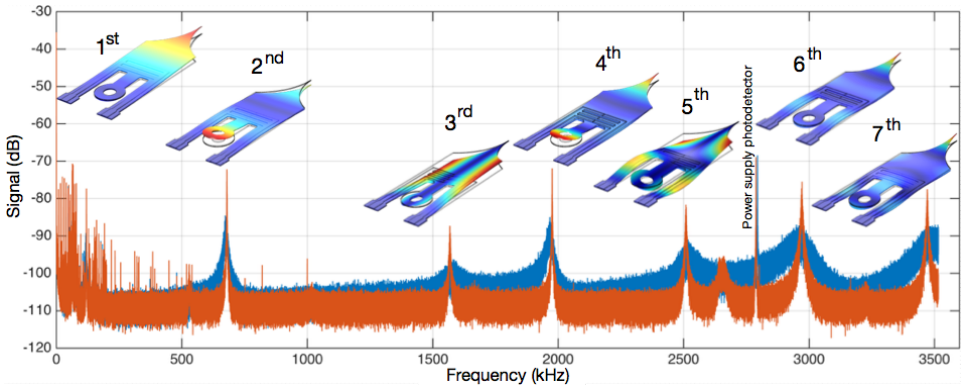

Figure C.8: *Mechanical spectrum in air (blue) and vacuum (orange / 5 mPa) for the layout # 3*

Parameter	Value
g_{OM}	$28 \pm 1.2 \frac{\text{GHz}}{\text{nm}}$
β	$11 \pm 0.8 \frac{\text{V}}{\text{nm}}$
α_{disk}	3.8 ± 0.8 fm
dyn. range disk	8 nm

Figure C.9: *The general optical parameter for the cantilever are summarized in this table.*

Mode	f_{res}	f_{sim}	m_{eff}	k_{disk}	k_{tip}
1st	119 kHz	127 kHz	4.3*10^{-14} kg	24.3 $\frac{N}{m}$	4.5 $\frac{N}{m}$
2nd	680 kHz	705 kHz	1.98*10^{-15} kg	3.5 $\frac{N}{m}$	3.8 $\frac{N}{m}$
4th	1.97 MHz	1.83 MHz	2.44*10^{-14} kg	2.6 $\frac{N}{m}$	1.7 $\frac{N}{m}$
6th	2.57 MHz	2.54 MHz	2.78*10^{-14} kg	96 $\frac{N}{m}$	0.9 $\frac{N}{m}$
7th	3.5 MHz	3.7 MHz	1.36*10^{-14} kg	39 $\frac{N}{m}$	0.8 $\frac{N}{m}$

Mode	$\sqrt{S_{VV\ peak}}$	Q_{air}	Q_{vacuum}
1st	1.8*10^{-9} $\frac{V}{\sqrt{Hz}}$	48	400
2nd	9.5*10^{-9} $\frac{V}{\sqrt{Hz}}$	113	1360
4th	1*10^{-8} $\frac{V}{\sqrt{Hz}}$	131	1975
6th	3.3*10^{-9} $\frac{V}{\sqrt{Hz}}$	42	643
7th	1.7*10^{-9} $\frac{V}{\sqrt{Hz}}$	49	1157

Table C.7: *The mechanical parameter of the cantilever are summarized in this table.* $\sqrt{S_{VV\,peak}}$ *has been measured with a laser power of* $\approx$ *10 µW at the disk coupling region*

Mode	α_{tip}	dyn. range tip
1st	8.7 $\frac{fm}{\sqrt{Hz}}$	7.6 nm
2nd	3.5 $\frac{fm}{\sqrt{Hz}}$	8.3 nm
4th	4.8 $\frac{fm}{\sqrt{Hz}}$	12 nm
6th	4.7 $\frac{fm}{\sqrt{Hz}}$	0.8 µm
7th	4.8 $\frac{fm}{\sqrt{Hz}}$	380 nm

Table C.8: *The optical parameter related to the tip of the cantilever are summarized in this table.*

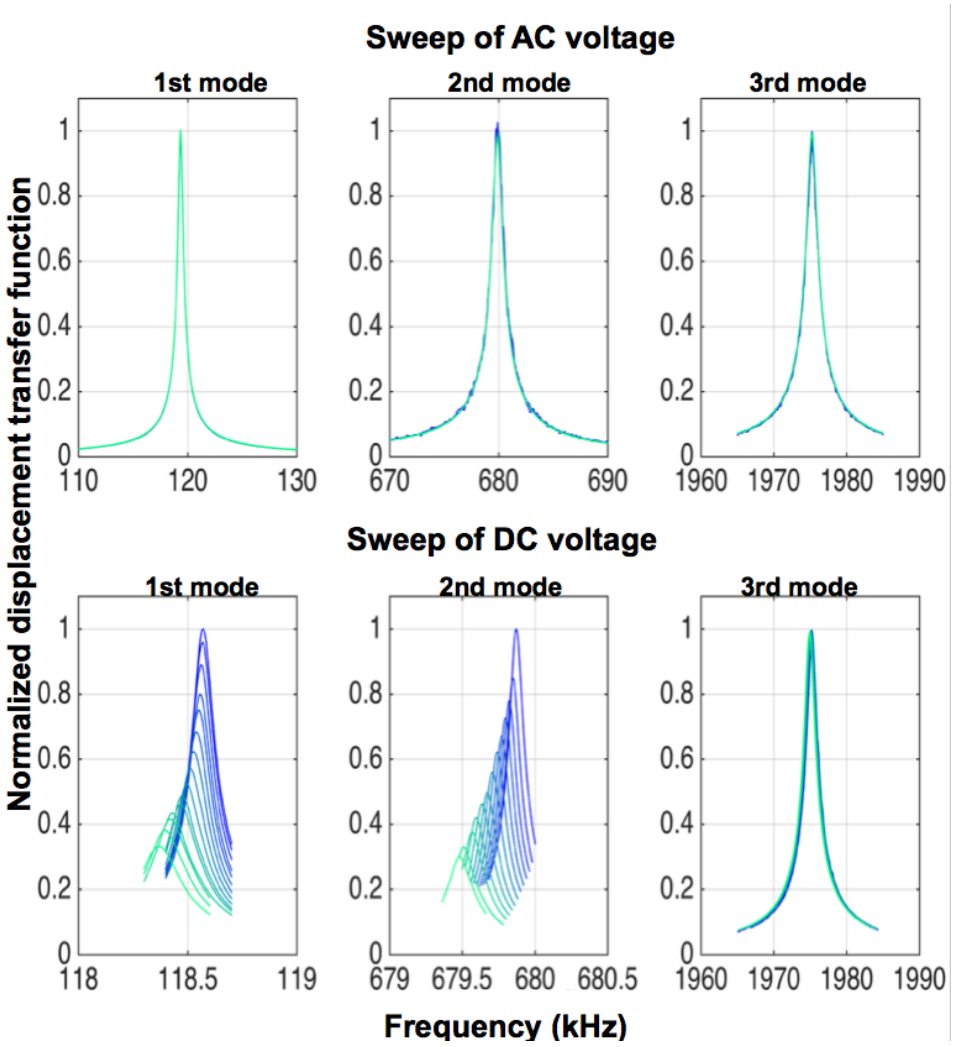

Figure C.10: *Transferfunction in air*

C.4 Probe Design # 4

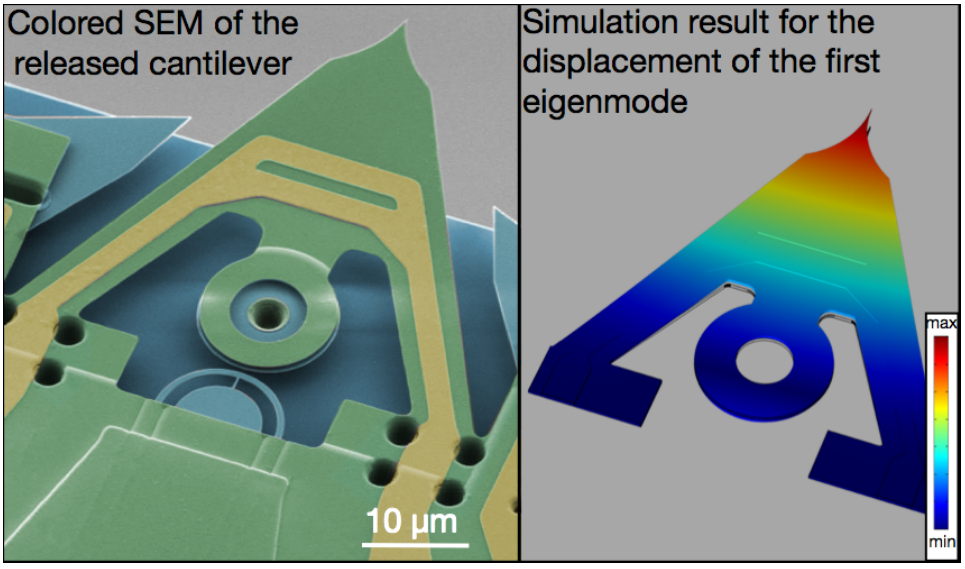

Figure C.11: *(left) Scanning electron micrograph of the released cantilever. (right) Simulation result for the displacement of the first eigenmode, to illustrate the cantilever movement.*

C.4.0.1 Mechanical spectrum

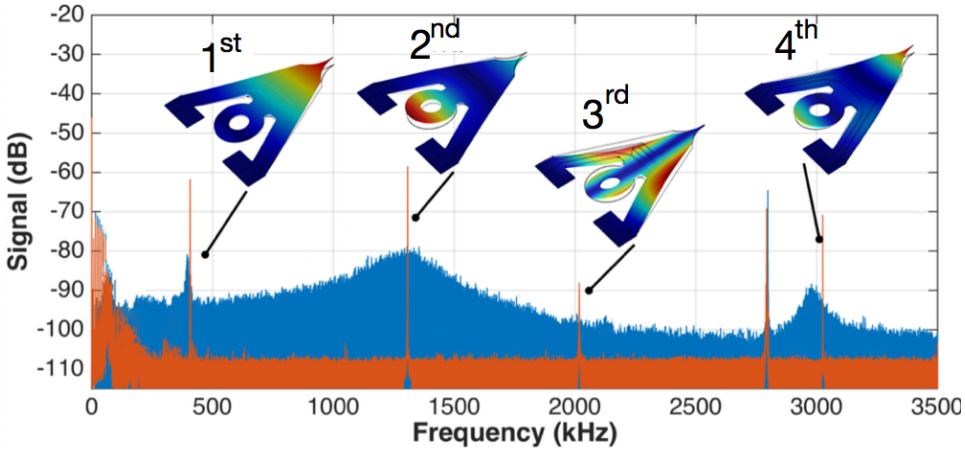

Figure C.12: *Mechanical spectrum in air (orange) and vacuum (blue (5 mPa)) for the cantilever layout # 4.*

Parameter	Value
g_{OM}	$38 \pm 3.5 \frac{\text{GHz}}{\text{nm}}$
β	$9 \pm 1.3 \frac{\text{V}}{\text{nm}}$
α_{disk}	2.5 ± 1.2 fm
dyn. range disk	≈ 6.3 nm

Table C.9: *The general optical parameter for the cantilever are summarized in this table.*

Mode	f_{res}	f_{sim}	m_{eff}	k_{disk}	k_{tip}
1st	407 kHz	409 kHz	5.8*10^{-13} kg	53.6 $\frac{N}{m}$	0.27 $\frac{N}{m}$
2nd	1.3 MHz	1.25 MHz	1.7*10^{-13} kg	8.4 $\frac{N}{m}$	13 $\frac{N}{m}$
4th	3 MHz	3.1 MHz	4.3*10^{-14} kg	137 $\frac{N}{m}$	1.9 $\frac{N}{m}$

Mode	$\sqrt{S_{VV\ peak}}$	Q_{air}	Q_{vacuum}
1st	3.4*10^{-9} $\frac{V}{\sqrt{Hz}}$	-	-
2nd	7*10^{-9} $\frac{V}{\sqrt{Hz}}$	-	-
4th	0.4*10^{-9} $\frac{V}{\sqrt{Hz}}$	-	-

Figure C.13: *The mechanical parameter of the cantilever are summarized in this table.* $\sqrt{S_{VV\,peak}}$ *has been measured with a laser power of* $\approx$ *. 10 µW at the disk coupling region*

Mode	α_{tip}	dyn. range tip
1st	36 $\frac{fm}{\sqrt{Hz}}$	140 nm
2nd	2 $\frac{fm}{\sqrt{Hz}}$	20 nm
4th	21 $\frac{fm}{\sqrt{Hz}}$	53 nm

Figure C.14: *The optical parameter related to the tip of the cantilever are summarized in this table.*

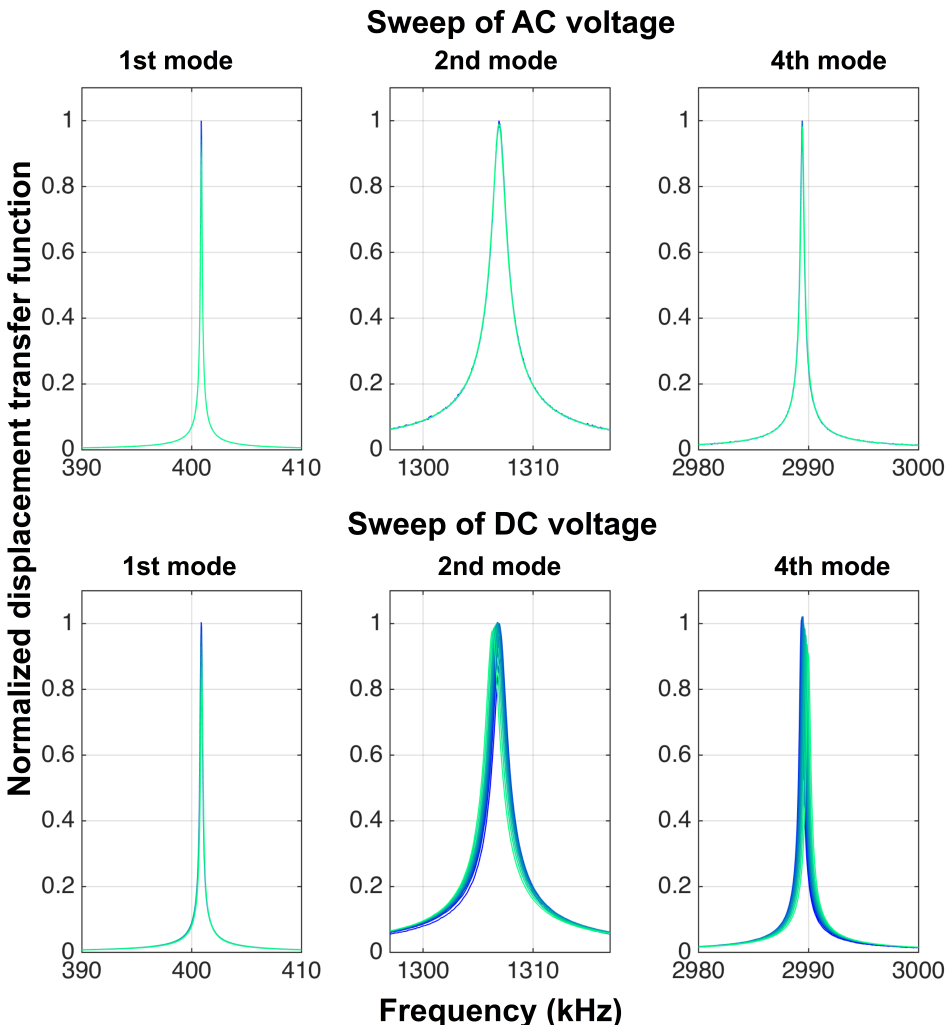

Figure C.15: *Transferfunction in air*

C.5 Probe Design # 5

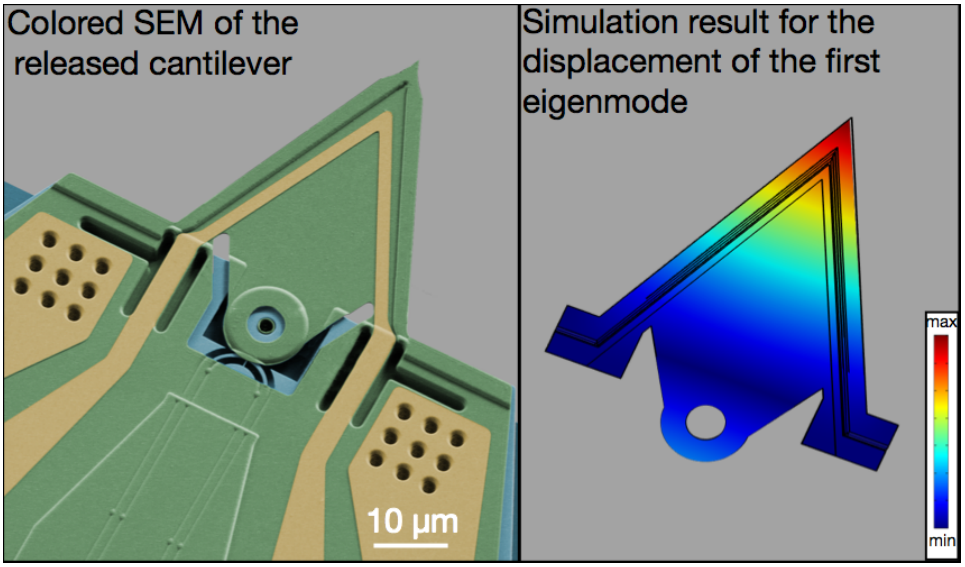

Figure C.16: *(left) Scanning electron micrograph of the released cantilever. (right) Simulation result for the displacement of the first eigenmode, to illustrate the cantilever movement.*

C.5.0.1 Mechanical spectrum

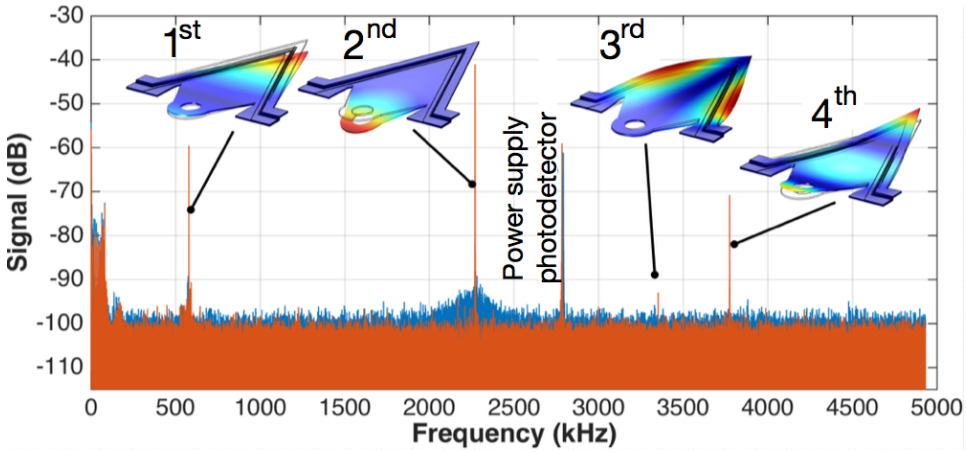

Figure C.17: *Mechanical spectrum in air (blue) and vacuum (orange (5 mPa)) for the cantilever layout #* 5.

Mode	f_{res}	f_{sim}	m_{eff}	k_{disk}	k_{tip}
1st	580 kHz	610 kHz	6.4*10^{-13} kg	99 $\frac{N}{m}$	8.5 $\frac{N}{m}$
2nd	2.27 MHz	2.12 MHz	3.7*10^{-13} kg	0.4 $\frac{N}{m}$	75 $\frac{N}{m}$
4th	3.77 MHz	3.59 MHz	1.18*10^{-13} kg	207 $\frac{N}{m}$	99 $\frac{N}{m}$

Mode	$\sqrt{S_{VV\ peak}}$	Q_{air}	Q_{vacuum}
1st	2.8*10^{-9} $\frac{V}{\sqrt{Hz}}$	57	2700
2nd	196*10^{-9} $\frac{V}{\sqrt{Hz}}$	23	3500
4th	0.2*10^{-9} $\frac{V}{\sqrt{Hz}}$	-	2675

Table C.10: *The mechanical parameter of the cantilever are summarized in this table.* $\sqrt{S_{VV\,peak}}$ *has been measured with a laser power of* $\approx$ *. 10 µW at the disk coupling region*

Mode	α_{tip}	dyn. range tip
1st	11.3 $\frac{fm}{\sqrt{Hz}}$	75 nm
2nd	2.6 $\frac{fm}{\sqrt{Hz}}$	0.36 nm
4th	4.7 $\frac{fm}{\sqrt{Hz}}$	13.6 nm

Table C.11: *The optical parameter related to the tip of the cantilever are summarized in this table.*

Parameter	Value
g_{OM}	31 $\pm$ 1.3 $\frac{GHz}{nm}$
β	6.8 $\pm$ 0.2 $\frac{V}{nm}$
α_{disk}	3.3 $\pm$ 0.15 fm
dyn. range disk	$\approx$ 6.8 nm

Table C.12: *The general optical parameter for the cantilever are summarized in this table.*

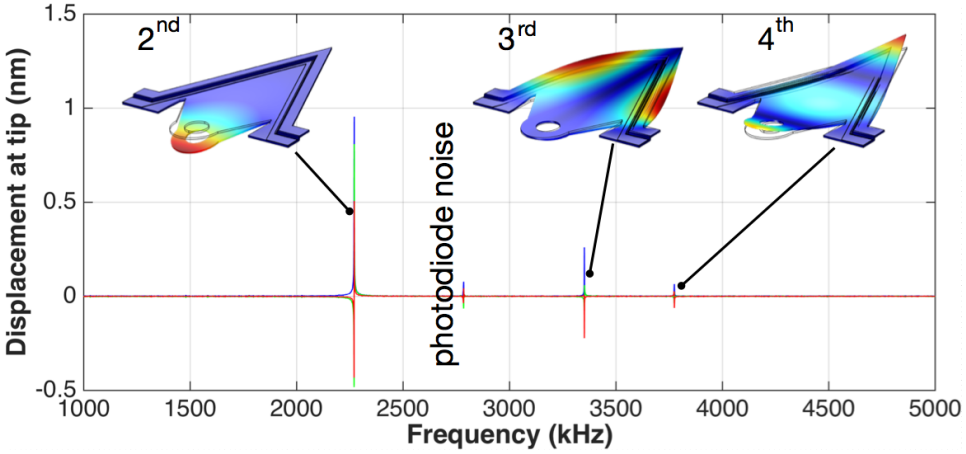

Figure C.18: *Transferfunction in vacuum*

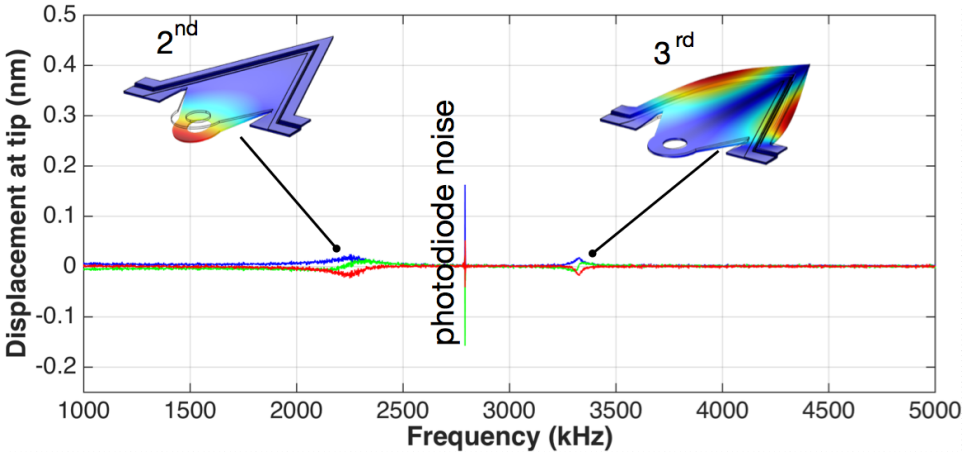

Figure C.19: *Transferfunction in air*

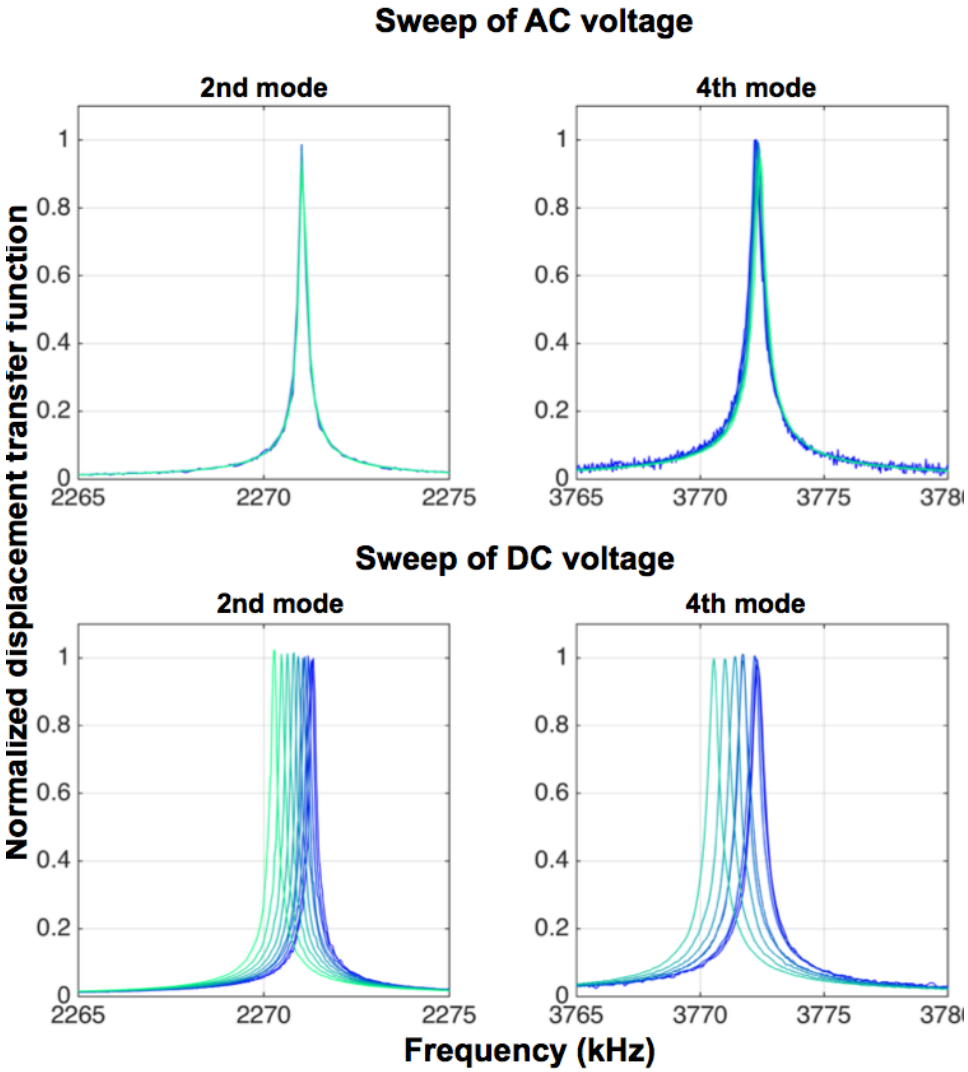

Figure C.20: *Transferfunction in air*

C.6 Probe Design # 6

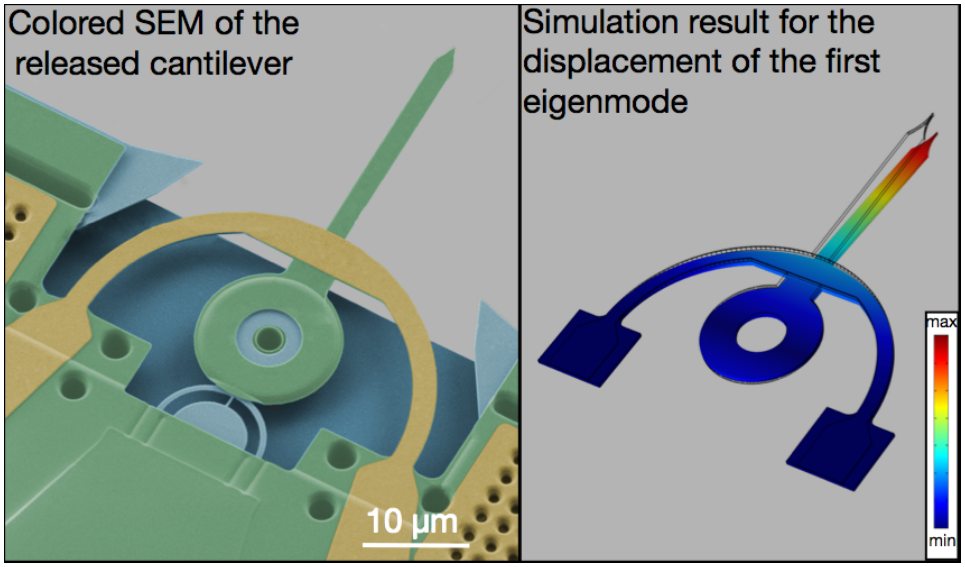

Figure C.21: *(left) Scanning electron micrograph of the released cantilever. (right) Simulation result for the displacement of the first eigenmode, to illustrate the cantilever movement.*

C.6.0.1 Mechanical Spectrum

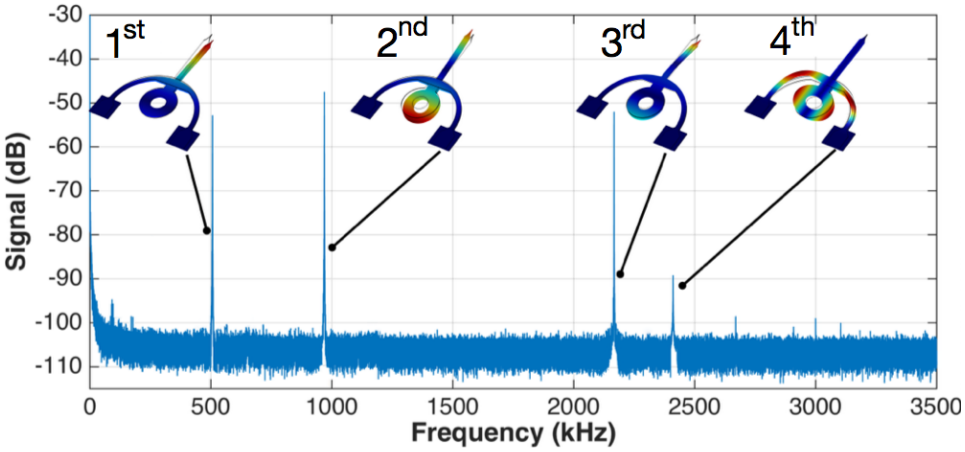

Figure C.22: *Mechanical spectrum in air (orange) and vacuum (blue (5 mPa)) for the cantilever layout # 6.*

Mode	f_{res}	f_{sim}	m_{eff}	k_{disk}	k_{tip}
1st	506.5 kHz	513 kHz	2.1*10^{-13} kg	63 $\frac{N}{m}$	0.08 $\frac{N}{m}$
2nd	969 kHz	970 kHz	1.8*10^{-13} kg	8.7 $\frac{N}{m}$	5.1 $\frac{N}{m}$
3rd	2.166 MHz	2.1 MHz	6.4*10^{-15} kg	9.3 $\frac{N}{m}$	0.1 $\frac{N}{m}$

Mode	$\sqrt{S_{VV\ peak}}$	Q_{air}	Q_{vacuum}
1st	26*10^{-9} $\frac{V}{\sqrt{Hz}}$	-	-
2nd	89*10^{-9} $\frac{V}{\sqrt{Hz}}$	-	-
3th	31*10^{-9} $\frac{V}{\sqrt{Hz}}$	-	-

Table C.13: *The mechanical parameter of the cantilever are summarized in this table.* $\sqrt{S_{VV\,peak}}$ *has been measured with a laser power of* $\approx$ *. 11 µW at the disk coupling region*

Mode	α_{tip}	dyn. range tip
1st	42 $\frac{fm}{\sqrt{Hz}}$	89 nm
2nd	2 $\frac{fm}{\sqrt{Hz}}$	11 nm
3rd	13 $\frac{fm}{\sqrt{Hz}}$	64 nm

Table C.14: *The optical parameter related to the tip of the cantilever are summarized in this table.*

Parameter	Value
g_{OM}	36 $\pm$ 3.5 $\frac{GHz}{nm}$
β	3.1 $\pm$ 0.7 $\frac{V}{nm}$
α_{disk}	1.5 $\pm$ 0.4 fm
dyn. range disk	$\approx$ 7 nm

Table C.15: *The general optical parameter for the cantilever are summarized in this table.*

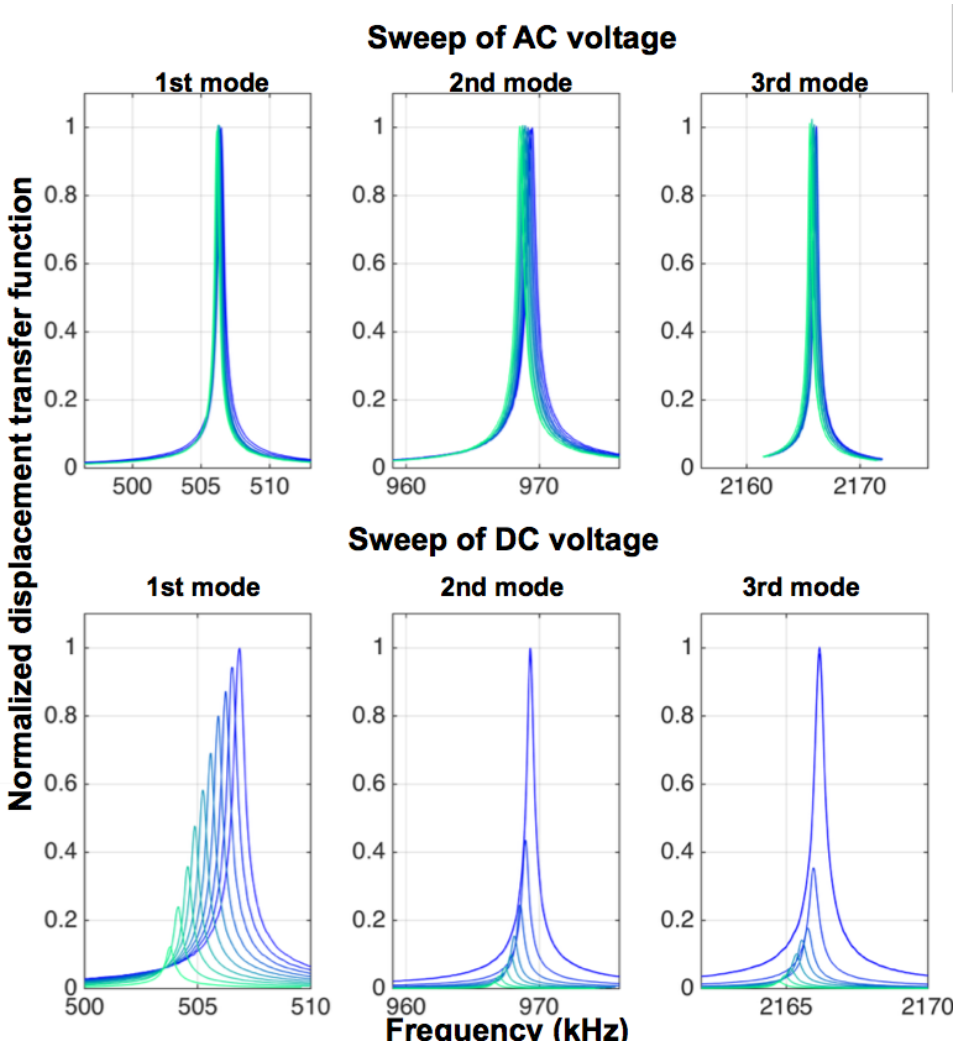

Figure C.23: *Transferfunction in air*

C.7 Probe Design # 7

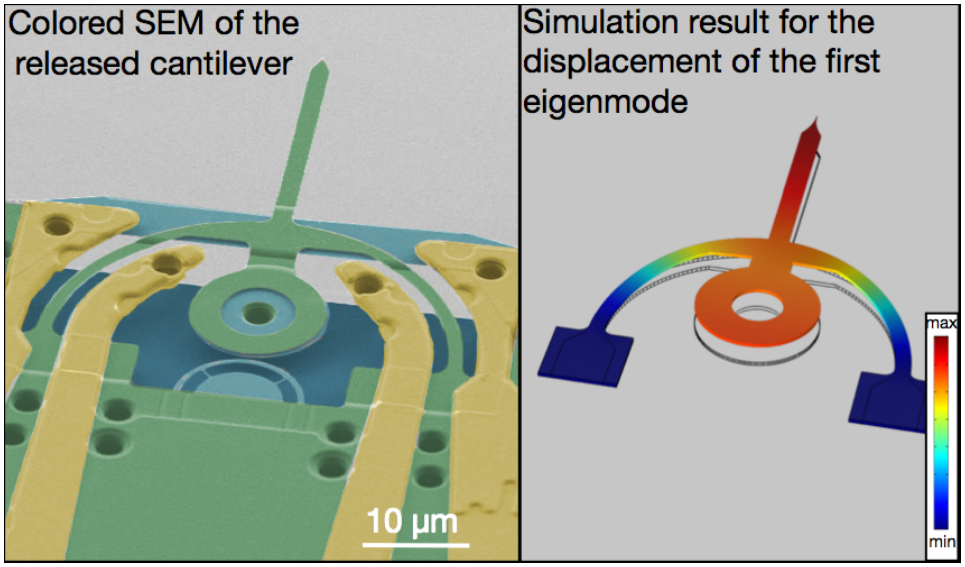

Figure C.24: *(left) Scanning electron micrograph of the released cantilever. (right) Simulation result for the displacement of the first eigenmode, to illustrate the cantilever movement.*

C.7.0.1 Mechanical Spectrum

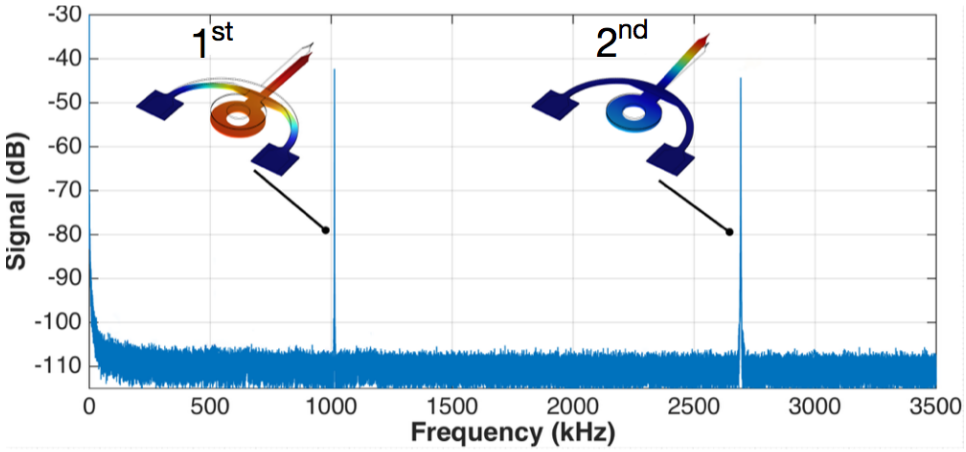

Figure C.25: *Mechanical spectrum in air (orange) and vacuum (blue (5 mPa)) for the cantilever layout # 7.*

Mode	f_{res}	f_{sim}	m_{eff}	k_{disk}	k_{tip}
1st	1.013 MHz	1.08 kHz	2.27*10^{-13} kg	13 $\frac{N}{m}$	8 $\frac{N}{m}$
2nd	2.69 MHz	2.72 MHz	9.5*10^{-16} kg	5 $\frac{N}{m}$	0.2 $\frac{N}{m}$
Mode	$\sqrt{S_{VV\ peak}}$	Q_{air}	Q_{vacuum}		
1st	294*10^{-9} $\frac{V}{\sqrt{Hz}}$	-	-		
2nd	178*10^{-9} $\frac{V}{\sqrt{Hz}}$	-	-		

Table C.16: *The mechanical parameter of the cantilever are summarized in this table.* $\sqrt{S_{VVpeak}}$ *has been measured with a laser power of* $\approx$ *. 9 µW at the disk coupling region*

Mode	α_{tip}	dyn. range tip
1st	0.8 $\frac{fm}{\sqrt{Hz}}$	6 nm
2nd	4 $\frac{fm}{\sqrt{Hz}}$	40 nm

Table C.17: *The optical parameter related to the tip of the cantilever are summarized in this table.*

Parameter	Value
g_{OM}	40 $\pm$ 3.5 $\frac{GHz}{nm}$
β	2.1 $\pm$ 1.3 $\frac{V}{nm}$
α_{disk}	0.67 $\pm$ 1.2 fm
dyn. range disk	$\approx$ 6 nm

Table C.18: *The general optical parameter for the cantilever are summarized in this table.*

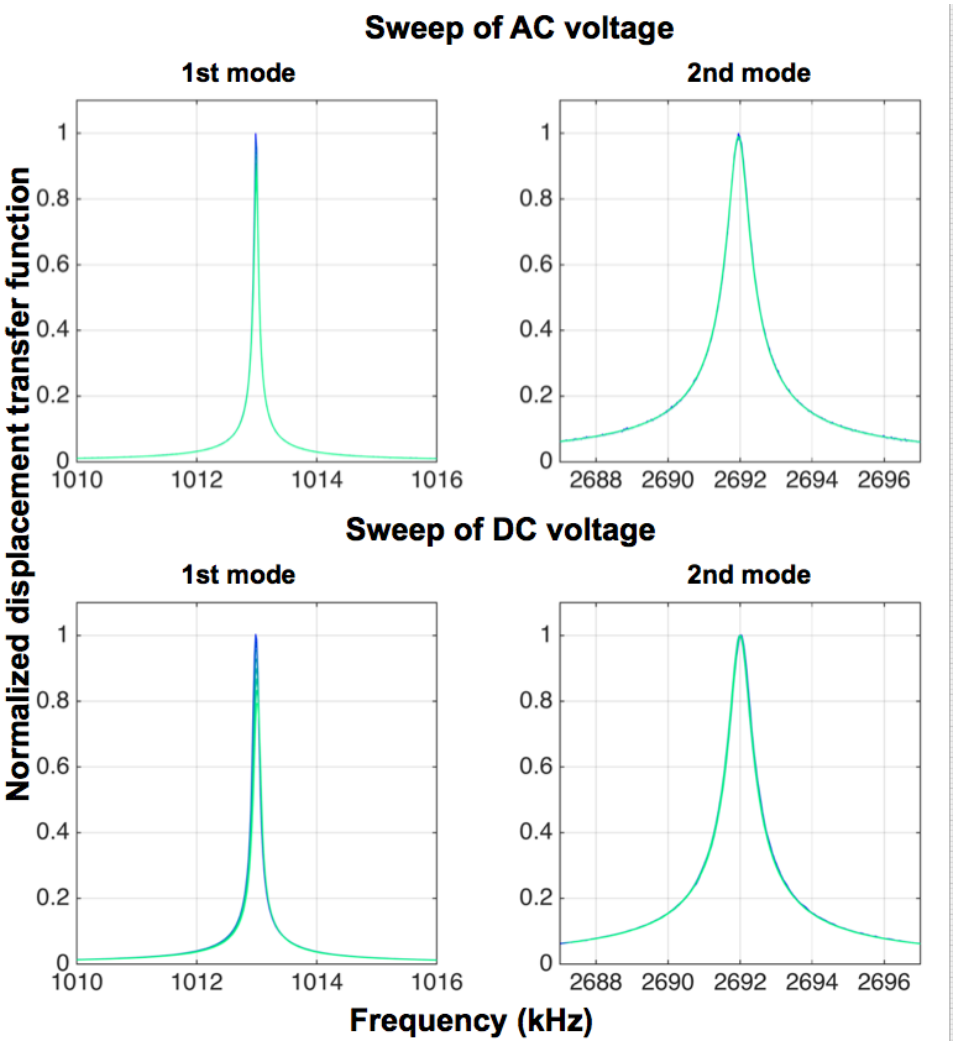

Figure C.26: *Transferfunction in air*

Declaration: I confirm that I wrote this dissertation by myself and without illegal assistance. I have not used resources other than quoted. All materials taken verbally or logically from published or unpublished scripts are identified. No part of this work is related to another dissertation or habilitation.

Erklärung: Ich versichere, dass ich die vorliegende Arbeit ohne unzulässige Hilfe Dritter und ohne Benutzung anderer als der angegebenen Hilfsmittel angefertigt habe. Die aus anderen Quellen direkt oder indirekt übernommenen Daten und Konzepte sind unter Angabe der Quelle gekennzeichnet.

Bei der Auswahl und Auswertung folgenden Materials haben mir die nachstehend aufgeführten Personen in der jeweils beschriebenen Weise entgeltlich/unentgeltlich) geholfen:

- 1. Vladimir Aksyuk beratend
- 2. Prof. Ivo Rangelow beratend
- 3. William McGehee FIB experiment (Aufbau und Auswertung)

Weitere Personen waren an der inhaltlich-materiellen Erstellung der vorliegenden Arbeit nicht beteiligt. Insbesondere habe ich hierfür nicht die entgeltliche Hilfe von Vermittlungs- bzw. Beratungsdiensten (Promotionsberater oder anderer Personen) in Anspruch genommen. Niemand hat von mir unmittelbar oder mittelbar geldwerte Leistungen für Arbeiten erhalten, die im Zusammenhang mit dem Inhalt der vorgelegten Dissertation stehen. Die Arbeit wurde bisher weder im In- noch im Ausland in gleicher oder ähnlicher Form einer Prüfungsbehörde vorgelegt. Ich bin darauf hingewiesen worden, dass die Unrichtigkeit der vorstehenden Erklärung als Täuschungsversuch bewertet wird und gemäß § 7 Abs. 10 der Promotionsordnung den Abbruch des Promotionsverfahrens zur Folge hat.